UNIVERSITÉ DE MONTRÉAL

CONTRIBUTION TO THE STUDY OF THE DIRECT AND INVERSE PROBLEM IN ELECTROMYOGRAPHY (EMG)

POOYA MAGHOUL

DÉPARTEMENT DE GÉNIE ÉLECTRIQUE

ÉCOLE POLYTECHNIQUE DE MONTRÉAL

UNIVERSITÉ DE MONTRÉAL

ÉCOLE POLYTECHNIQUE DE MONTRÉAL

Ce mémoire intitulé:

CONTRIBUTION TO THE STUDY OF THE DIRECT AND INVERSE PROBLEM IN ELECTROMYOGRAPHY (EMG)

présenté par: MAGHOUL Pooya

en vue de l'obtention du diplôme de Maîtrise ès sciences appliquées

a été dûment accepté par le jury d'examen constitué de :

M. BRAULT Jean-Jules, Ph.D., président

M. CORINTHIOS Michael J., Ph.D., membre et directeur de recherche

M. MATHIEU Pierre A., Ph.D., membre et codirecteur de recherche

M. VINET Alain, Ph.D., membre

DEDICATION

This thesis is dedicated to both my parents. My father, Behzad maghoul, did not only raise and nurture me but also taxed himself dearly over the years for my education and intellectual development.

My mother, Sima khoshnevis-asl, has been a source of motivation and strength during moments of despair and discouragement. Her motherly care and support have been shown in incredible ways.

Morover, my sister deserves my wholehearted thanks as well.

ACKNOWLEDGEMENTS

I would like to express my sincere gratitude to Prof. Bertrand for his support of my M.Sc. study and research, for his patience, motivation, enthusiasm, and immense knowledge.

Besides him, I would like to thank the rest of my thesis committee: Prof. Vinet, Prof. Brault, for their times which they spent to me.

Last but not the least, I would like to thank my family: my parents (Sima Khoshnevis-asl and Behzad maghoul) and my sister (Pooneh Maghoul), for giving supporting me spiritually throughout my life.

RÉSUMÉ

On dispose maintenant de prothèses myoélectriques du membre supérieur pouvant produire plusieurs mouvements utilisés dans les activités de la vie quotidienne. Pour les activer, la présence de 6 compartiments anatomiques dans le biceps brachial pourrait être exploitée. Pour aider à vérifier si ces compartiments ont pu être activés lors de contractions accomplies par des sujets normaux, l'utilisation d'un modèle direct et inverse pourrait être très utile. Pour initier le développement de ces modèles, des données provenant d'expériences où, un contenant cylindrique, encerclé de 16 électrodes et rempli d'une solution saline a été utilisé. Dsns ce bassin, jusqu'à 3 dipôles avaient été introduits à des positions connues. Pour poursuivre la validation du modèle inverse, on a simulé des signaux associés à 3 regroupements de 5000 fibres musculaires placées à des positions connues à l'intérieur d'un bassin cylindrique virtuel. Finalement, les signaux EMG recueillis au-dessus du biceps de sujets normaux lors d'expériences visant à activer individuellement ou en groupe les 6 compartiments du biceps ont été analysés. On a identifié 3 zones d'activité: une dans le chef court et 2 dans le chef long du muscle. Dans le chef court, l'intensité du dipôle a été similaire dans les 6 conditions testées tandis que sa position était variable. Dans le chef long, la position des deux zones actives est moins variable mais leur intensité très variable. Alors que les 3 zones d'activité peuvent être considérées comme étant situées dans divers compartiments du biceps, on a trouvé que leur position lorsque reportée sur une illustration générique d'une coupe transversale de l'avant-bras, l'une des zones était localisée au niveau de la couche de graisse et celle de la peau. Il semble donc possible d'identifier dans le biceps des zones d'activité associables à ses compartiments. Toutefois étant donné que certaines de ces zones pourraient se situer en dehors du muscle, la présence des couches de gras et de la peau doivent être introduites pour un modèle plus réaliste du bras lors d'études portant sur le problème direct et inverse en EMG.

Mots-clés: Biceps brachial, compartiments, matrice d'électrodes, EMG, modèle direct et inverse, contrôle de prothèses myoélectriques.

ABSTRACT

In the context of improving the control of upper arm myoelectric prostheses capable of producing various useful movements for daily life activities, the presence of up to 6 anatomical compartments within the biceps brachii can be exploited to increase the number of potential control sites. To help identify where activity could occurs within the biceps during different contractions accomplished by normal subjects, a direct and an inverse model could be very useful. To develop such models, we started with the reproduction of previously collected data obtained with 16 equally spaced electrodes circling a tank filled with a saline solution. Up to 3 dipoles were placed at known positions within the tank. To further test the inverse model, simulated data obtained from the activity of 3 groups of 5000 closely packed single fibers placed at known positions within a virtual tank similar to the real one were analyzed. Finally, EMG signals collected over the biceps brachii during experiments aimed at activating individually or in groups the 6 compartments of the biceps where analyzed in 6 conditions. Three zones of activity were found: one in the short head of the muscle and 2 in its long head. In the short head, the dipole intensity was similar in the 6 conditions tested while its position was variable. In the long head, the position of the two active zones was less variable but their intensity was quite variable. While those 3 zones of activity could be considered to be located in 3 of the 6 muscle's compartments, when their position was overlaid on a generic cross-section image of the upper arm, one of the zones was outside the muscle tissue. It thus appears possible within the biceps, to identify active zones associable to the muscle's compartments. However, considering that some of the detected positions could be over the fat and skin layers, those layers should be introduced for a more realistic upper arm model when studying the EMG direct and inverse problem.

Keywords: Biceps brachii, compartments, electrode array, surface EMG, direct and inverse model, myoelectric prostheses control.

TABLE OF CONTENTS

LIST OF TABLES

LIST OF FIGURES

List of abreviations

Ach	Acetylcholine
AP	Action potential
BB	Biceps Brachii
BEM	Boundary Element Method
BR	Brachialis
CMRR	Common Mode Rejection Ratio
DD	Double Differential
ECG	Electrocardiography
EEG	Electroencephalography
EMG	Electromyography
FDM	Finite Difference Method
FEM	Finite Element Model (FEM)
FF	Fast-Fatigable
FFR	Fast Fatigue-Resistant
IAP	Intracellular action potential
LAURA	Local Autoregressive Average
LDD	Longitudinal double differential
LSD	Longitudinal single differential
MEG	Magnetoencephalography
MN	Motoneuron
MU	Motor unit
MUAP	Motor Unit Action Potential
NDD	Normal Double Differential
SD	Single Differential (SD)
SFAP	Single Fiber Action Potential
TR	Triceps
WMN	Weighted Minimum Norm

CHAPTER 1: INTRODUCTION

The direct and inverse problem is a mathematical approach used in many branches of science and mathematics such as computer vision, medical imaging, machine learning and many other fields including electrophysiology. In the forward or direct problem, a known source is placed within a known volume conductor but the signals across the medium are not known and needed to be calculated. A single solution is obtained with an accuracy which depends to how well the source and the volume conductor characteristics are known. Results are obtained by applying pertinent physical laws. In the inverse problem, signals around the medium are known and the source(s) at their origin has/have to be found. Since many different source configurations could produce the same results, the inverse problem does not have a unique solution. To find the most pertinent results, a priori information or constraints on the system under study are used or simplified source and volume conductor models considered.

In electrophysiology, due to the clinical importance of detecting and correcting abnormal heart and brain activity from respectively electrocardiographic (ECG) and electroencephalographic (EEG) signals, many studies have been done on the direct and inverse problem. Results provided by inverse models are used to localize the source of a cardiac problem that a surgeon could cure and the same in EEG by pinpointing for instance to an epileptic zone within the brain.

In ECG, the forward problem implies the calculation of body-surface potentials from equivalent current dipoles representing the heart's activity or, during a surgery, from potentials generated directly on the heart. In the inverse model, with body-surface-potential distributions usually collected with a 12 lead systems, the considered current source is generally a single or an ensemble of current dipole(s). Initially, the volume conductor was assimilated to a cylinder but more elaborated models consisting in a real shape torso including lungs intercostal muscles and ribs are now available. Through adjustments of the parameters of the considered source(s), inverse models can be used to predict epicardial potentials or heart surface isochrones.

In EEG, an activity zone can be modelled either as a single equivalent dipole or as a complex 3D current source. For the representation of the head, a sphere composed of 3 concentric layers representing the scalp, the skull and the brain is frequently used but more realistic model can be obtained from 3D medical images. To solve the inverse problem, different software programs such as LAURA, LORETTA (downloadable from the Internet) or MN and EPIFOCUS are quite popular in this area.

To solve the equations of a direct model, the finite difference method (FDM) is a well-known method to get a good approximate solution for partial differential equations. When the volume conductor is homogeneous and has limited dimensions (i.e. bounded), the discretized integral equation method can be derived from the differential equation where only the potential values at the surface of the volume conductor are considered. When the medium is unbounded or when the boundaries can be described in a simple coordinate system, an analytic method is then adequate. What is happening in a volume conductor can be described with equations similar to the ones used in electrostatics making such equations very popular.

As for the inverse problem, it is an ill-posed problem since many solutions could give the same results. To get the best available solution the over-determined approach or the under-determined one can be used. In the over-determined approach, the basic a priori assumption is that a small number of current sources in the volume conductor can be adequately modeled by dipoles. A unique solution is obtained when the number of independent measurements is greater than the number of parameters to be determined. The best location of these limited numbers of sources is found by computing the surface electric potential map generated by the dipoles using a forward model and comparing its results with the actual experimental results. Scanning through the whole solution space for the best location and orientation of the sources is complicated and gets impractical when two or more dipoles are considered. Non-linear optimization methods integrated in directed search algorithms can be used but there is a risk that they get trapped in a local minimum.

The under-determined method is used when the exact number of dipole sources cannot be determined a priori. The approach thus consists on establishing solutions points associated to a 3D grid of the volume conductor offering many more points than the number of signals collected over its surface. Since many distributions of current sources within the 3D grid points can reproduce the recorded potentials, different assumptions have to be used to identify the most reliable solution.

Compared to ECG and EEG fields, the direct and inverse problem in electromyography (EMG) has received less attention due to its more limited impact on the health of a person. However, since the generation of those 3 signals have similar electrophysiological basis, the approaches used in ECG and EEG can thus be of great help for the EMG situation.

When the presence of a neuromuscular disease is suspected, its detection and characterization is either done with a biopsy or with intramuscular recording. To help identify where to do such procedures, or as an alternative to those invasive methods, surface EMG recordings can be used and, with an inverse model, useful information obtained on the characteristics of active current sources under a certain location of a limb. A cylinder is the simplest shape to model a limb volume conductor while more realistic ones can be obtained, as in ECG and EEG, from magnetic resonance images.

Recent interest for the direct and inverse problem in EMG can be partly associated to the modern wars where the death of soldiers equipped with bulletproof vests are less likely than in previous wars while results in an increase numbers of amputated veterans. To take care of their amputee veterans, who could be quite young and thus have a long life expectancy, the American government has allotted important sum of money for designing sophisticated upper limb prostheses. Very often, the control of such prosthesis is based on EMG signals generated from contractions of the muscles left inside the limb following amputation. To exploit the full capabilities of sophisticated prostheses, which is of importance for a young veteran in their daily life activities, many muscle control sites are required while their number have been reduced due

to the amputation. When an upper limb has been completely lost, elaborate surgical procedures can be used to re-route nerves formely used to produce arm movement to trunk muscles in order to create new control sites. For less severe amputations, various signal processing algorithms can combine a certain number of available EMG signals into a greater number of different patterns of activity an assign each of the most reliable ones to a given movement of the prosthesis.

With the same objective of increasing control sites, our group is relying on muscle anatomy. In the upper arm, the biceps brachii (BB) muscle has been shown, through cadaver dissections, to be composed of up to 6 compartments each individually innervated by a nerve branch. They could thus be voluntary made to contract making possible to have 6 control sites instead of one from this muscle. Interestingly, other arm muscles also appear to have compartments. Illustration of an hypothetical division of the biceps compartments (1 to 6) is shown in Fig. 1.1
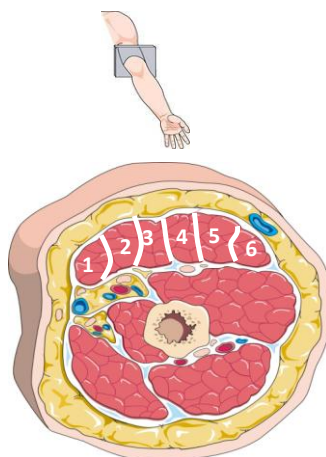
Fig 1.1 Generic representation of a cross-section of the arm with the skin, the fat (yellow), muscles (red) and the humerus bone (at the center) of the upper arm. The biceps is at the top of the illustration with hypothetical divisions representing its 6 compartments.

Experimental EMG signals have thus been collected over the BB of normal subjects by another graduate student (Nahal Nejat, [40]). Ten pairs of surface electrodes were positioned over the muscle and the subjects were asked to produce contractions while their arm was in different positions in order to solicit the various compartments of the muscle. Our project here is to

analyze those EMG distributions with an inverse model with the aim of identifying in which hypothetical compartment the biceps activity could be located.

The development of our direct and inverse EMG models was initially tested on another graduate student data (David Filion, [15]) who collected signals from 16 electrodes uniformly distributed around a circular tank. In the tank filled with a saline solution, up to 3 current sources were inserted at know positions. Our analytical direct model is based on Okada work and an over-determined inverse model based using a genetic algorithm and a conjugate gradient method was used to locate the position of the sources in the tank. We then used our models to analyze the experimental EMG signals that were collected over the BB of normal subjects.

The thesis is made out of 5 chapters. Following this introduction, the second chapter is devoted to the literature review with an initial section related to the anatomy and physiology of the upper arm and a second one on the methods used to solve the direct and inverse problems in electrophysiology with special coverage for the EMG field.

In the third chapter, a description of the signal acquisitions made with a tank by David Filion will be presented as well as the context within which experimental EMG signal were collected by Nahal Nejat from 10 normal subjects. A description of our direct and inverse model is also presented.

Results are presented in the fourth chapter. Following localization of the dipoles within the tank, results obtained with the experimental EMG signals are presented for few subjects. In the fifth chapter, a Discussion of the obtained results is presented and it is followed by a Conclusion and a view on where future works could be heading.

Chapter 2: LITTERATURE REVIEW

2.1 MUSCLES

2.1.1 Anatomy

Skeletal muscles are attached to the skeleton. They are anchored by tendons to two bony structures which are linked by an articulation. The upper limb for instance has two main articulations one at the shoulder level and one between the arm and the forearm. This is illustrated in Fig 2.1A where the humerus of the upper arm is attached to the skeleton through the scapula articulation which is an element of the shoulder. The lower end of the humerus makes an articulation with the ulna and radius. Those two bones of the forearm permit many movements that can be produced by the hand. As shown in Fig 2.1B, the biceps brachii is attached at the shoulder and elbow level and when this muscle is contracted, a flexion at the elbow level is produced. To produce an opposite movement, another muscle, the triceps (also seen in Fig 2.1B) is attached across the elbow articulation but in opposite direction has to be contracted.

A muscle is composed of many fibers which are generally aligned in parallel. Those fibers (Fig 2.1C) are bundled in groups called fascicles and a muscle is composed of several fascicles. Looking closely at a muscle fiber, it can be seen that it is made of many subunits called myofibrils. When a myofibril is examined, a repetition of zones of different intensities separated by vertical lines is seen all along its length. Called sarcomeres, those repeating units, are each shortened during a muscle contraction by a micron or so. The sum of each of those microscopic shortenings results in an appreciable change in length of the contracted muscle or in a production of a force. Sarcomeres are made of thin filaments of actin and of thick filaments of myosin which are intermingled as can be seen at the bottom of Fig 2.1C. When those filaments slides between each other during a contraction, their length is reduced (Fig 2.1D).

2.1.2 Physiology

To produce a voluntary movement, a command is generated in the brain and communication between its neurons and the peripheral muscles is done through action potentials (APs) which are

produced within each of those neurons and muscular fibers. At rest, the potential inside a cell is around -65 to -70 mV due to its semipermeable membrane and the ionic gradients existing between the interior and the outside (Fig 2.2A). When few sodium (Na^+) ions are moved inside the cell due to an input to its dendrites, a depolarization occurs while a hyperpolarization is induced when potassium (K^+) ions leak out of the cell. When the depolarization is important enough to reach a certain threshold, an all or nothing phenomena occurs (Fig 2.2B): a massive number of Na^+ ions flow in the cell causing an important depolarization reaching momentarily ~+20 mV following which an important amount of K^+ ions flow out of the cell and repolarize it. After a rapid passage below the resting potential the resting potential is re-established.
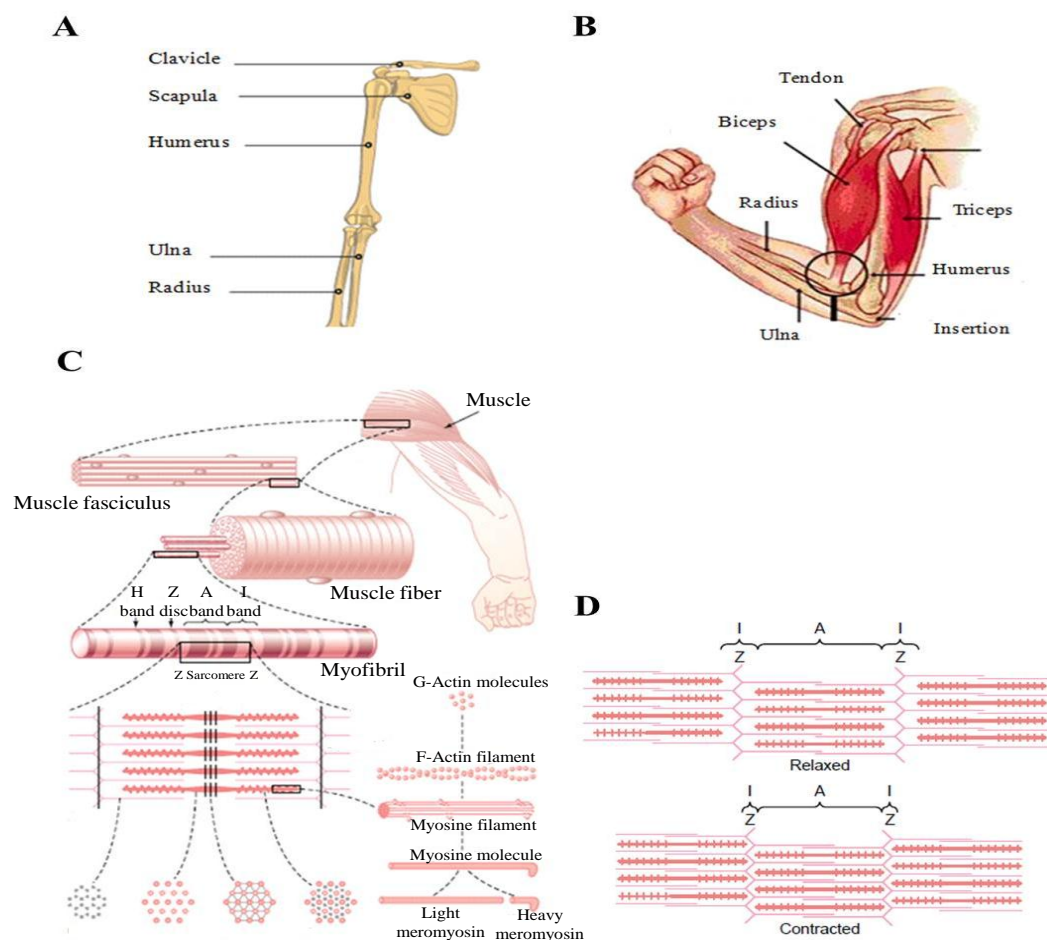
Fig 2.1 A. Bones of the arm attached to the shoulder articulation (Encyclopedia Britannica Online). B. Transverse view of the arm with anatomical position of the biceps and triceps (from [7], p. 156). C. Structure and components of a squelettal muscle up to a sarcomere within which item F represents a section of an actin filament, G a section of myosin, H a section in the middle of the sarcomere and I a section where actin and myosin can interact D: Illustration of the shortening of 3 sarcomeres (from [22], p.74-75).

A

B
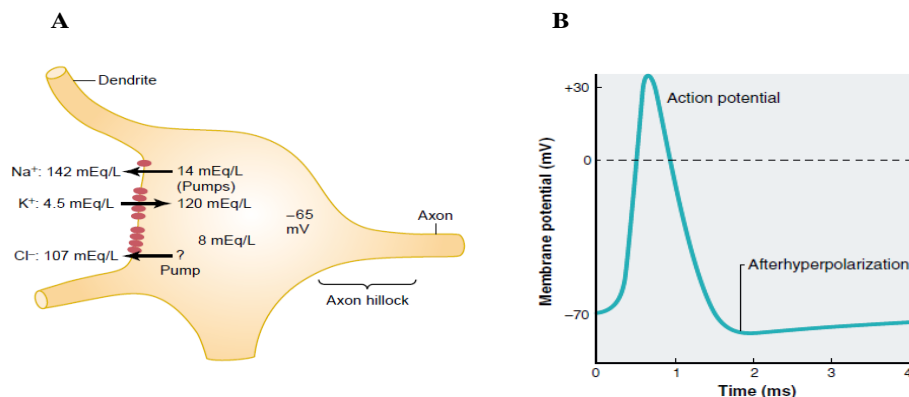
Fig 2.2 A: Schematic of a neuron where the different concentrations of Na^+ and K^+ across its semipermeable membrane create a resting potential around -65 Mv (from [22], p. 564) B: when dendrite activity causes a depolarization high enough to reach a thresholed, an action potential is generated (from [58], p. 191).

APs generated in the brain to produce a movement are propagated by their axons in the spinal cord where they are grouped within nerves to finally make contact with the motoneurons (MNs) (Fig 2.3). Axons of the MNs leave the spinal cord to reach a muscle, when near a muscle each axon of a MN produces many branches each of them making contact with a different muscle fiber. A motoneuron plus the fibers to which it is connected constitute a motor unit (MU). The number of MUs per muscle in humans may range from about 100 for a small hand muscle to 1000 or more for large powerful limb muscles [35]. An example of a MN making contact with 2 muscle fibers and a second one which makes contact with 3 other muscular fibers is illustrated in Fig 2.3. Activity in a MN induces the contraction in all the muscle fibers to which it is in contact.
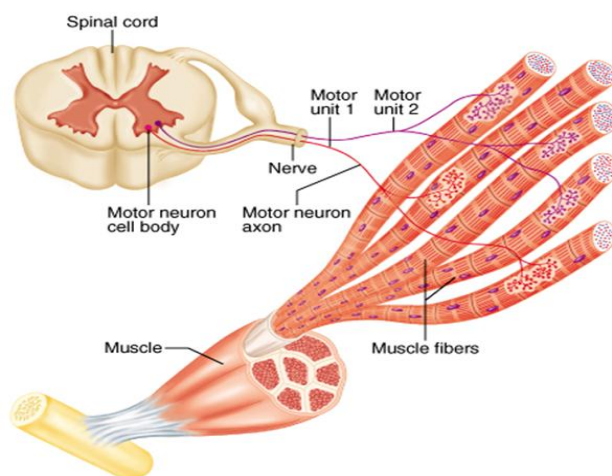
Fig 2.3 Axons of 2 motoneurons extending from the spinal cord to a muscle. Each axon divides into a number of branches that make contact with some of the muscle fibers scattered throughout the muscle (from [35], p. 251).

2.1.3 The Neuromuscular Junction and Mechanisms of the contraction

 Where 2 muscular APs are produced, each travels in opposite direction up to the 2 tendons. As those 2 APs move along the fiber, they also propagate in the transverse (T) tubules which are surrounding the sarcoplasmic reticulum which encircles each myofibril (Fig 2.4). In the transverse tubules, the passage of the AP induces a Ca^{++} release from the lateral sacs of the sarcoplasmic reticulum. As previously mentioned, myofibrils are made of actin and myosin. In Fig 2.5A, myosin is represented by two large polypeptide chains with cross-bridges pointing toward the thin filaments (Fig 2.5B). The thin filaments also contain two other proteins: troponin and tropomyosin (Fig 2.5C). At rest, the cross bridges are not in contact with the actin but when Ca^{++} is present, it removes the troponin-tropomyosin complex from the actin making possible the interaction of the myosin cross-bridges with actin. This leads to the sliding of the actin over myosin filaments and consequently, the contraction of each sarcomere of each myofibril (Fig 2.5D). As long as Ca^{++} ions are present, the process is repeated again and again until the actin filaments pull the Z membrane up against the ends of the myosin filaments or until the load on the muscle becomes too great for further pulling to occur. When no more APs from the motoneuron are reaching the end-plates, the Ca^{++} ions are pumped back in the sarcoplasmic reticulum and the sarcomeres regain their initial length and are ready to contract again.

2.1.5. Two types of contractions

In an isotonic contraction, the tension generated in the muscle remains constant throughout the contraction while the muscle length is modified (Fig 2.6A). .In an isometric contraction, a force is produced while the muscle length is kept constant (Fig 2.6B).

2.1.6. Recruitment of MUs

The force generated by a muscle is proportional to the number of active MNs and the number of fibers they innervated. There are three types of MUs:

   1- Slow (*S*) which innervate a small number of small fibers,
   2- Fast Fatigue-Resistant (*FFR*) which innervate more fibers of a larger diameter,

3- Fast-Fatigable (*FF*) which innervate a large numbers of fibers of large size.
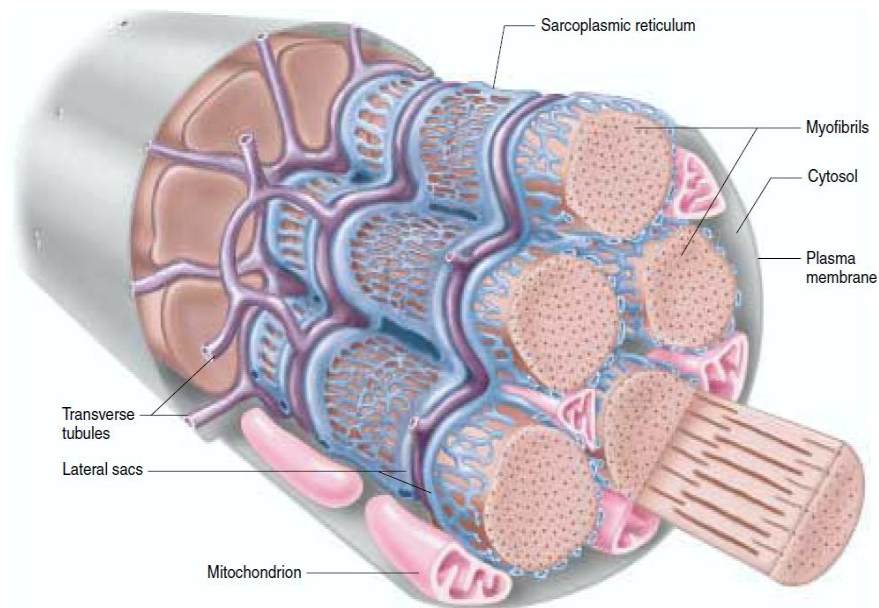
Fig 2.4 Anatomic structures of the transverse tubules and of the sarcoplasmic reticulum system in a single skeletal-muscle fiber (from [58], p. 303).

For the *S type*, force production is due to an oxidative process which relies on the presence of oxygen and the force produced is small. For *FFR type*, energy to contract is partly dependent on the availability of oxygen and on the presence of stored glycogen within the fibers. Those MUs produce a greater force than *S* units, Finally, *FF* fibers are only using the glycolytic process for its energy source and their force output is large.

For a contraction of low intensity, the *S* (also called *type I)* MUs are activated. When more force has to be produced, additional *S* MUs are recruited as well as those of type *FFR* (or *type IIA)*. When still additional force is needed, *FF* MUs are then added to *S* and *FFR* types (Fig 7A). This order of recruitment from the smaller to the larger MUs (i.e. *S* to *FF*) is named the Henneman principle (Fig 2.7B). The largest MUs are thus set in action in only few occasions. As seen at the bottom of Fig 2.7A, when a MU of type *S* is solicited on a long period of many minutes, its mechanical output is kept constant and such MU is said resistant to fatigue. When a FFR unit is solicited for a long time, fatigue sets in and its produced force decreases with time. The presence

of fatigue develops more rapidly for the powerful *FF* units. This is due to the differences between the oxidative and the glycolytic processes used by those MUs to produce energy.
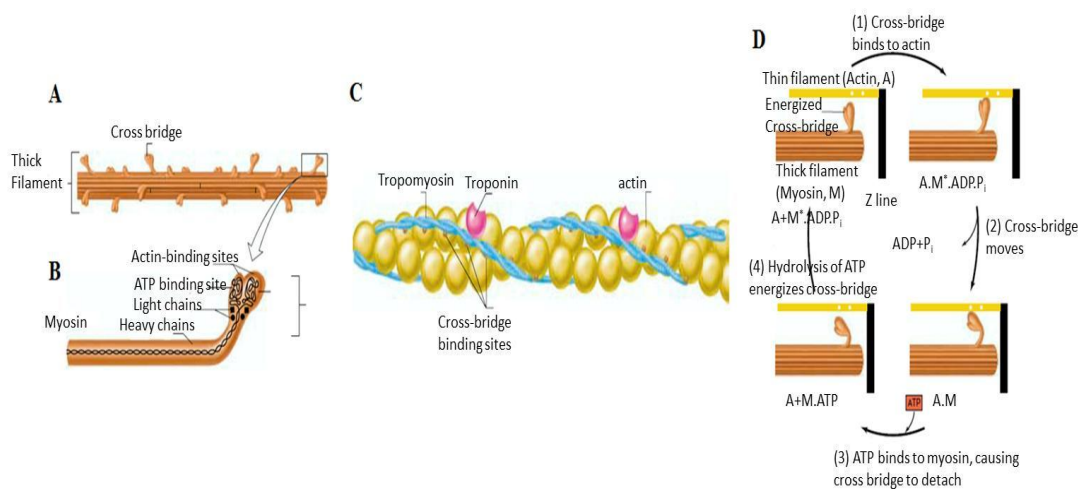
Fig 2.5 A: Heavy chains of myosin molecules form the core of a thick filament. The myosin molecules are oriented in opposite directions in either half of the filament. B: The two globular heads of each myosin molecule extend from the sides of the filament forming a cross bridge. C: A molecule of troponin is bounded to a molecule of tropomyosin and that association prevents interaction with the myosin cross bridges. D: Four stages of a cross-bridge cycle. 1: In presence of Ca^{++}, a link is made between actin and myosin. 2: the binding triggers the release of ATP which induces an angular movement of each crossbridge. 3: A new ATP binds to the cross bridge and cause detachment from the actin. 4: ATP is splited into ADP and P for new movement. M* represents an energized myosin cross bridge (from [58], p. 299, 300, 302).
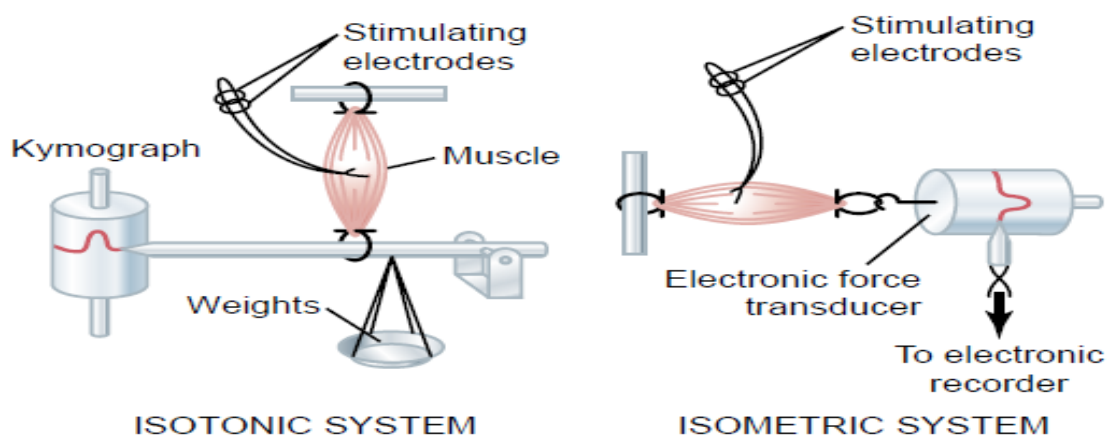
Fig 2.6 At the left, the load pulling on the muscle is constant and an isotonic contraction is produced when the muscle is stimulated. At the right, the length of muscle is kept constant and an isometric contraction is produced (from [22], p. 80).
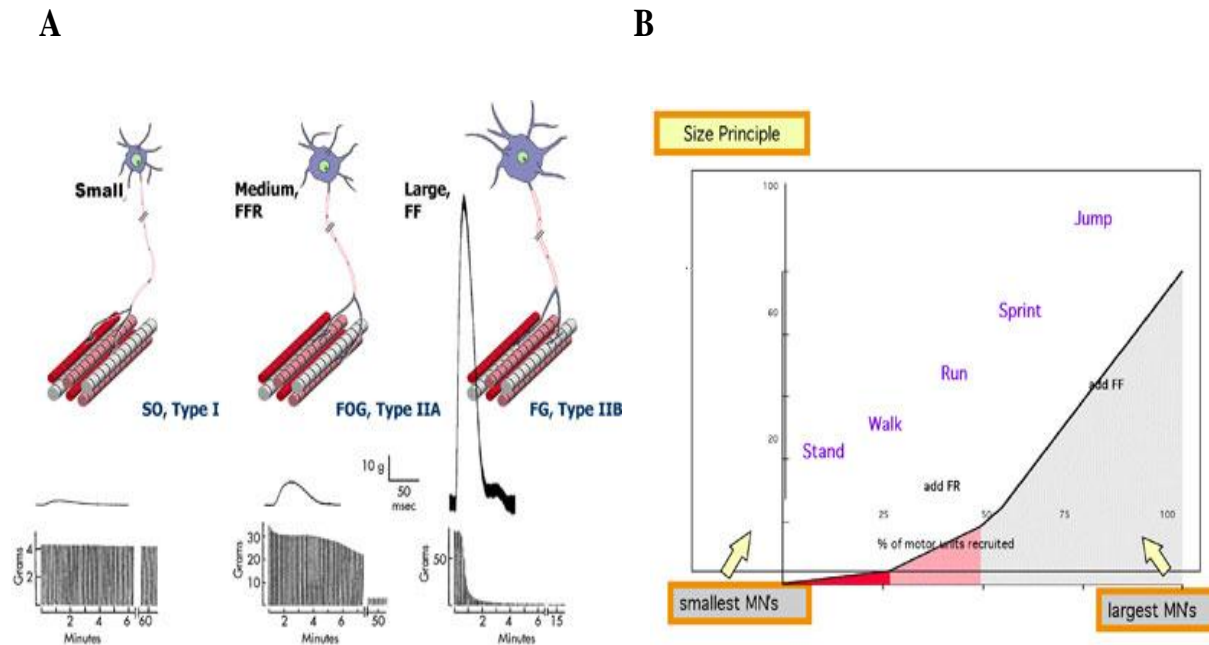
Fig. 2.7 A: three types of motor units with the amplitude of their twitch when electrically stimulated and their resistance to fatigue upon continuous stimulation.B: The size or Henneman principle: small motor units are initially recruited and when more power is required to increase the speed, medium and large MUs are then recruited (from [41], p. 451).

2.1.7 Muscle compartments

Generally, muscles are considered as single entities but this not always the case. For instance, the dissection of the cat lateral gastrocnemius muscle was revealed four compartments each innervated by a primary branch of a nerve. Activity within each compartment was collected with implanted electrodes and when the cats walked at low speed, more intense EMG activity was found in distal than proximal compartments while at moderate to fast speeds, the intensity of activity in proximal compartments was equal to or greater than in the distal compartments [5, 9, 10 and 31].

As for the human biceps brachii (BB) muscle, dissections of Segal [51] revealed on the dorsal face of the muscle the presence of 4 to 8 (Fig 2.8) natural grouping of the fibers called

compartments. Each of those grouping is innervated by a nerve branch which sometimes gave other branches suggesting the presence of smaller units within a compartment. Electrophysiologically, Ter haar Romeny et al ([53], [54]) reported for the cat LG muscle, that the territory of a MU occupies only a fraction of the muscle cross-section area. This factor, coupled with the broad tendons linking the muscle to the bones, lead to its implication in the production of different movements of the cat upper-limb ([60], [61]).

For English et al. [11], the ramification of each compartment nerve branches is a significant aspect of muscles control to consider since in a compartment, a nerve can be divided in primary or first-order nerve branches which could divide to produce other (higher order) branches. In the primary nerve branch, motoneuron axons enters only one compartment while for the higher nerve branches, the axons of some MNs can innervated several compartment sub-units called *subcompartments* (Fig 2.9). Beside the BB, neuromuscular compartments have also been observed in other human arm muscles such as the flexor carpi radialis and the extensor carpi radialis longus [52]. Ability of voluntarily contracting those compartments individually or in groups could be very useful to facilitate the control of myoelectric prostheses by amputee persons.
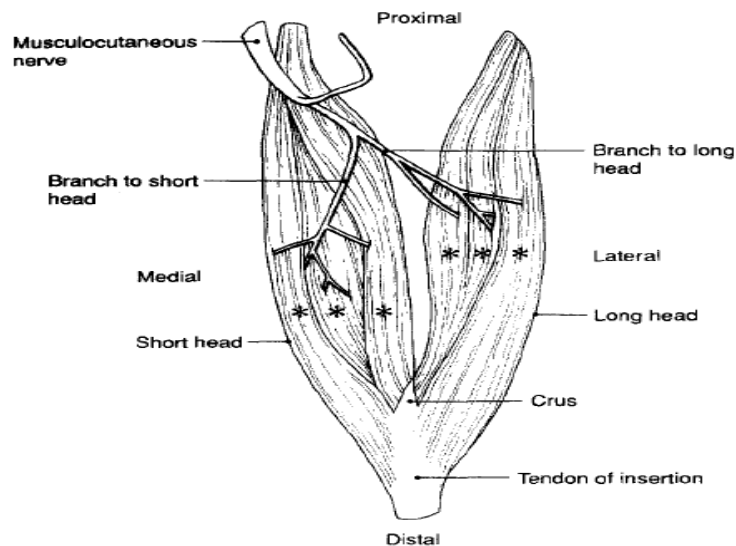
Fig. 2.8. Posterior view of the biceps brachii where asterisks indicate neuromuscular compartments in the long and short head. In the most cases, musculocutaneous nerve does not insert to the long and short head of BB directly but it divided into several branches each * identifies a compartment. (from [51], p.100).
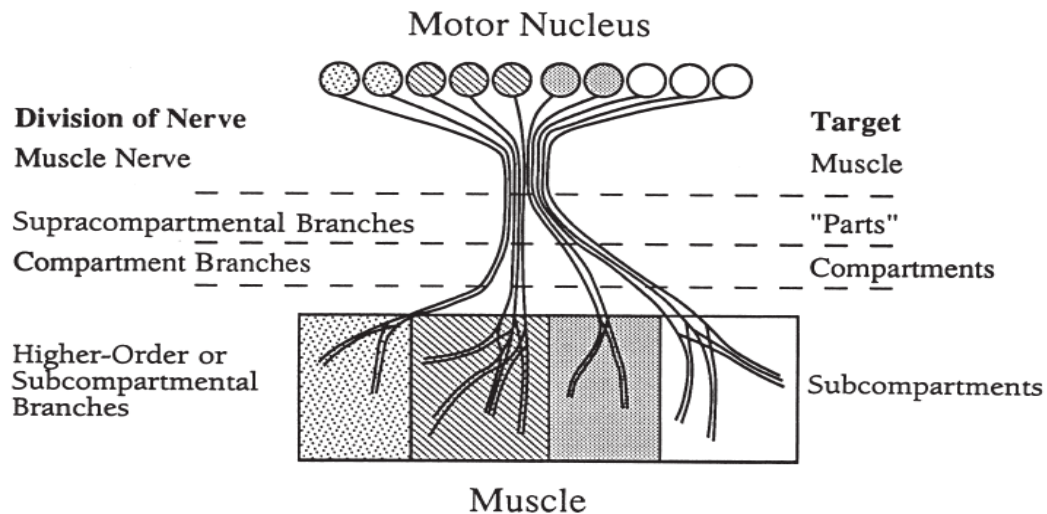
Fig 2.9 Schematic representation of motoneurons and compartments of one muscle. The circles at the top of the figure represent the motoneurons innervating a muscle, and the boxes at the bottom symbolize the different compartments of the muscle innervated by these motoneurons. Each compartment is illustrated by different shades. Each motoneuron is connected to its compartment by axon which is demonstrated by one solid line. The collection of axons into a single muscle nerve and the branching of this muscle nerve are indicated by the horizontal dashed lines. (from [11], p. 861).

2.2 EMG recording techniques

2.2.1 Intramuscular electrodes

The ionic exchanges associated to the initiation and propagation of an AP within muscle fibers give rise to electrical potentials called electromyograms (EMG). To record that signal, fine electrodes of various types can be inserted inside a muscle. For example, when inserted in a muscle, the concentric and monopolar needle electrodes which have a small recording area (~ 0.20 mm^2) can be used to record the activity of only few muscle fibers of a given MU which are in its close vicinity (Fig 2.10). Amplitude of the recorded signal is proportional the electrode uptake area: with large recording surfaces, activity from a large area within the muscle is picked up. A large amplitude signal with a reduced spatial selectivity is thus obtained.
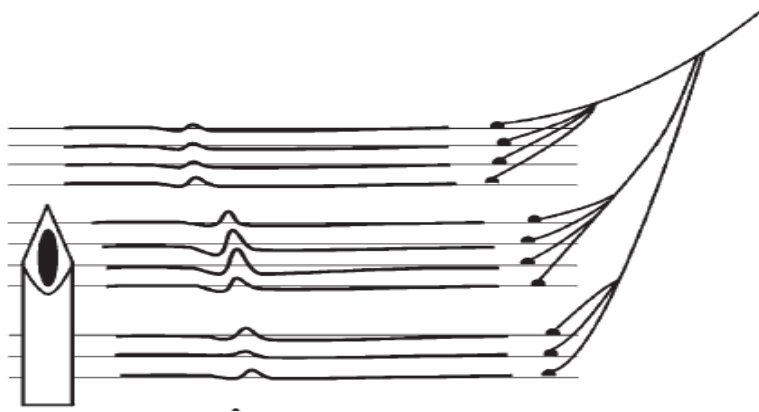
Fig. 2.10 Illustration of a concentric needle electrode inserted close to the muscular fibers of 3 MUs which are simultaneously generating an extracellular APs with amplitude proportional to the diameter of the MU's fibers. Activity of the closest fibers to the electrode will have the largest contribution to the signal collected. In the illustration, activity of the top MU will be first detected because its neuromuscular end-plate zone is closest to the electrode. (from [36] p. 29)

2.2.2 Surface electrodes

Intramuscular recordings are invasive and thus used in special settings when information collected is greater than the risks associated with the procedure. Surface recording where electrodes are directly placed on the skin surface is thus the most frequent method of collecting EMG signals. The diameter of surface electrodes can vary from 4 to 10 mm and are usually made of Ag/AgCl, or with silver or gold. The biological tissues interposed between the surface electrode and the active fibers constitute a volume conductor which acts as a low-pass filter. Surface electrodes can take different configurations (Fig 2.11A). When spatial sampling of the activity over a muscle is of interest, linear or a matrix array of electrodes can be used (Fig 2.11B and C).

Signals at the electrodes level may be in the microvolt (µV) range and should be amplified by a factor of 1000 or more. Amplifiers need to have high input impedance, a high Common Mode Rejection Ratio (CMRR) and have a low noise level. Analog filters can cover 2 Hz to many KHz. Monopolar recording (Fig 2.12A), bipolar (single differential (SD) and double differential (DD) (Fig 2.12B, C) is possible. Bipolar or differential (SD configuration is most frequently used due to its interferences removing such as power line [2]. DD configuration is used when crosstalk originating from other muscles is to be minimized and for non-invasive conduction velocity measurements [20].
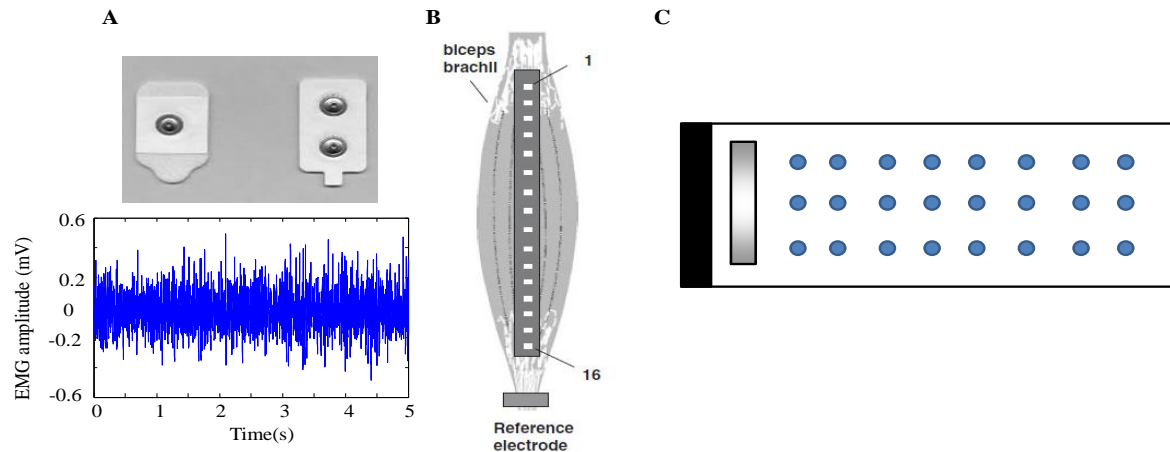
Fig. 2.11 A. Surface electrodes and surface EMG signal over the BB with the arm abducted and a weight at the wrist corresponding to 20% of maximal voluntary contraction. B. Linear array combination of surface electrodes (from [36], p.181). C. an electrode array of 3 x 8 electrodes used to collect signals around the arm as used in [8].
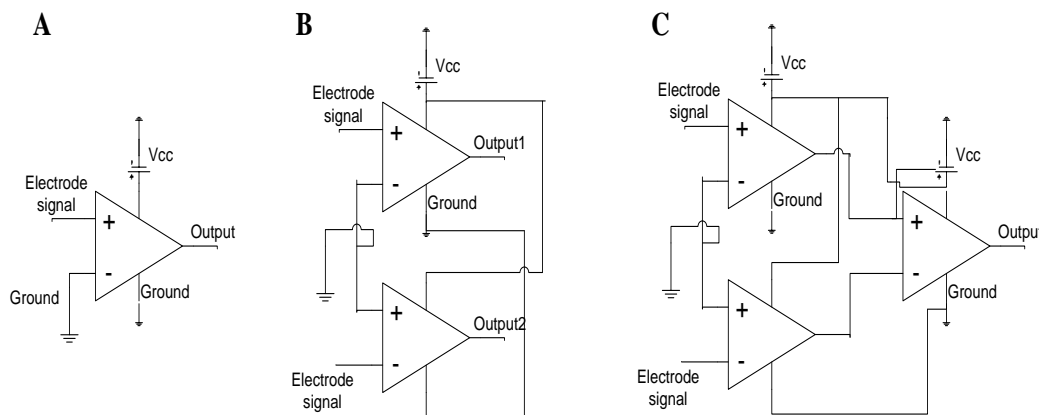
Fig. 2.12 Different recording of EMG signals A. Monopolar B. Single differential (SD) C. Double differential (DD) (from [3], p.181)

2.3 Direct Problem

Relatively few activities have been carried on the direct and inverse problem in the EMG field as compared to ECG and EEG. However, since the generation of those 3 signals have similar electrophysiological basis, the approaches used in ECG and EEG can thus be of great help for the EMG situation. A pioneer in the field, Plonsey [45] produced in 1977 a tutorial paper where he quantitatively described how, in cylindrical nerve or muscle fiber; the extracellular field are related to the underlying current sources.

At that time, only simple characteristics of the medium through which the signal propagates (volume conductor) where considered (i.e. unbounded, homogeneous, and isotropic). Spheres where initially used as a representation of the heart and the head but since the ECG signals were collected on the torso, the cylinder appeared as a more realistic shape. Cylinders without top and bottom (unbounded) or with top and bottom (bounded) where then considered (Burger et al [4]). It is within that context that Frank [16] conducted experiments with a tank filled with a conductive medium in which a dipole representing the heart was placed on or off the cylinder's axis. Modeling an infinite cylinder, he obtained a good match between the theoretical results and the experimental data. Efforts were also directed at solving the equations used in those models. For instance, Okada [42] developed a simpler computational method than Burger [4] and got similar results. As for Lambin and Troquet [30], they solved, with the Green's function, the Poisson's equation for a dipole positioned anywhere within a finite length cylinder filled with an homogeneous medium.

With computer availability, various numerical approaches were developed to facilitate the solution of the equations of Laplace and Poisson. To evaluate the available methods for the forward problem, Heringa et al. [26] compared the finite difference method, the discretized integral equation method and the analytic method when applied to a source distributed along the axis of a bounded cylinder filled with an homogeneous medium. Advantages and disadvantages of the 3 methods considered are presented in Table 2.1.

Table 2.1. Comparison between the finite difference method (FDM), the discretized integral method called boundary element method (BEM) and the analytic one (Analytic). (from [26], Table 1)

	FDM	BEM	Analytic
Anisotropies	Yes	No	Should be defined in the same coordinate system. e.g. Cartesian or Cylindrical
Inhomogeneity	Yes	Restricted	
Boundary Condition	Yes	Simple ones	Simple ones
Storage memory	Large	Intermediate	Low
Convergence	Slow	Intermediate	Fast
Complexity	Simple	Difficult	Difficult

Effect of a finite limb dimension within which muscles have a finite length on the modelisation of motor unit action potentials (MUAPs) was studied by Gootzen et al. [18]. They used an analytical method and their volume conductor consisted of an inner compartment representing a resistive anisotropic muscle, an outer less conductive isotropic compartment to model the subcutaneous fat tissue and finally air is all around this volume conductor (Fig 2.13). Their results indicate that for a good simulation of MUAPs that can be detected at an increasing distance from the skin surface, considering a finite limb and muscle dimensions is a necessity. Trying to model EMG data collected over the BB with a two compartments model, Blok et al [1] found inconsistencies which prompt them to add a third layer to represent skin tissue (Fig 2.14A) In an homogeneous and isotropic volume conductor, they simulated the effect of increasing fiber
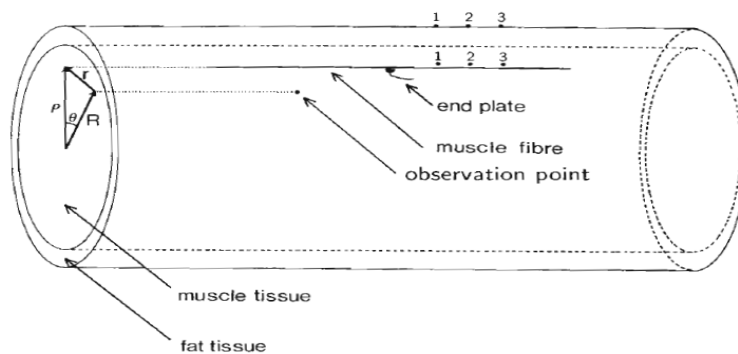
Fig. 2.13 Two concentric cylinders of finite dimensions to model singlr fiber extracellular action potential. Inner cylinder represents the muscle tissue considered anisotropic, Outer cylinder to model the fat layer is isotropic (from [18], p. 153).

depth on the potential at the skin surface. As shown in Fig 2.14B, the downward wave at the end of the simulated signals represents the effect of the tendon when the active fiber is located deep in the volume conductor. When the fiber is near the surface, its propagating signal is large and the effect of the tendon is then barely visible. In Fig 2.14C, by comparing the MF and M curves, it can be seen that the fat layer contributes to the increase of the potential amplitude and reduces its width. The opposite effect happens for the effect of the skin tissue which reduces the amplitude and increases its width. The combined effect of fat and skin thus depends on the relative thickness and conductibility of each layer. Using the 3 layers model, they found that the rate of amplitude decline over the circumference of the cylinder with increasing source depth was similar for both the experimental data and the simulated signals (results not shown).
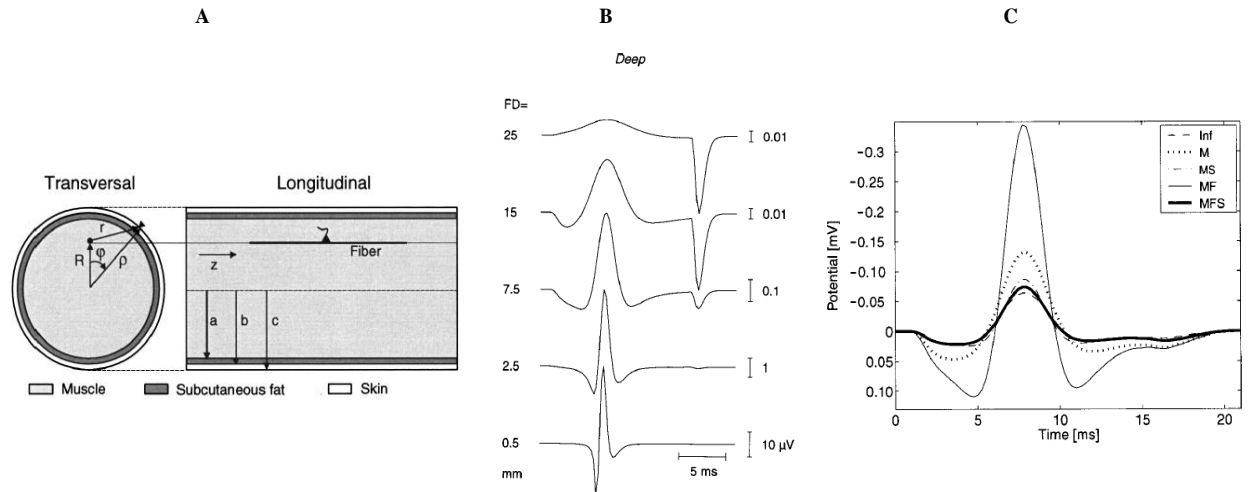
Fig 2.14 **A**: Three concentric cylinders simulating muscle tissue, fat and skin layer. The inner cylinder represents the anisotropic muscle the middle one the fat and the third one the skin both considered isotropic. R represents the distance of an active fiber from the center of the model and r the distance between the fiber and the surface of the model. ϕ is the angle between the active fiber and the point of measurement and ρ is the radius to the skin surface. In the longitudinal view, *a* is radial distance of the active fiber. *b* is the radial distance to the upper limit of the fat layer and *c* (equal to ρ) is the distance to the skin. The source is represented by the horizontal fiber with its neuromuscular junction at its center. **B:** Simulated signals when the active fiber is placed at various depth (FD) in an homogeneous volume conductor. The downward peaks (to the right of the signals) are associated to the effect when the AP reaches the tendon. **C**: Simulation results for a motor unit composed of 300 fibers at a depth of 5 mm under the skin when the volume conductor is considered to be composed of only an anisotropic muscle compartment (M), of a two-layered model of muscle and fat (MF) or muscle and skin (MS) and for a three layered model (MFS); (from [1], Fig.1, 2 and 3).

For Farina et al. [14], air surrounding a limb is considered as a fourth layer to be added to muscle tissue, fat and skin layers. They then calculated the potential distribution over the skin, due to sources in the muscle by solving the Poisson equation in the spatial frequency domain. The model is based on a cascade of low-pass spatial filters representing the anisotropic muscle tissue and the isotropic fat and skin layers. The results illustrated the effect of the sub-cutaneous tissue layers increase the detection volume in all directions and reduced its amplitude (Fig 2.15). To compensate the attenuation and widening of the signal due to the subcutaneous tissue, various recording electrode arrays such as shown in Fig 2.16A could be used. The transfer functions of anisotropic muscle tissue and the isotropic layers of fat and skin is shown in Fig 2.16B.
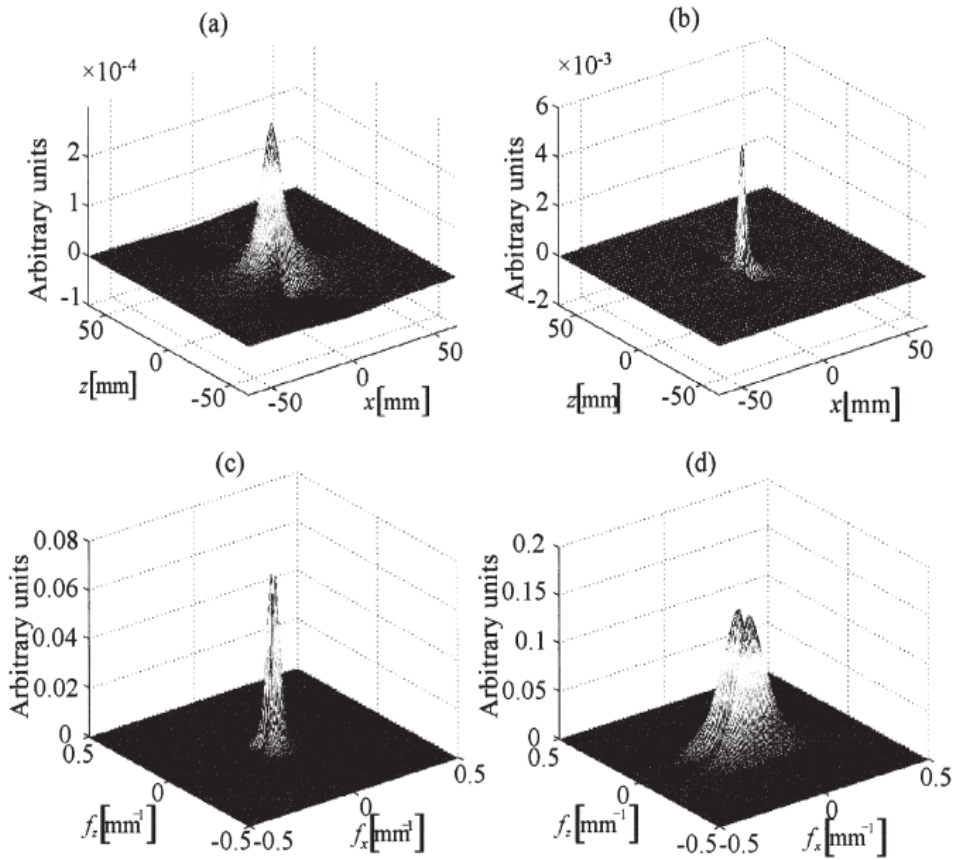
Fig. 2.15. Spatial and spatial frequency domain potential distributions at the skin surface (a and c) and directly over the muscle (b and d) as generated by a fiber located at 2 mm under the skin Simulated thickness of 3 and 1 mm was respectively used for the fat and skin layers, A current tripole with wirh a length of 7 mm represented the depolarized zone of the fibers. (from [14], Fig.3),
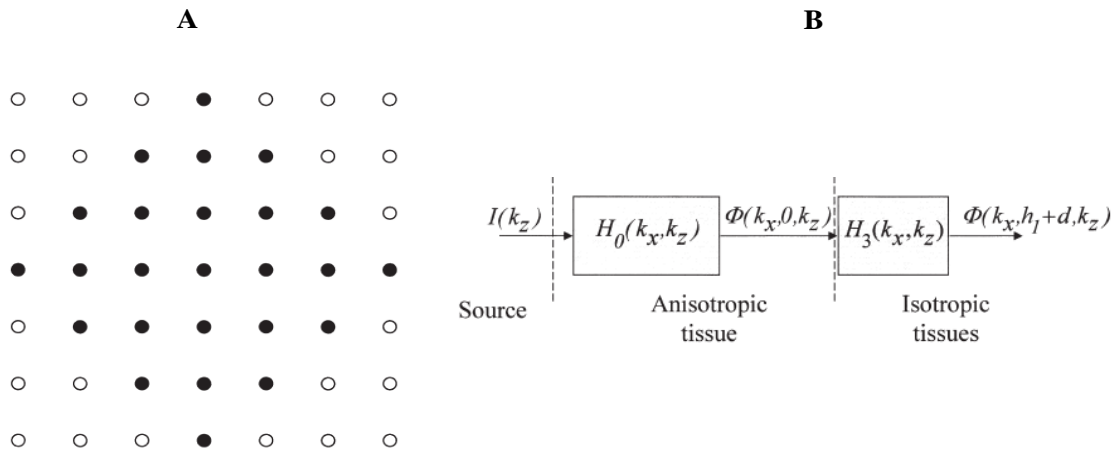
Fig 2.16. A: Structure of a spatial electrode matrix. The weights of the filled circles were varied according different filters and the weights of white circle were zero. B: Block diagram of anisotropic tissue and isotropic tissue (fat and skin). (from [14], Fig 2 and 8).

Pursuing on how the modeling of the volume conductor interacts with spatial filters, Farina et al. [13] studied the spatial selectivity offered by various electrodes configurations in order to separated pr opagating (APs travelling in muscle fibers) and non-propagating signals (generation of the APs at the neuromuscular junction and their extinction at the tendons). They considered 3 different anatomical configurations as shown in Fig. 2.17a. In b of that figure, a lateral view of the volume conductor with a finite-length muscle fiber placed near the detection surface at a position located between the end-plate (neuromuscular junction) and the tendons. As shown in Fig.2. 17c, three different spatial filters where considered: the longitudinal single (LSD), double (LDD) and normal double differential (Laplacian, NDD). By combining those spatial filters and various thicknesses, 13 different configurations were analyzed with an analytical model simulating the generation, propagation and extinction of an IAP within the muscle fiber. Effects of the configuration of the electrodes on the transverse selectivity (around the cylinder away from the electrodes) and on the depth selectivity (effect of the depth of the active fiber) were considered.
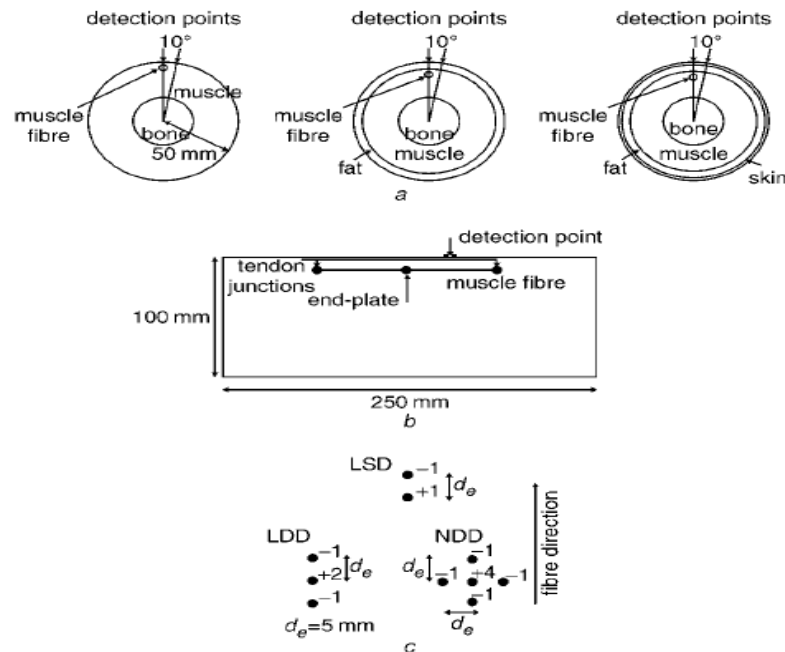
Fig. 2.17.Volume conductor models with bone-muscle, bone-muscle-fat, and bone-muscle-fat-skin. b. Lateral view of the volume conductor with simulated finite-length muscle fibre which varied between 30 and 50 mm. The detection point represents the position of the middle electrode of LSD, LDD and NDD. It is positioned in the middle between the end-plate and a tendon. c. Configurations of 3 filters with their associated weights for each electrode. (from [13], Fig 1).
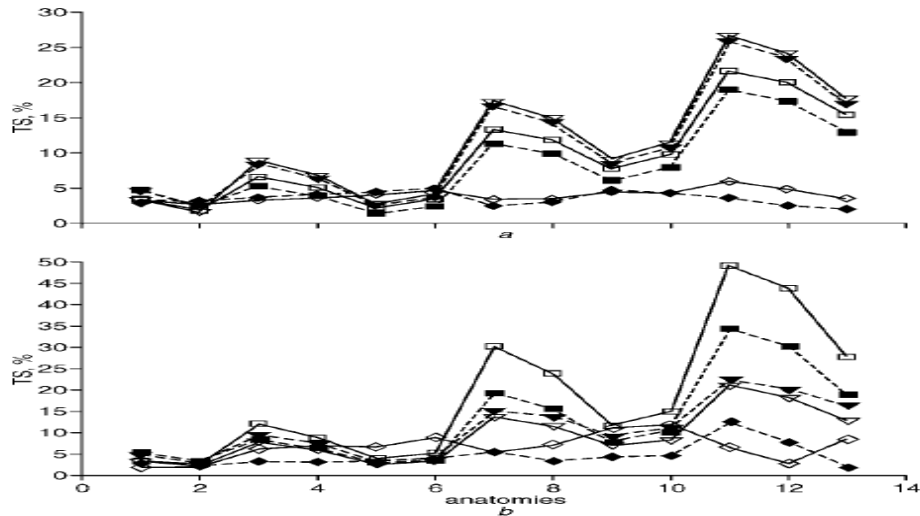
Fig 2.18 Transverse selectivity (TS) between peak-to-peak amplitude of signals generated by the muscle fiber at 0 ° and 10 ° in the transverse direction relative to the detection system as simulated in different anatomical conditions. The muscle fiber is simulated with a 50 mm length and at a depth of 1 mm in the muscle Moreover the inclination angle between muscle fiber and detection system was 0 ° or 15 °. b. TS when length of fiber was 30 mm. (◆) NDD; (▼) LSD; (■) LDD. (◇) NDD, 15 ° of misalignment; (▽) LSD, 15 ° of misalignment; (□) LDD, 15 ° of misalignment. (from [13], Fig 5).

In Fig.2.18, results indicate that propagating as well as non-propagating signal components are highly influenced by the model considered. LSD, LDD and NDD show similar performance with some anatomies (e.g. when the fat and skin was not considered), whereas they perform significantly differently with other situations. When the radius of bone, muscle, fat and skin layers were assumed to be 20, 28 and 1mm respectively, by increasing the lateral displacement of the detection system from 0° to 10°, the propagating components are approximately reduced to 2% with LSD and LDD and to 4% with NDD. By increasing the fat layer to 5 mm and reducing the muscle to 24 mm, LSD and LDD reduce the signal amplitude to approximately 25% and 20% respectively, whereas, with NDD, amplitude decreases to 4%.

As expected, when isotropic layers of fat and skin are added, there is a decrease in selectivity in propagation component. For the nonpropagation components, NDD is generally less selective than LDD and LSD but the importance of the difference depends on the anatomy model considered. For the propagation components, LSD and LDD may be more or less selective than NDD depends again on the volume conductor model. In an article aimed at extracting neural strategies from surface EMG, Farina et al. [12] surveyed the various factors which can affect the

features of the surface EMG signal. Among those shown in Table 2.2 crosstalk which is contamination of a signal recorded over one muscle by those generated by other nearby muscle(s), can be significantly reduced by the spatial filtering made by an electrodes configuration.

Table 2.2. Factors that influence the surface EMG (from [12], Table 2)

Factors That Influence the Surface EMG	
Nonphysiological	
Anatomic	Shape of the volume conductor
	Thickness of the subcutaneous tissue layers
	Tissue inhomogeneities
	Distribution of the motor unit territories in the muscle
	Size of the motor unit territories
	Distribution and number of fibers in the motor unit territories
	Length of the fibers
	Spread of the endplates and tendon junctions within the motor units
	Spread of the innervation zones and tendon regions among motor units
	Presence of more than one pinnation angle
Detection system	Skin-electrode contact (impedance, noise)
	Spatial filter for signal detection
	Interelectrode distance
	Electrode size and shape
	Inclination of the detection system relative to muscle fiber orientation
	Location of the electrodes over the muscle
Geometrical	Muscle fiber shortening
	Shift of the muscle relative to the detection system
Physical	Conductivities of the tissues
	Amount of crosstalk from nearby muscles
Physiological	
Fiber membrane properties	Average muscle fiber conduction velocity
	Distribution of motor unit conduction velocities
	Distribution of conduction velocities of the fibers within the motor units
	Shape of the intracellular action potentials
Motor unit properties	Number of recruited motor units
	Distribution of motor unit discharge rates
	Statistics and coefficient of variation for discharge rate
	Motor unit synchronization

While simulation results indicate that LSD or LDD spatial filter would be more transversely sensitive than NDD, the inverse had been reported from experiments on some muscles among which the biceps is found [12].

In a review article on the relation between physiological processes and surface EMG Farina et al. [14] used a 4 layers model (Fig 2.19A) to simulate for the upper limb, the effects of 2 muscle

lengths and two fat thicknesses on the surface signal characteristics. As illustrated in Fig 2.19B and C, the peak value of the power spectrum is shifted to lower values as fat thickness increased and when position of the source is changed relative to the detection point. In panel D, the same conditions as in C is shown except that the fiber length is shorter which results in broader spectra because of the prevalence of non propagating components. However, mean frequency decreases as the depth of the source is increased.
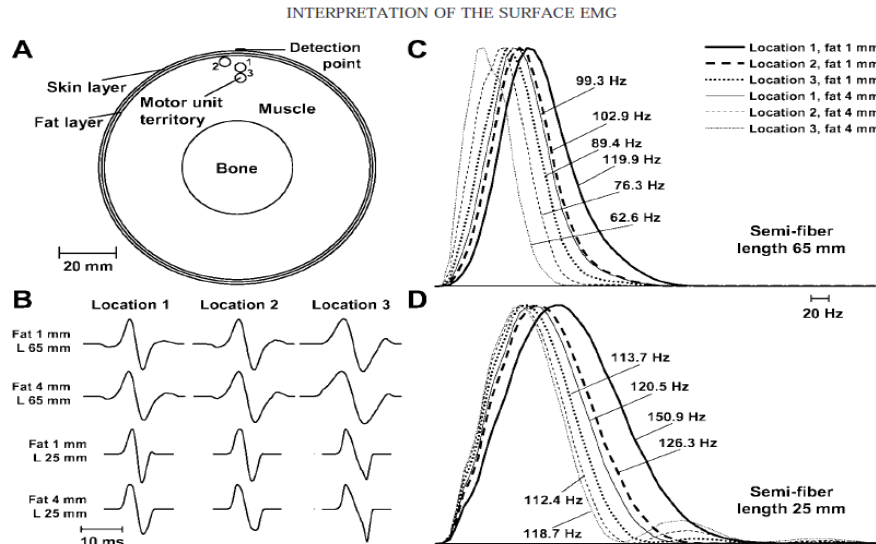
Fig. 2.19 *A*: Simulation of single MUAP measured with a pair of electrodes placed between the innervation zone and a tendon. The MU was placed in 3 positions within the muscle and occupies a circular territory (radius of 2 mm). It innervated 250 fibers with a density of 20 fibers/mm². Locations *1* and *2* were at the same distance from the detection point, whereas location *3* was 4 mm deeper. Four conditions were considered: semi-fiber length of 65 and 25 mm and fat thickness layers of 1 and 4 mm. Conduction velocity was 4 m/s. *B*: Changes in MU potential waveform (normalized maximum values) due to the influence of fiber depth, fat thickness and fiber length. *C and .D*: Power spectral densities of the MUAPs in different conditions. The bandwidth of the power spectrum was broader for shorter fibers (*D* vs. *C*). The distance from the detection system is not the only parameter to influence the power spectrum, for example, the power spectra at locations 1 and 2 are different. The depth of the source may decrease the mean frequency which may increase for large distances, especially when the fibers are short, because of the prevalence of nonpropagating components. Despite a constant conduction velocity, the frequency bandwidths were significantly different in the 12 cases (2 fiber lengths from 50 to 130 mm, 3 locations of MU 2 fat thicknesses from 1 to 4 mm). (from [14]. Fig 5).

Considering that surface EMG models do not take into consideration that the volume conductor is not space invariant, Mesin et al [37] introduced spheres of different conductivities in the volume conductor. With an analytical solution, they found that the spheres modified the signal propagation (Fig 2.20) and reduced the amplitude of the detected signals
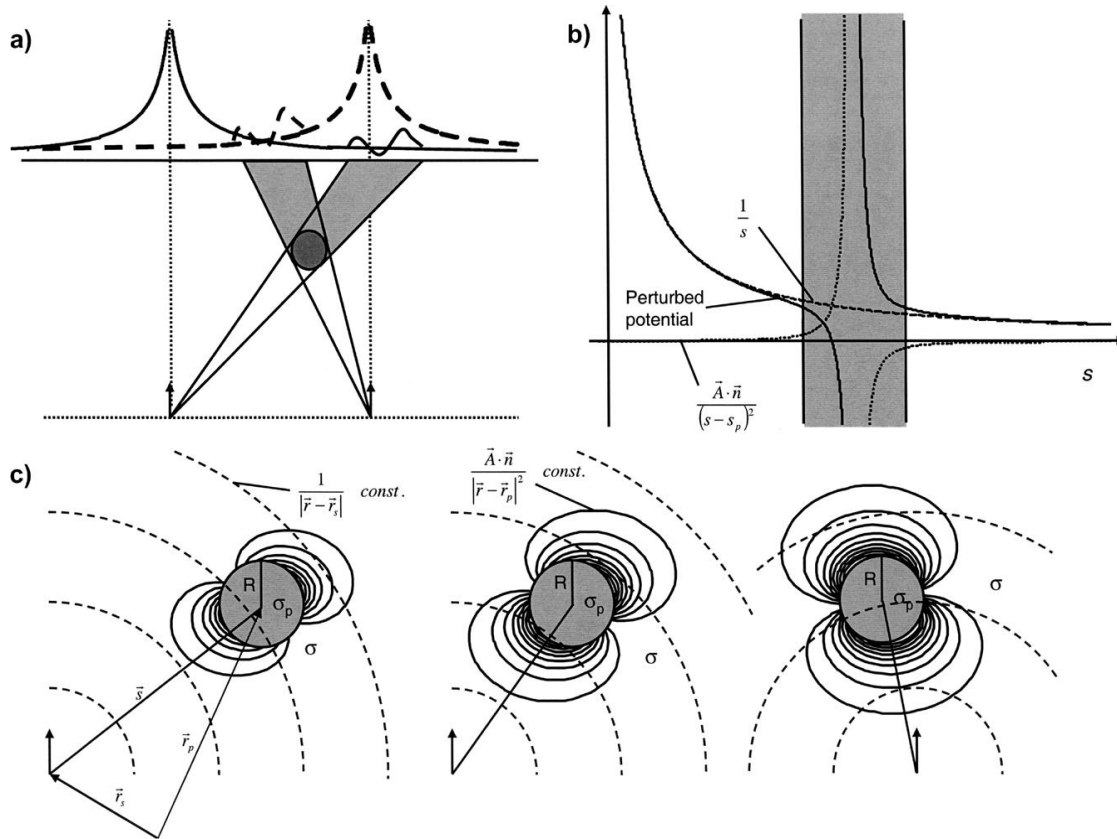
Fig.2.20 Insertion of a circular inhomogeneity in an otherwise homogeneous volume conductor perturb the surface potential. a) Perturbation (small amplitude wiggles) on the impulse response associated when the source is at 2 different locations. b) Signal associated of the impulse current source alone (1/s) and with the perturbation induced by the sphere $(A.n/(s-s_p)^2)$ where A is related to the conductivity in each axis of the sphere. Perturbation effect decays rapidly as the distance from the inhomogeneity is increased C) Contours of the perturbation effect for 3 positions of the current source (from [37], Fig 1).

The effects of the presence of the homogeneity at 2 positions relative to the detection point (Fig 2.21a) on the surface signal detected with 4 different electrode configurations (Fig 2.21b) is shown in Fig 2.21c. The results show that sensitivity to the presence of the sphere depends on its location and to the electrodes configuration. Those results indicate that homogeneities has to be considered when elaborated volume conductors are considered but the perturbation effect of inhomogeneities decreases as the inverse of the square of the distance from the detection point. It has also to be noted that the perturbation travels on the signal in opposite direction to the direction of the propagating source.
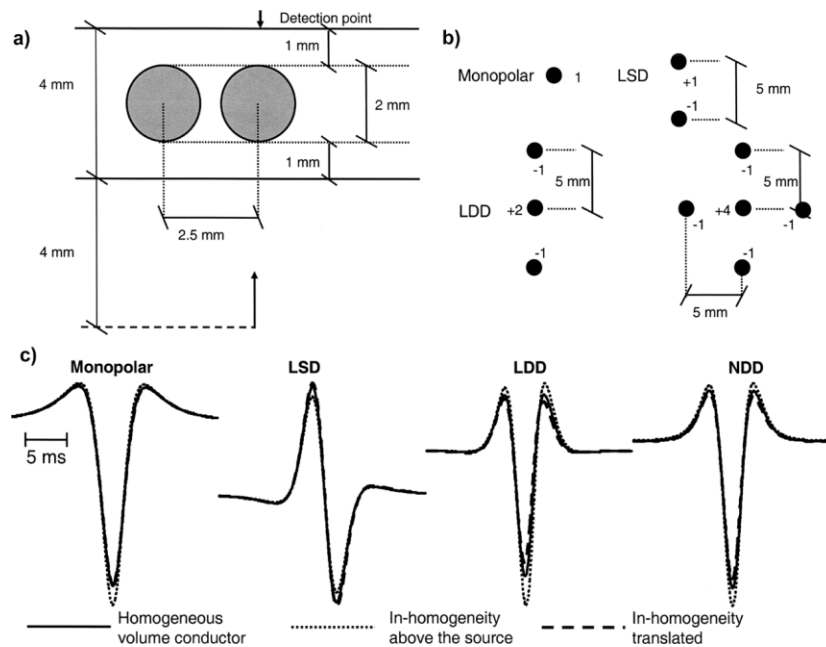
Fig 2.21 a) volume conductor perpendicular to the active fiber with an inhomogeneous sphere placed at two positions relative to the detection point. b) Four spatial filters were considered: monopolar recording, longitudinal single differential (LSD), double differential (LDD) and normal double differential (NDD). c) Signals obtained with the 4 spatial filters under 3 volume conductor conditions: without, with the inhomogeneity above the detection point, the sphere translated by 2.5 mm (from [37], Fig 6).

In a more practical orientation of the use of direct and inverse modeling, Kuiken et al [29] use the approach with the aim of improving the control of artificial arms by using nerve grafts following an important amputation of the upper limb. To be successful, the EMG signals following the nerve–muscle grafts need to be independent of each other and the presence of crosstalk minimized. They used as an experimental phantom arm, a cylinder of 10x 30 cm for its diameter and length which was filled with ground cooked meat. Eight pairs of 6 mm diameter electrodes were equally spaced around the periphery of the phantom. Four pairs of spherical spheres of 4 mm were placed at different levels inside the cylinder on its axis with different distance of their poles. A 150 Hz sinusoidal signal, close to the mean value of the surface EMG spectrum, was used as the excitation source for the electrodes pair either placed inside or outside the cylinder.

In parallel with the phantom, they developed a finite element model (FEM) to simulate the results obtained with the phantom. An homogeneous and isotropic volume conductor was used. With a total of 51800 elements either linear or quadratic tetrahedral results with satisfactory accuracy were obtained. Experimental data and simulation results were found in good agreement.

A sample of their simulated cylinder with potential distribution over the recording electrodes when the source was on the cylinder surface is shown in Fig 2.22.A while a transverse view at the level of the recording electrodes is shown in Fig 2.22B. With an error in signal magnitude generally <5%, correlation between the FEM data and the experimental cylinder data was very high (0.99). When simulations were performed using muscle dielectric properties and using static, complex, and full electromagnetic solvers, a significant displacement currents was detected (50% of total current) and the fall-off of surface signal power varies depending on how the signal source was modeled. So, while most EMG models are quasistatic or stationary models where only the resistive component of tissue impedance is considered. The simulation results of those authors point to the potential importance of the capacitive properties of biological tissues since permittivity of biological tissues are generally very high even at low frequency.

Also using a FEM model, Lowery et al. [34] investigated the effects of skin, subcutaneous fat, muscle, bone structures on surface EMG signal generated by an active muscle fiber with a diameter of 50 µm located 10 mm below the skin as shown in Fig 2.23. The muscle was considered homogeneous and anisotropic while the fat and skin layers are isotropic. Assuming a resistive only medium and a quasi-stationary situation (no induction, no capacitive effects), the Laplace's equation was used. For the FEM model, the skin was represented with quadrilateral elements while 3D tetrahedral ones were used to mesh the interior of the model. For the muscle fibers, the size of the elements was 0.05 mm but increased up tp to 12 mm for other components. Depending of the complexity of the muscle geometry, 300 000 to 600 000 elements were used. Five models (Table 2.3) were considered.
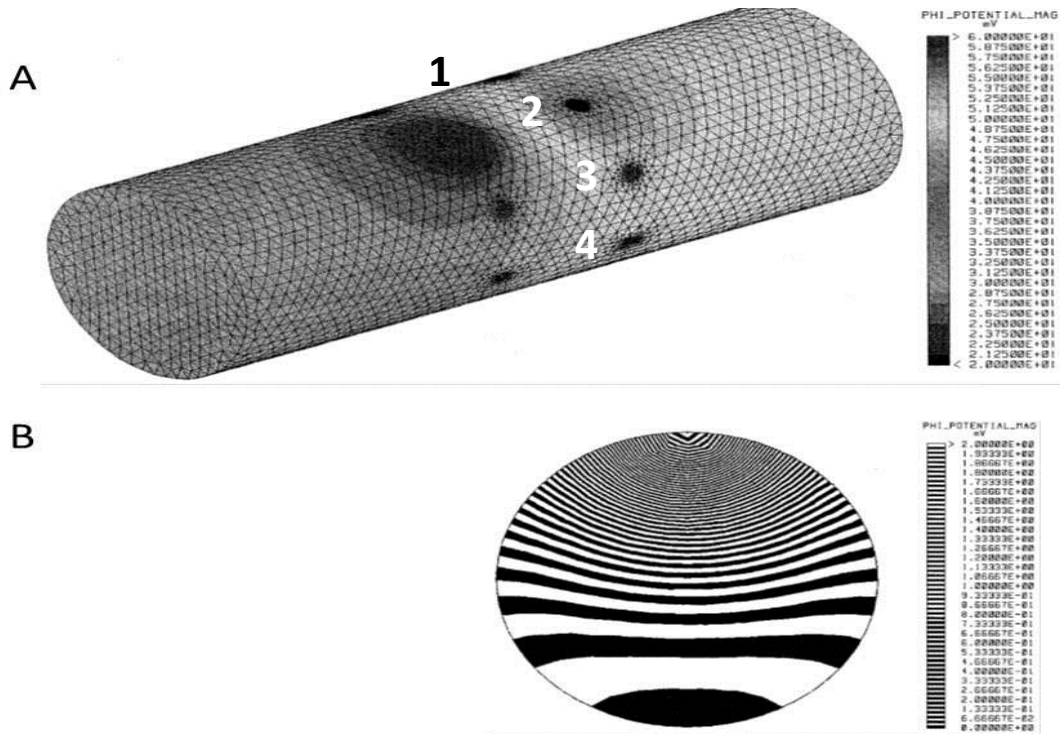
Fig. 2.22 A: Surface electrode potential over the phantom as obtained with a FEM model. Potentials calculated at the 4 visible recording sites is shown as small black zones. The excitation source (large black zone) was placed at the periphery of the cylinder. B: Transverse view of the potential distribution. Many isopotential lines are observed near the source and their convexity decreases to become concave near the opposite border of the cylinder (from [29], Figs.2 and 3).
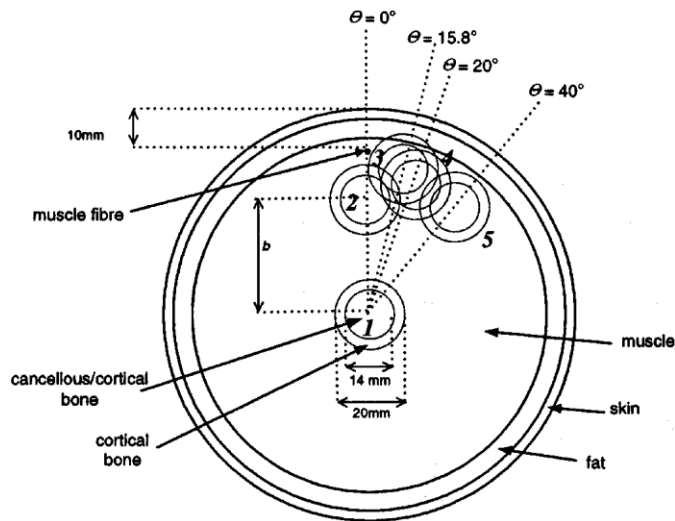
Fig. 2.23 Cross section of the 4 components model (bone, muscle, fat, skin) with the 5 positions considered for the bone and where b is the distance between center of the volume conductor and center of the bone. θ represents the angular displacement of the bone from the source. The bone has a cortical annulus around a less resistive cancellous circle. Position of the active muscle fiber is 10 mm below the skin surface (from [34], Fig 2).

TABLE 2.3:   TISSUE COMPOSITION OF MODELS I–V (from [34], Table 2)

	Model I	Model II	Model III	Model IV	Model V
Region 1	muscle	muscle	muscle	muscle	bone
Region 2	muscle	muscle	muscle	muscle	muscle
Region 3	muscle	muscle	fat	fat	fat
Region 4	muscle	skin	fat	skin	skin
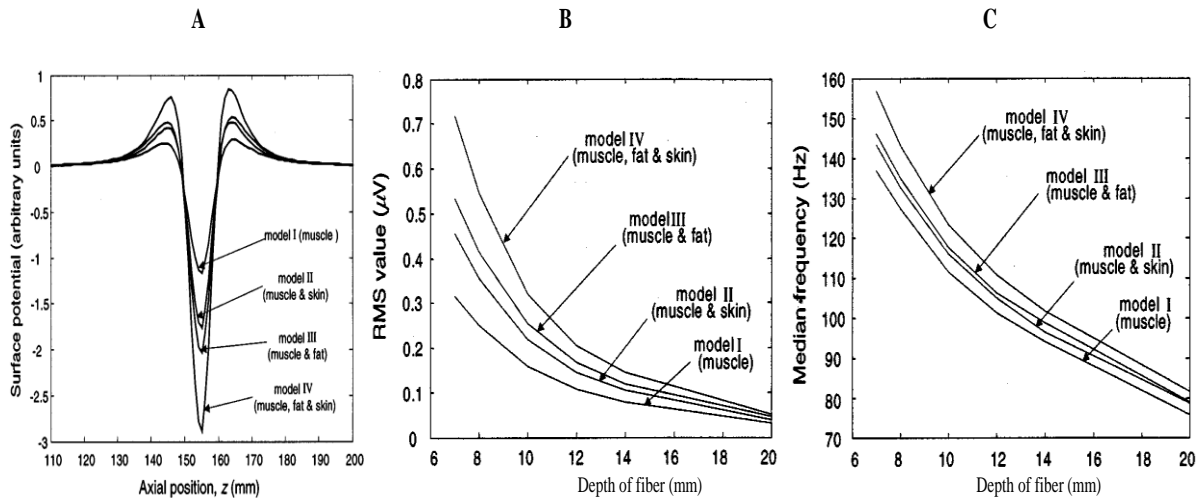
Fig. 2.24 A. Action potential detected the surface of fiber in 4 of the models of Table 2. B. For each of the 4 models, RMS value of surface potentials above the active fiber as its depth increased. C. amplitude of spectrum median frequency of surface potential when fiber depth increased (from [34], Fig 3.4).

As illustrated in Fig 2.24.A, the presence of skin and fat increases the amplitude of surface EMG signal. The effects of each of the 4 models as the depth of the active fiver increased is illustrated in Fig 2.24B and C for the RMS value and median frequency amplitude of the signals. Muscle anisotropy was introduced by increasing the axial conductivity of the muscle tissue in model I and IV. As can be seen in Fig 25 both amplitude and frequency content decreased as the muscle anisotropy increase.
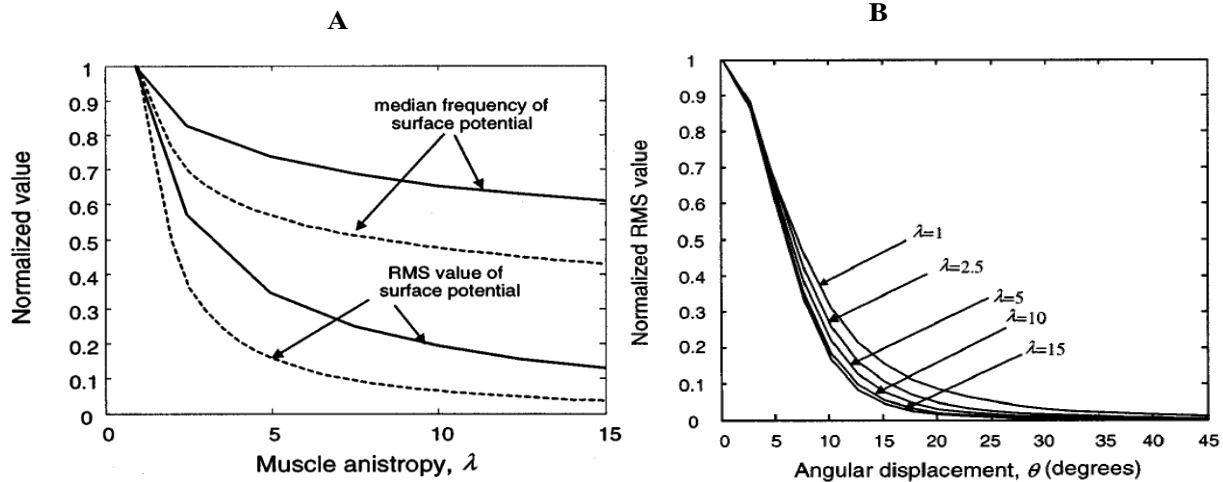
Fig 2.25 A: Comparison of the RMS value and median frequency in model I (solid line) and model IV (dashed line) by increasing the muscle anisotropy B:Rate of decay of surface potential RMS value is considered by increasing angular displacement from the source, as muscle anisotropy is varied (from [34], Fig 6,7).

When bone is at the center of the model, its effect on the skin surface is small for both parts of the bone. When at position 2, the surface EMG amplitude increased with a small difference for the two bone parts. Similarly, when the bone was placed close to the muscle or fat (positions 3–5), the RMS value of the surface potentials increased between the source and the bone but decreased slightly elsewhere. The effects of fat thicknesses varying from 0 to 18 mm was analyzed with an active fiber located at 3 mm below the muscle-fat interface, the RMS value and the frequency content of the simulated surface EMG signals increased with fat thickness due to its high resistivity.
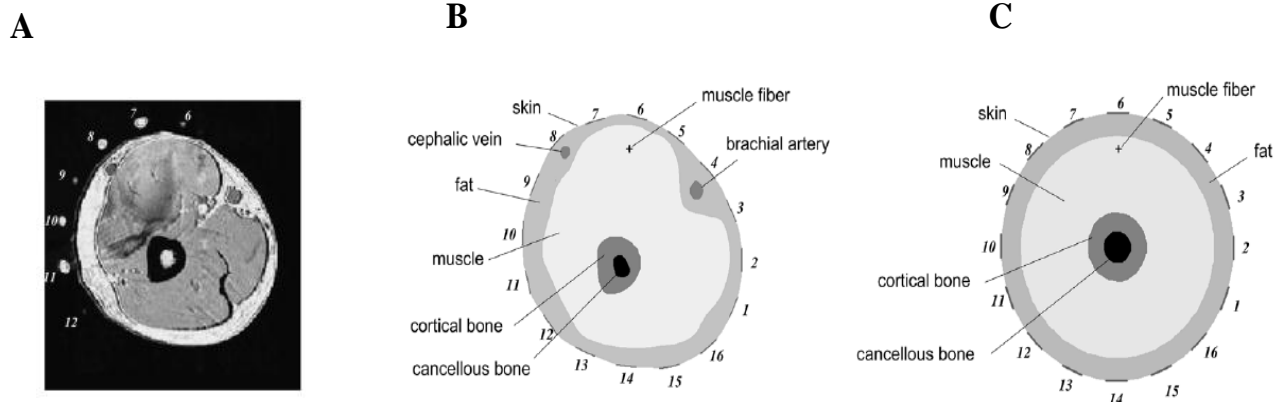
Fig 2.26 A. Magnetic resonance image of a transverse section of an human upper arm. The white small circles show the positions of the electrodes used in the EMG recording session. B. Image model of MRI. C: idealized cylindrical model of the image at the left (from [33]. p. 2140).
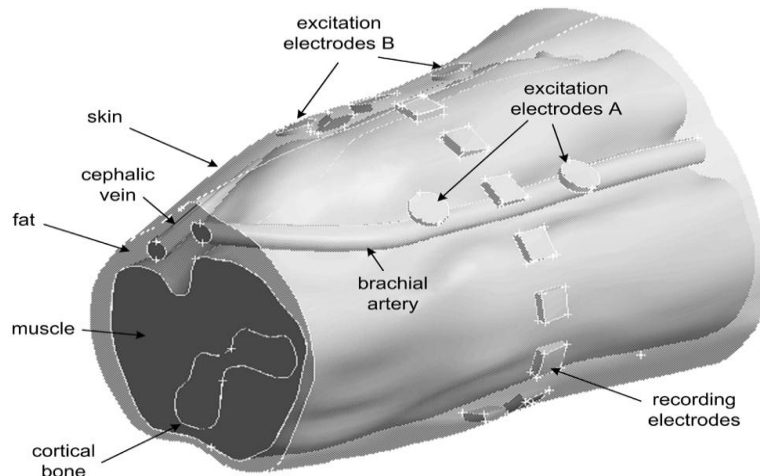
Fig. 2.27. An anatomical based volume conductor. and location of excitation and recording surface electrodes (from [33], Fig 2).

For a model closer to the reality than a cylinder, Lowery et al [33] used a resonance magnetic image of the upper arm of a normal subject (Fig 2.26.A). The derived FEM model is shown in the B panel of the figure. For comparison, a cylindrical model is shown in C. Sixteen pairs of 10×1 mm silver bars spaced by 10 mm were placed around the upper arm. As an excitation signal, a 1 mA sinusoidal current at 100 Hz was applied to 2 pairs of pregelled circular electrodes (10 mm): one pair was placed close to recording electrode pair 4 and the other on either side of electrode pair 7 (Fig 2.27). Distance between adjacent nodes of the mesh varied from 0.1 mm, along the muscle fiber, to 8 mm deeper within the volume conductor. Different values of conductivity and relative permittivity of tissue, fat, skin and bones were considered and 5 situations were considered (Table 2.4).

Simulations were done with a curved and a straight muscle fiber in the real shape of upper arm (Fig 2.26B) and for a straight fiber in the idealized cylindrical model (Fig 2.26C). Fig 28 illustrates the results obtained at the skin surface when an active fiber was located 14.5 mm below. As it can be seen in the 8 result panels, the volume conductor geometry and the curvature of the fiber have important effects on the shape and amplitude of the simulated surface potentials between recording sites. While accurate modeling of limb geometry, including tissue capacitance and of fiber curvature are important for a precise description of surface potentials, the use of the

idealized cylindrical volume conductor with subcutaneous layers gives a good approximation of the surface signal reduction as the source depth is increased.

Table 2.4: Conductivity (σ) and relative permittivity (ε) of muscle, fat and skin tissue as obtained in the litterature making 4 realistic models to be compared to the idealized one (from [33], Table I).

Model	Muscle longitudinal direction		Muscle transverse direction		Fat		Skin		Mean rms error	
	σ_l (S/m)	ε_l	σ_t (S/m)	ε_t	σ_f (S/m)	ε_f	σ_s (S/m)	ε_s	Excitation 4	Excitation 7
A	0.30 [a]	3×10^7 [a]	0.20 [a]	1×10^7 [a]	0.04 [a]	1.5×10^5 [a]	4.3×10^{-4} [a]	4.5×10^4 [a]	69.59%	134.48%
B	0.52 [b]	1.1×10^6 [b]	0.076 [b]	3.2×10^5 [b]	0.07 [b]	1.5×10^5 [b]	4.3×10^{-4} [a]	4.5×10^4 [a]	29.76%	28.95%
C	0.40 [c]	2×10^7 [c]	0.09 [c]	4.4×10^6 [c]	0.04 [a]	1.5×10^5 [a]	4.3×10^{-4} [a]	4.5×10^4 [a]	26.61%	18.00%
D	0.40 [c]	2×10^7 [c]	0.09 [c]	4.4×10^6 [c]	0.04 [a]	1.5×10^5 [a]	2.2×10^{-2} [d]	4.0×10^5 [d]	26.15%	20.40%
Idealized	0.40 [c]	2×10^7 [c]	0.09 [c]	4.4×10^6 [c]	0.04 [a]	1.5×10^5 [a]	4.3×10^{-4} [a]	4.5×10^4 [a]	31.5 %	29.2 %

In summary, the reviewed models span from a single cylinder (Heringa et al. [26]) up to 4 concentric layers (Farina et al. [13]). In such models, characteristics of the media are considered to be space invariant except for the 2 layers model of Mesin and Farina [37] where a sphere is inserted to make the volume conductor space variant. Beside analytical methods usually considered to solve the direct problem when cylindrical forms are used, Kuiken et al [29] used the FEM. In search of a more realistic representation of an arm cross-section, a magnetic resonance image was used to produce a more elaborate FEM model (Lowerey et al. [33]). Among those models we considered that the four-layered concentric cylinder model of Farina et al. [13] appeared as the best choice for the localisation of dipoles at the origin of EMG signals collected over the short and long head of the BB. In such a model, the muscle mass is considered homogeneous and anisotropic while fat and skin layers are isotropic. Availability of conductivity and thickness values for each layer being available in the literature is an additional advantage for such a model. Finally, an analytical solution can be easily implemented to calculate the surface potentials resulting from current sources placed within the muscle volume. Compared to numerical methods, the analytical approach offers more accuracy and results are obtained more rapidly.
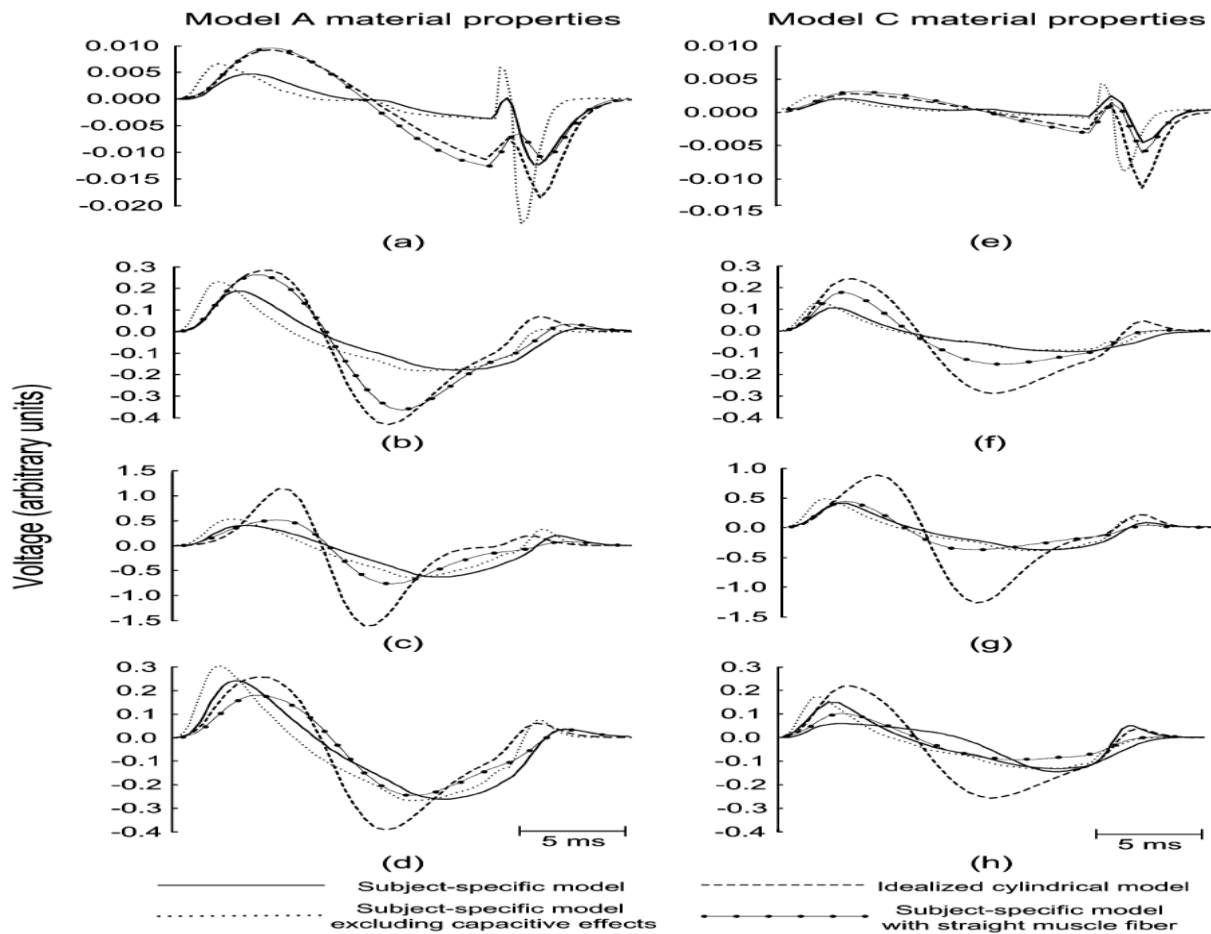
Fig. 2.28 Simulated surface AP for a fiber is located 14.5 mm below the skin surface and under electrode pair 6. Left and right columns of results are for 2 different material properties. .Results from the upper row to the lowest one are respectively signals amplitude under electrode pairs 2, 5, 6 and 7. In each of those 8 panels, four different conditions where experimented as indicated at the bottom of the figure. (from [33], Fig 4).

2.4 INVERSE PROBLEM

As for the direct problem, solutions for the inverse problem in EMG are inspired by approaches developed either for ECG or EEG. To solve the inverse problem in those two fields the situation is either considered as under-determined or over-determined. A priori information can be introduced through regularization parameters associated to different functions leading to different methods such as Minimum Norm (MN) [38]. MN method is recommended for superficial sources but deeper sources are incorrectly identified. When the regularization parameters are combined with the Laplacian method (Laplacian weighted minimum norm) the MN method became known

as the weighted minimum norm (WMN) [20]. This method is implemented in the LORETA software [43] which is freely downloadable. When additional constrains are applied with physiological information, the software is then called local autoregressive average (LAURA) [19]. The Beamformer method, used for radar and sonar signal processing can also be used in an under-determined problem as Gross et al [21] did for the analysis of magnetoencephalography (MEG) signal. Baysian approaches are also used for the analysis of brain signals (Schmidt et al. [49]). When those methods were compared in different conditions, it was found that the methods presented by LORETA software offered the best source localization [17,32].

2.4.1. Over-determined method

This approach is used in linear systems where it is assumed that the number of current sources is less or equal to the number of independent measurements obtained from as many electrodes. Location of these reduced numbers of sources is obtained by the use of a forward model and comparing its results with the experimental measured potential distributions. In this comparison, the average squared error between the experimental and simulated results is minimized which lead to the identification of the best explanation for the collected data. However, finding the best solution within the solution space is time consuming and nearly impossible if more than one dipole is assumed. Non-linear optimization methods based on various algorithms are then required.

As for the EMG signal, it results from the activation of many hundreds of myofibers which can be associated to an under-determined situation. However when several of these myofibers are considered bundled together and assimilated to a single current source, an over-determined condition can be assumed. This approach could be used in our project since we are looking to identify activity within the 6 compartments in the BB with the availability of 10 surface EMG signals collected over the muscle.

The over-determined situation was applied by Saitu et al [48] who determined dipoles position and intensity that could duplicate the characteristics of each MU detected over the upper arm. Experimental MUAPs distributions were obtained with 16 pairs of electrodes placed at various positions across the BB of 3 normal subjects producing isometric low level contractions. The limb was modeled with a semi-finite length cylinder filled by an anisotropic and homogeneous medium. The Poisson equation was solved to obtain the potential distribution around the cylinder used as a model of the arm and quasi-Newton optimization method was used to duplicate the experimental data. From the 3 subjects, 36 different MUAPs were obtained and for each of them, and 5 to 6 dipoles estimated at a depth of 0.3 to 8.0 mm and an intensity of 0.1-5.9 nAm were obtained with the inverse model. An example is given in Fig 2.29 where 3 dipoles are located near the peak of MUAP and the 2 others positioned on the peripheral slopes of the 3D distribution. In this case, the current dipoles were estimated at a depth of 1.7±4.0 mm with intensities of 0.4±3.3 nAm and were spreaded over 8.1 mm perpendicularly to the muscle fibers direction.

The over-determined approach was also used in the feasability study by Chauvet et al. [6] who developed a numerical localization algorithm of MUs from surface EMG. They simulated 16 EMG signals equally spaced over half of the upper arm covering mainly the BB (Fig 2.30). Their forward model is based on a summation of SFAP to obtain MUAPs as shown in Fig 2.30. In the inverse model, which does not use the analytical function used in the direct model, a simple mathematical model was considered and the gradient method was used to minimize the differences between synthetic signals and the inverse model results. Their results are at the effect that an active motor unit in a given zone can be localized regardless of its distance from the electrode location
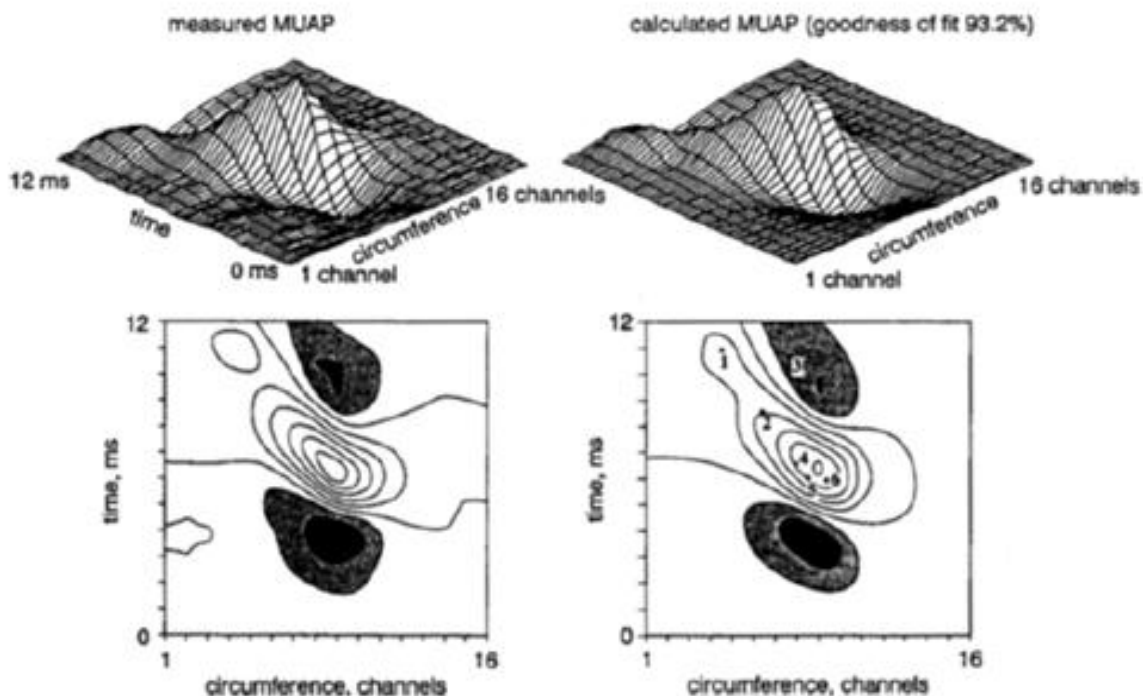
Fig. 2.29 Surface plots of a measured MUAP (upper left) and its contour plot (lower left).The same for a calculated MUAP on the right. For this MUAP, 5 current dipoles were found optimum with the inverse model. Dipoles 3, 4, 5 were located near the peak of the waveform distribution. As for dipoles 1 and 2, they were along the slopes of the potential distribution. The location and intensities of these dipoles are: 1: 3.8 mm deep, 0.9 nAm; 2: 4.0 mm deep, 3.3 nAm; 3: 2.4 mm, 2.5 nAm; 4: 1.7 mm, 0.7 nAm; 5: 3.0 mm, 0.4 nAm (Fig. 5 from [48]).
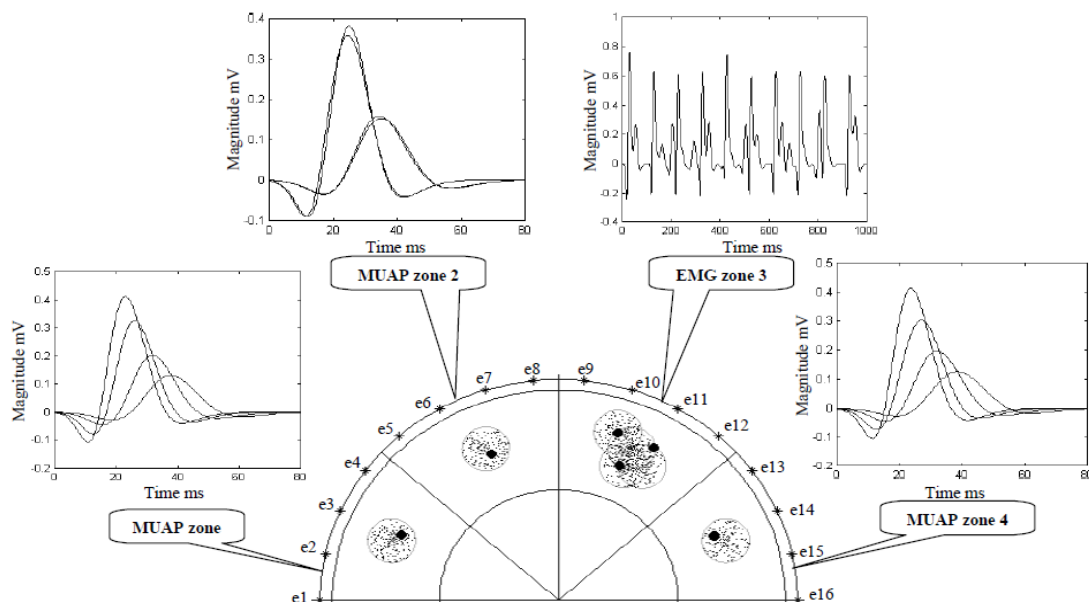
Fig. 2.30 Potentials detected by 16 surface electrodes placed around the upper arm during a weak contraction. The dots (●) locations are the average of the coordinates of current sources which is detected in zone 1, zone 2, zone 4. In zone 3, more than one current sources are present and are scattered (from [6], p 2).

In the previous articles, the volume conductor was considered homogeneous while biological tissues i.e. muscles, bone, fat and skin have different characteristics. To analyze a more realistic situation, Jesinger et al [28] used magnetic resonance images obtained from elbow to shoulder when the BB was contracted to elaborate a FEM of a cross-section of the upper arm (panel C of Fig 2.31). Assuming quasi-static and steady ohmic conduction, considering bone, muscle and fat tissues, they solved the Poisson's equation with the finite element method when the number of sources to be identified was constrained. Experimental EMG signals were obtained over the BB (Fig 2.31A) with 4 mm disc electrodes when various levels of contraction were experimented. Using time-frequency distributions, they considered 46 Hz as to most significant to assign to their current sources. On the slice shown in Fig 2.31C, a dipole within the BB is represented by the small white circle.
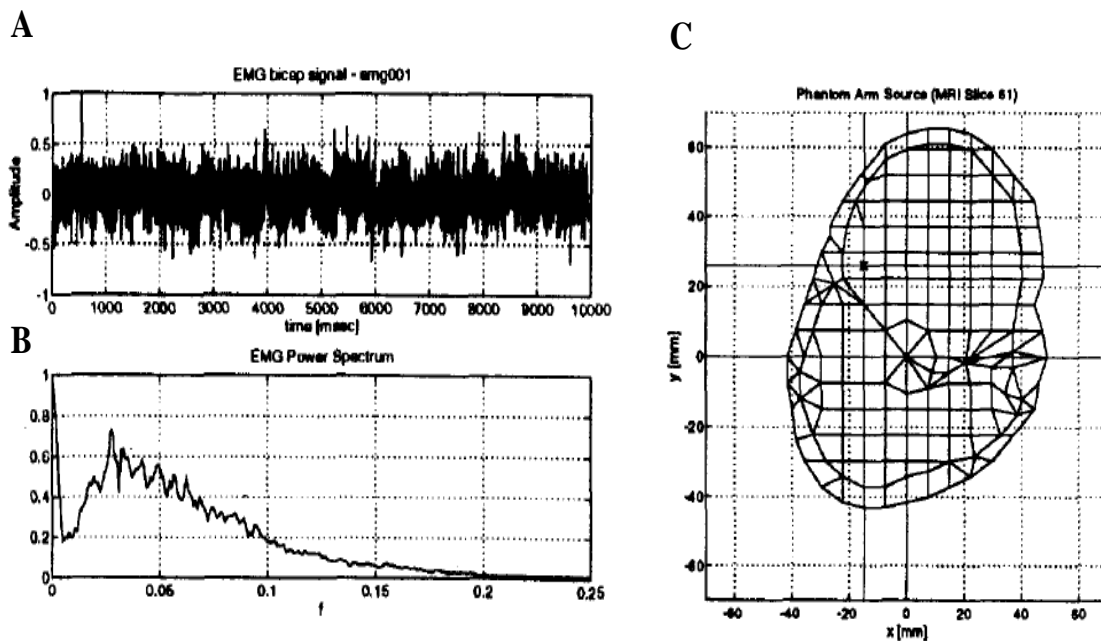
Fig. 2.31 A: Experimental surface EMG signal collected over the BB. B: Power spectrum of the A signal. C: FEM of the upper arm and location of one current source positioned at -15 mm on the X-axis and 25 mm on the Y-axis. This location is within the biceps (adapted from Fig.2 and 6 of [28]).

2.4.2. Under-determined method

In the under-determined approach, the exact number of current sources cannot be fixed a priori. To find the possible locations of the sources, the volume conductor medium is 3D gridded with such a resolution that the numbers of crossing points, each representing a possible source location, are quite large. Unfortunately, a very large number of different dipole positions within the 3D grid, could duplicate the experimental potential distribution. This is called an ill-posed problem and a priori mathematical or physiological information has to be added to provide a realistic solution [38,56].

In a situation where the numbers of sources is much larger than the available measurement points an exact number of dipole sources cannot be fixed a priori. In that context, Van den Doel et al. [56] used MRI to collect realistic information on the shape of the arm, on muscle contours, on fat and skin layers thicknes and bone position (Fig 2.32A). In B, one can sees the model of upper arm muscle MRI in COMSOL software. In C, a cross-section mesh is presented with the position of 12 electrodes from which signals were obtained.

A   B   C

Fig. 2.32 A. Upper arm MRI. B: 3D COMSOL model of the upper arm. C: FEM mesh of a slice of the arm made of tetrahedral elements with 12 electrodes around the arm (from [56], Fig 2).

Results were obtained by solving the Poisson's equation in an anisotropic environment. As a current source, either a tripole (a triangular shape with duration of 2-40 ms) or the Rosenfalk model was used. With a MU innervating hundreds of muscle fibers and a muscle made of 100 to 1000 MUs which are usually not synchronized, 5000 IAP current sources were distributed in the BB and in the brachialis. To reconstruct the current sources, simulations where potentials could be obtained at 215 points on the surface grid or restricted to 56 points in a ring around the center of the muscle where considered, To those signals, a 5% random Gaussian noise was added. Since the 5000 current sources were only placed in the biceps and the brachialis, a large penalty was applied to the triceps region to suppress its activity. The current sources were randomly located either only in the BB or in the brachialis or equally put in both muscles.

2.4.3 Single source localization

To verify the performance of their source location method, a single tripole source was placed at various locations in the three muscles. The results illustrate that when the single source was placed near the humerus bone (deep locations of e to h in Fig 2.33), a noticeable localization error occurs.

$(a)\,D = 1$ $(b)\,D = d^2/dz^2$ $(c)\,D = 1$ $(d)\,D = d^2/dz^2$

$(e)\,D = 1$ $(f)\,D = d^2/dz^2$ $(g)\,D = 1$ $(h)\,D = d^2/dz^2$
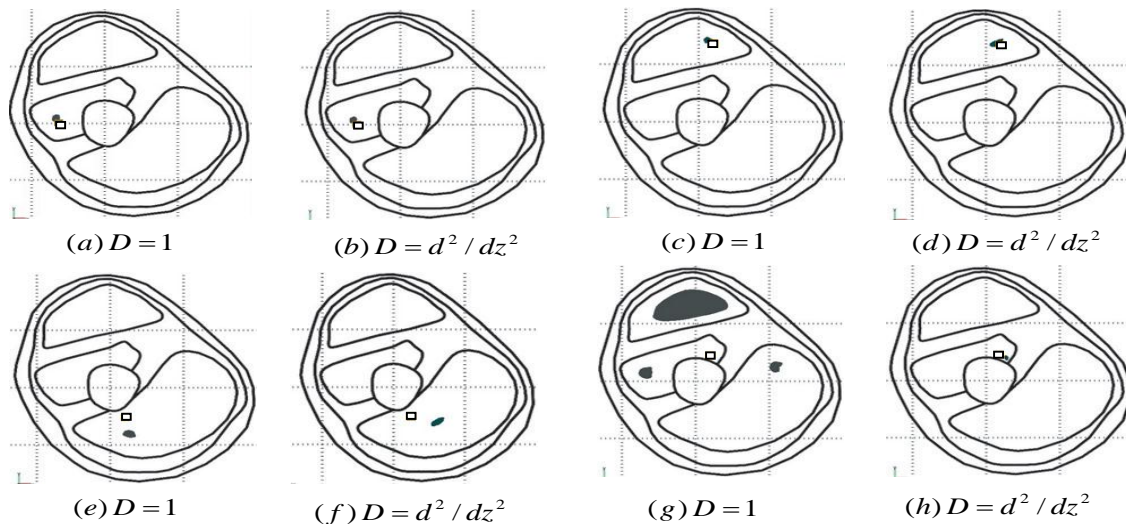
Fig. 2.33 Single tripole source localization under various inverse model variables. Real dipole position is represented by the white squares and the reconstructed positions by the black shape. In (g) 3 reconstructed dipoles were found (adapted from [56], Fig 6).

2.4.4. Discriminating brachialis, BB and triceps

Here, 5 different conditions (Fig 2.34) are considered to activate the 5000 IAPs: all IAPs were placed only in the brachialis (Br), only in the biceps (Bi) and only in the triceps (Tr); then 2500 IAPs where placed in the Br and 2500 in the Bi; finally, IAPs were inserted in equal number in the 3 muscles (All). In Fig 2.34 D=1 indicates that the potential of current sources and *D=d2/dz2* their second derivative are used for the reconstruction. As seen in Fig 2.34, potential (A) provide slightly better results than the second derivative (B) with a grid of 215 points. When only 56 points are used around the limb (panel C), less good results are obtained than in panel A.

A	B	C
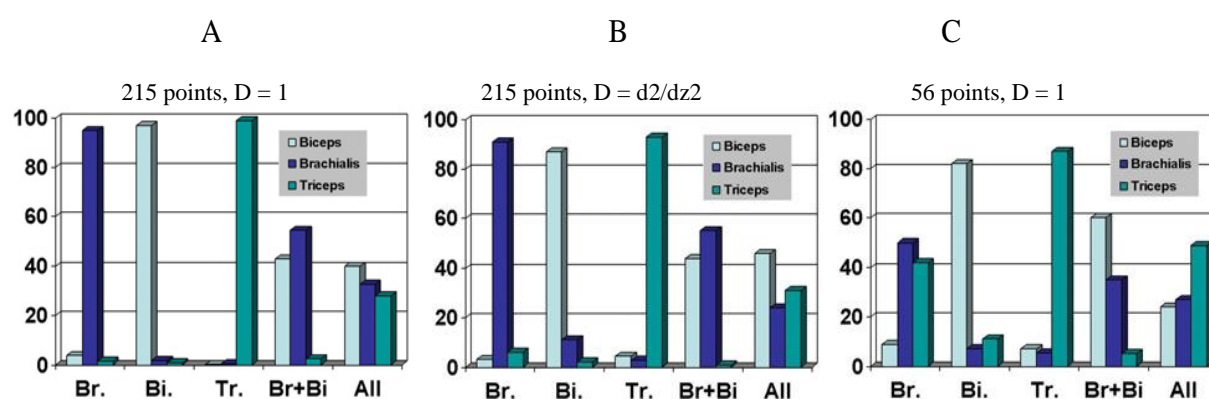
Fig. 2.34 Reconstruction of the current sources for 5 conditions (see above text for a description). A: Results obtained with 215 signal points potentials B: Results with the second derivative of yhe 215 data points. C: Current of sources reconstructed with only 56 points (Adapted from [56], Fig 7).

Besides simulated data, Van den Doel et al. also worked on EMG signals collected around the upper arm with 12 surface electrode pairs from a human subject having his elbow flexed at ~90° flexed with his hand supinated. He produced a isometric flexion of the elbow to activate the biceps and the brachialis only and performed isometric extensions to mainly activate the triceps but possibly also the Bi and Br which provide stabilization of the elbow joint. Without MRI data of the subject a generic arm muscle model scaled to match the arm circumference was used. For the reconstruction, 1s of data was chosen randomly in the middle of each 15s recording. As seen in Fig. 2.35, results in (a) look plausible as the main activity is in the Bi and Br. From the isometric extension in (b) the extension of the Tr is accompanied by a significant amount of co-activation of the Bi and the Br which is also plausible since it is difficult to not activate these muscles for stabilization purposes during the exercise.
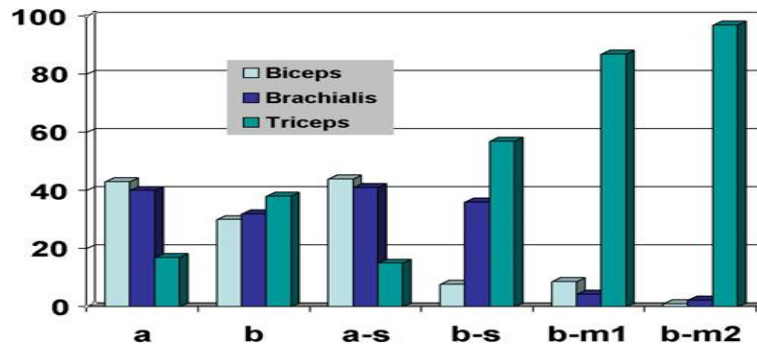
Fig. 2.35 Relative power contribution of the upper arm muscles to total power (100%) **a:** during flexion with main activity in the biceps and brachialis. **b:** during extension with activity in the 3 muscles. **a-s**: synthetic data used for simulating a flexion and result are very close to the real ones in a. **b-s:** synthetic data for extension where activity in the triceps is large but a significant amount of activity in the brachialis and biceps is also present. Less activity in the biceps and brachialis is obtained when only monopolar signals are used either with a ring of 56 sites (**b-m1**) or with 215 sensors (**b-m2**) (from [55], Fig 8).

In another article, van den Doel et al [56] kept using MRI to obtain morphological details (Fig 2.36A). As in an under-determined method, a gridded model was proposed consisting in 4 regions of interest (ROI) as illustrated in Fig 36.B. For *a priori* information, they evaluated many regularization functions: N2, N1 (for 2- and 1-norm), L2 for the Laplacian weighted 2-norm and applied them to a 2D test model. They combined these regularization functions with Tikhonov function to obtain a mathematical inverse model and minimized a cost function with iteration methods like conjugated gradient (CG). Their cost function consists in a least-squares error term (difference between calculated and measured potential) followed by a penalizing function related to the regularization function.

A   B
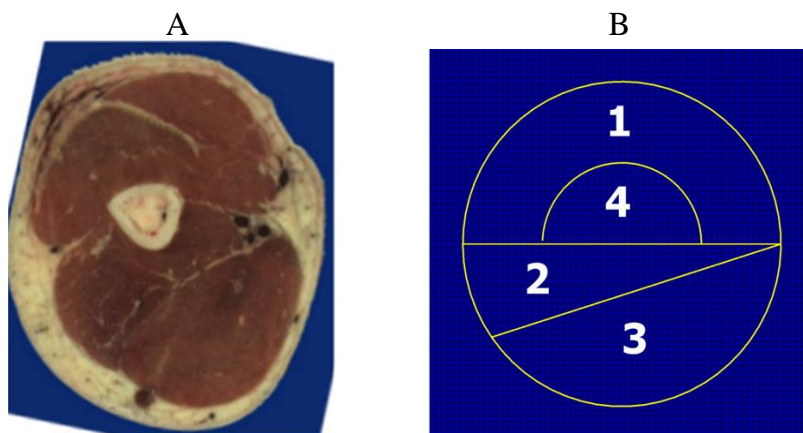
Fig. 2.36 A. Upside down MRI of upper arm muscles. B. Modeling upper arm muscles in 4 areas: 1 and 4: Triceps; 2: Brachialis 3: Biceps (from [56], Fig 2).

To test their inverse model, several current sources where placed inside the triceps and the forward problem was solved in presence of some Gaussian noise. They then reconstructed the location and intensity of the current sources. Out of their tested 10 regularization functions, the L2D function performed better than the others (Fig 2.37). When they experimented with deeper sources with dipoles placed in area 4 (Fig 2.38), L2DW provided a good approximation of the location of the current sources. However L2D gave also good results. So in those two conditions, L2D appears to be a good choice for 3D reconstruction of current sources.
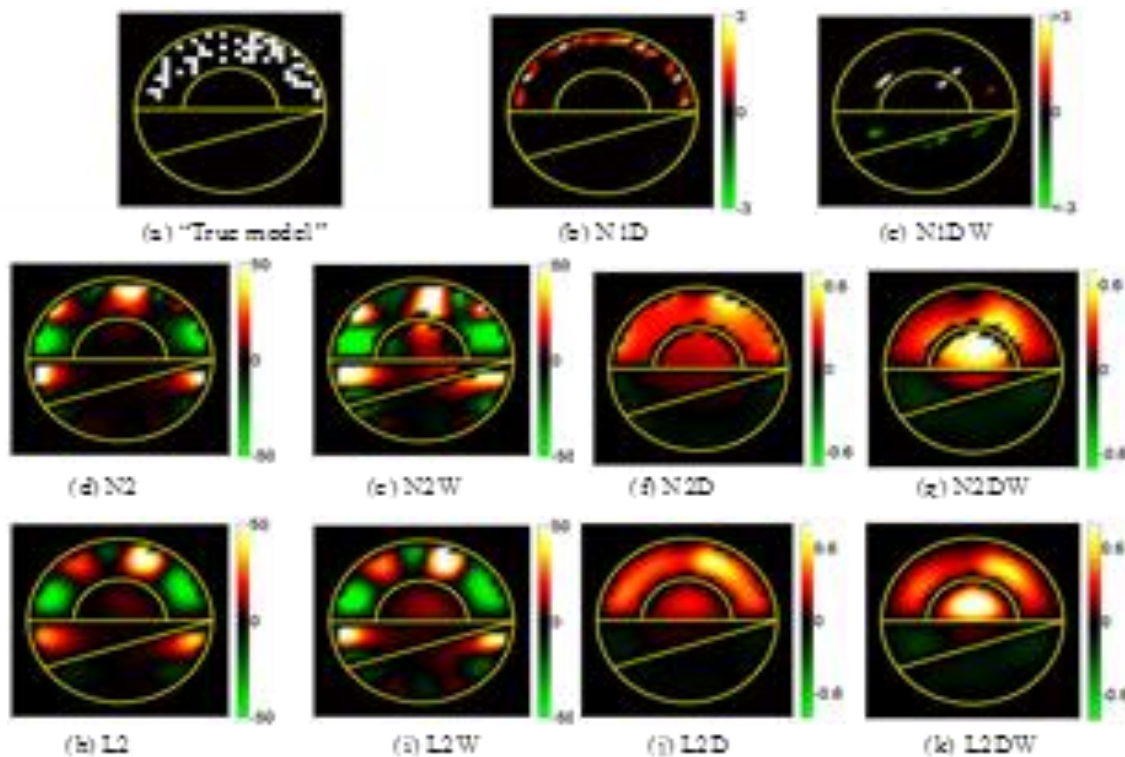
Fig. 2.37 Reconstruction results with different regularization functions when sources are only in region 1. Regularization functions used in this study were Norm functions (N1,N2) and Laplacian (L2) functions with different coefficients W (from [56], Fig 3).

(a) "True model"　　　(b) N1D　　　(c) N1DW

(d) N2　　　(e) N2W　　　(f) N2D　　　(g) N2DW

(h) L2　　　(i) L2W　　　(j) L2D　　　(k) L2DW
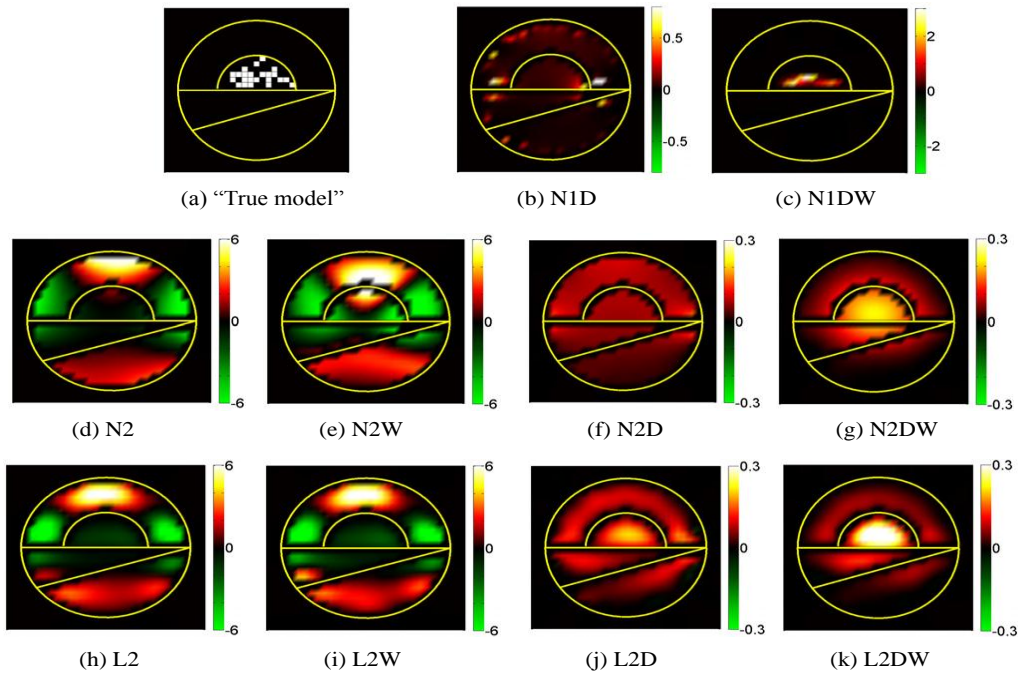
Fig. 2.38 Results with different regularization functions when sources are only in region 4. Same regularization functions as in Fig 2.38.

2.4.5. Results in three dimensions

The forward problem was solved for a 3D model of the arm elaborated from MRI (Fig 2.39). Properties such as stiffness matrix were exported to MATLAB to solve the inverse problem using an iteration method. Results obtained with MATLAB were exported to COMSOL to display the 3D results as in Fig.40. When the L2 and L2D penalty functions were compared when only the biceps or the brachialis was activated (Table 2.5), L2D provided better results.

(a) MRI data　　　(b) 3D geometry constructed
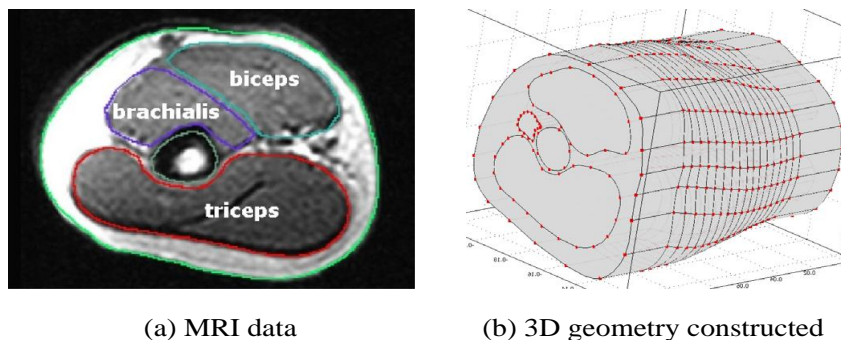
Fig. 2.39 (a). MRI of upper arm. (b) 3D geometry constructed with COMSOL (from [56], Fig 10).

(a) Biceps with D

(b) Biceps no D

(c) Brachialis with D
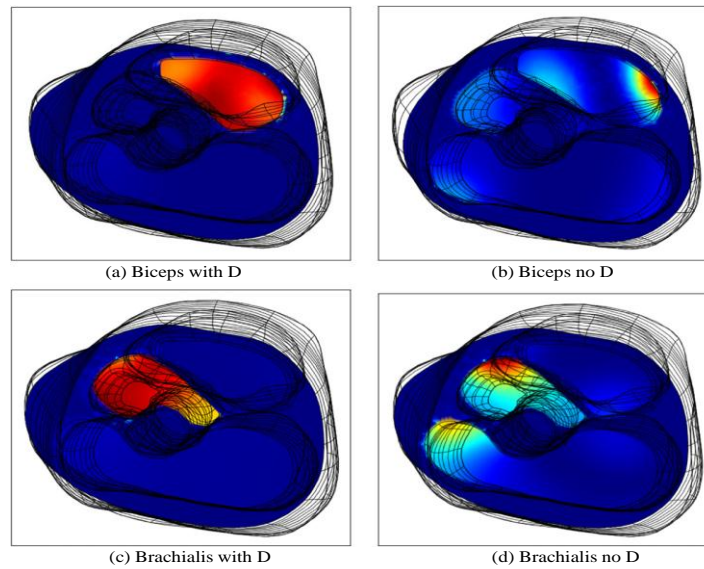
(d) Brachialis no D

Fig. 2.40 Visualization of 3D reconstructed activity with and without D. (a and b):when only the Biceps is active, (c and d): when only the Brachialis is active. Dark blue illustrated the low intensities and red shows the high intensities. Results without D are less descriptive (from [56], Fig 12).

Table 2.5. Normalized activations and their reconstructions in the two different conditions when biceps and brachialis were activate alone in each simulation (from [56], Table 2).

| | Muscle | Normalized activations | | |
		True	L2	L2D
1	Biceps	1	0.73	0.91
	Brachialis	0	0.24	0.05
	Triceps	0	0.03	0.04
2	Biceps	0	0.16	0.02
	Brachialis	1	0.65	0.96
	Triceps	0	0.19	0.02

From the information gathered in this review, we retained the over-determined method for our project. While many muscular fibers are active during a contraction, they can be considered some groups in bundles each one acting as a current source. Our goal being to identify the 6 compartments of the BB with 10 pairs of electrodes positioned over the muscle so the over-determined method is appropriate for our work. In our inverse model, we will use numerical

method to solve this over-determined situation. To find the best location of the current sources with a minimized cost function, the conjugated gradient (CG) nonlinear optimization solutions will be selected because of its fast convergence and stability. Among the several local minimum points obtained with a cost function, we are in search of the most minimum or global minimum point.

To find this global minimum, the optimization method can be initiated with different starting points each giving a local minimum point among which a global one is identified. In another approach, a genetic algorithm (GA) is used where, through mutations of a given population of data, a global minimum can be found. With GA, a fast convergence can be obtained with the addition of nonlinear optimization solutions such as Steepest Descent Method, Conjugate Gradient Method (CGM) and Newton's Method. In our case, we will use the CGM approach because it offers a faster convergence and is more stable than the other methods.

CHAPTER 3: METHODOLOGY

3.1 DIRECT MODEL

3.1.1 Sinusoidal current sources

We initially analyzed data which had been collected few years ago [15]. Those data were obtained with a tank of 8.5 cm of radius. It was circled by 16 equally spaced Ag/AgCl circular electrodes of 5 mm if radius (Fig.3.1A). The tank was filled with a saline solution and 1 to 3 dipoles where placed in it at different positions (Fig.3.1B) but at a fixed height. Illustrated in C the dipoles were made of 2 small pellets of sintered Ag/AgCl and feed with sine waves at frequencies of 22, 32 and 45 Hz and at different amplitude. Recorded signals at the periphery of the tank were amplified (gain of 50), filtered (1-300 Hz) and digitized (2 kHz). The tank size was larger than a human arm but is somewhat in relation with the size of the dipoles which was also larger than a physiological current source.

A　　　　　　　　　　**B**　　　　　　　　　　**C**
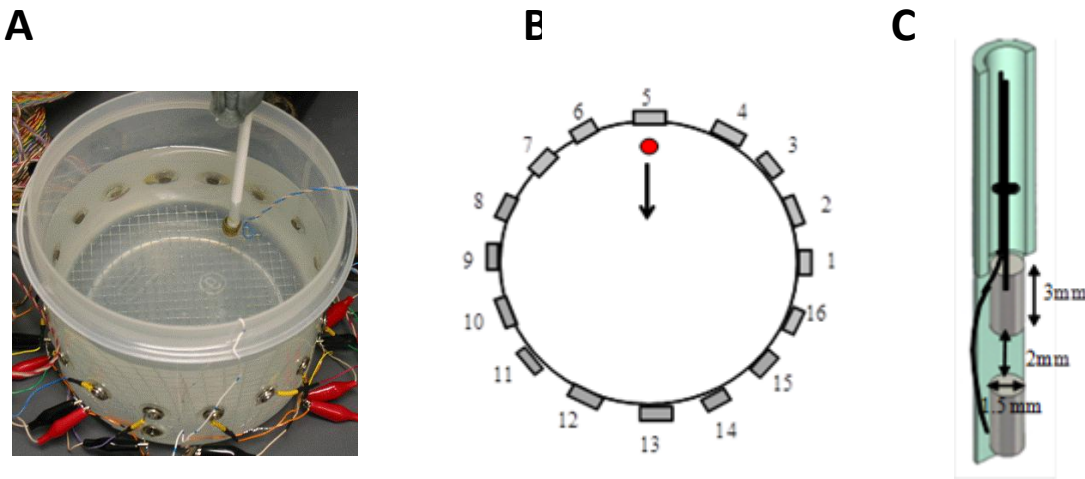
Fig 3.1 A: Photo of the tank circled with 16 equidistant Ag/AgCl electrodes with a dipole near the border. B: top view schematic of the tank. C: Representation of a dipole made of two small sintered Ag/AgCl cylinders.

For this simple cylindrical homogeneous volume conductor, the direct model was elaborated with the Laplacian or Poisson equation where a current density source j in a homogenous medium of conductivity σ produces in the tank an electric potential φ following:

$$\nabla^2 \varphi(r) = -j(r')/\sigma \qquad\qquad\qquad (3\text{-}1)$$

$$\frac{\partial \varphi}{\partial n} = 0 \qquad\qquad\qquad (3\text{-}2)$$

where r and r' are the respective radial position of the detection point and the source and n is the normal component of the current density vector. It vanishes at the tank perimeter since the current cannot flow across the wall of the tank. Moreover, in such an infinite homogenous conducting medium, current source I produces a potential given by:

$$V_\infty = \frac{I}{4\pi\sigma|r-r'|} \qquad\qquad\qquad (3\text{-}3)$$

This is illustrated in Fig 3.2.A where the origin of the axes is placed in the center of the tank and at its bottom.
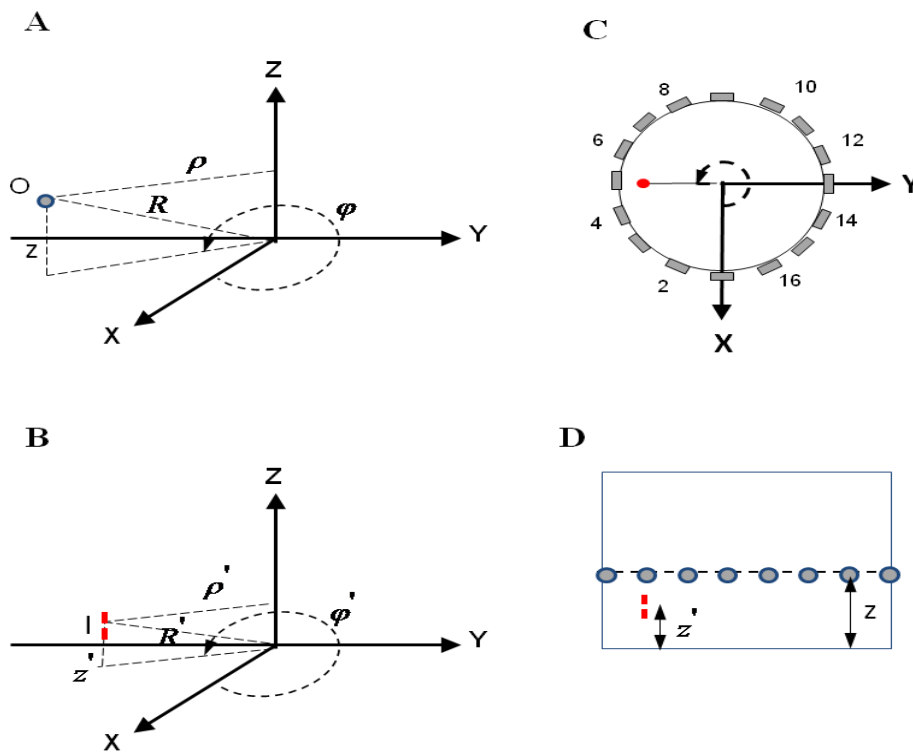
Fig 3.2 **A**: position of an electrode (point O) at the periphery of the tank where R is the electrode distance relative to the center of the coordinates (center of the tank and at its bottom), ρ is the radial distance of the electrode from the z axis, φ is the angle between the X axis and the electrode position in the XY plane and z is the height of the electrode position. **B**: coordinates of the dipole. **C**: top view of the tank with the electrodes and a dipole position. **D**: Side view of the dipole location relative to the recording electrodes.

With a dipole at a given location, the equations of Okada [42] and of Lambin and Troquet [30] have been extensively used to simulate the voltage at each electrode surrounding the tank. To solve equation (3-1), the Green function was used:

$$G(r, r') = \sum_{n \neq 0} \Phi_N \Phi_N^* / \lambda_N \tag{3-4}$$

where Φ_N is normalized solution of the Strum-Liouville problem defined by the eigenvalues of :

$$\nabla^2 \Phi_N + \lambda_N \Phi_N = 0 \tag{3-5}$$

where r is the coordinates of the observation point and r' is coordinates of the dipole.

To obtain the potential around the tank they have to solve:

$$V(r) = (p.\nabla)G(r, r') \tag{3-6}$$

where p is the dipole moment. Due to the finite dimension of the tank, the image phenomenon has to be considered as illustrated in Fig 3.3 where reflections at the bottom of the tank and at the top of the liquid in it give rise to two sets of dipole images located at the points r_j' and r_k'' that r_k'' is the location of dipole image relative to the bottom of the tank, z_0'' and also dipole image relative to the top of the liquid in tank, z_1''. r_j' is the image of z_0'' , z_1'.
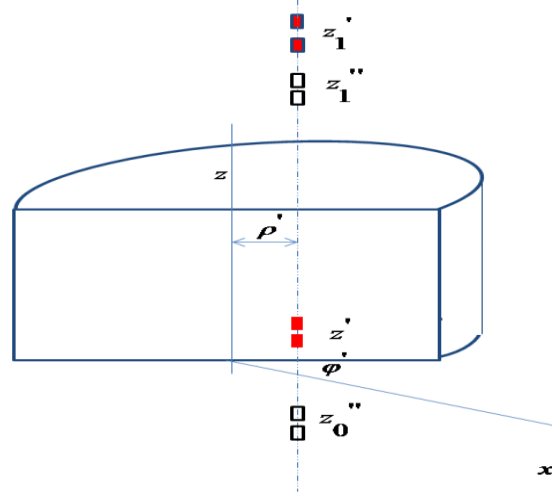
Fig 3.3 The image phenomenon from the front section where the dipole is positioned at $z'(\rho'\varphi'z')$. See following text for further information. Illustration modified from Lambin and Troquet [30].

In the above figure, the dipole is located at z' and its images at z_0'' relative to the bottom of the tank and z_1'' at the top while the image of z_0'' will be at z_1' and these images will be repeated infinitely. The position of a dipole and its image will be according below formulas:

$$\rho'_j = \rho', \quad \phi'_j = \phi', \quad z'_j = 2jL + z' \quad j = \pm 1, \pm 2, \pm 3 \tag{3-7}$$

$$\rho''_k = \rho', \quad \phi''_k = \phi', \quad z''_k = 2kL - z' \quad k = \pm 1, \pm 2, \pm 3 \tag{3-8}$$

Moreover the z component of dipole moment follows below formulas:

$$p'_j = p, \quad p''_k = p - 2p_z n_z \tag{3-9}$$

Solving (3-6) when the dipole is oriented in the z direction as in our situation, they got:

$$V_z(\rho \phi z) = \frac{-p_z}{L^2 \sigma} \sum_{m=0}^{\infty} (2 - \delta_{m0}) \times \cos[m(\phi - \phi')] \sum_{n=1}^{\infty} n I_m\left(\frac{n\pi\rho'}{L}\right) [K_m\left(\frac{n\pi R}{L}\right) - \frac{K'_m\left(\frac{n\pi R}{L}\right)}{I'_m\left(\frac{n\pi R}{L}\right)} I_m\left(\frac{n\pi R}{L}\right)] \cos\left(\frac{n\pi z}{L}\right) \sin\left(\frac{n\pi z'}{L}\right) \tag{3-10}$$

where I_m, K_m is the first and second kind of modified Bessel and δ is delta function and where ϕ' represents the angle between the X axis and the dipole position in the XY plane and the height of the liquid level in the tank is represented by L. Equation 3-10 is used in sections 4.1 (tank data) and 4.3 (EMG signals for subject PM and MM) of the Results chapter.

3.1.2 Extracellular current sources

Sine wave currents were used in our first simulations of the direct problem, but for more realistic results, the current associated to single fibers extracellular potentials (SFAPs) was then used. We thus elaborated an approximation of the signal that would be generated if such a bundle was positioned along the axis of the cylinder used for experiments.

When a muscle is contracted, many individual muscles fibers are activated. From each neuromuscular junction (NMJ), an action potential (AP) propagates in opposite direction up to the tendons. Since NMJ are not perfectly aligned there is some random time activation between the fibers. The generation of an AP is accompanied by an ionic transmembrane current which is

proportional to the first derivative of the AP and is given by: $\frac{\partial \Phi_i}{\partial z} = -r_i I_i$ where Φ_i is the AP, I_i the intracellular current and r_i is resistance per unit length (Ω/cm). Moreover, conservation of current requires that the axial rate of decrease in the intracellular longitudinal current be equal to the transmembrane current per unit length: $\frac{\partial I_i}{\partial z} = -i_m$ where i_m is the current of transmembrane (Fig 3.4) [36].
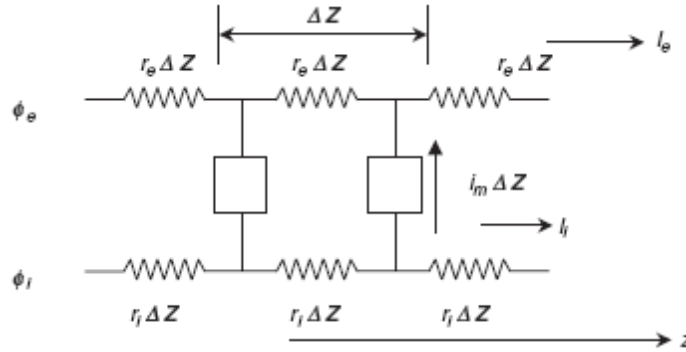
Fig 3.4 Model representing a portion of a fiber membrane shown as a repetitive network of finite length Δz. The rectangular boxes represent the equivalent circuit of the membrane. I$_m$ is the transmembrane current, ϕ_e and ϕ_i are respectively the extra- and intra-cellular potential (from [36], Fig 4.1).

The transmembrane voltage is thus: $\frac{\partial V_m}{\partial z} = \frac{\partial \Phi_i}{\partial z} - \frac{\partial \Phi_e}{\partial z} = -r_i I_i + r_e I_e$, where I_e is the extracellular current. The extracellular longitudinal current may decrease with increasing z either because of a decrement of current that crosses the membrane i_m or a current i_p carried outside by the presence of an indwelling electrode:

$$\frac{\partial I_e}{\partial z} = i_m + i_p$$

Therefore deriving a second time is:

$$\frac{\partial^2 V_m}{\partial z^2} = -r_i \frac{\partial I_i}{\partial z} + r_e \frac{\partial I_e}{\partial z} \Rightarrow \frac{\partial^2 V_m}{\partial z^2} = r_i i_m + r_e(i_m + i_p) = (r_e + r_i)i_m + r_e i_p \qquad (3\text{-}1)$$

the second derivative of the membrane potential being proportional to the transmembrane current, this current is thus used to estimate the potential at the fiber surface.

We used the Miller-Larsson model [39] which is based on the work of Rosenfalck [47]. For an isotropic volume conductor with infinite muscle fiber lengthm this SFAP model $\varphi^{is}(r,z))$ is given by:

$$\varphi^{is}(r,z) = \frac{a^2}{4}\frac{\sigma_i}{\sigma_e}\int_{-\infty}^{+\infty}\frac{d^2V_m}{ds^2}\frac{1}{\sqrt{r^2+(z-s)^2}}ds \qquad (3-2)$$

where V_m is the intracellular action potential propagating along the axis of a muscle fiber and is given by:

$$V_m(s) = \begin{cases} 96s^3e^{-s} - 90 & for\ s \geq 0 \\ -90 & for\ s < 0 \end{cases} \qquad (3-3)$$

where a is the radius of muscle fiber and r ($\geq$ a) is the radial distance from the axis of the fiber (Fig 3.5.A) to P (r, z) where the potential is calculated; s represents the center of the charge distribution associated with the SFAPs.

The potential of a SFAP in an anisotropic medium (φ^{an}) was modeled by Plonsey [45]):

$$\varphi^{an}(r,z) = \varphi^{is}\left(r\sqrt{\frac{\sigma_z}{\sigma_r}},z\right) \times \left[\frac{\sigma_r+\sigma_z}{2\sigma_r}\right] \qquad (3-4)$$

thus eqn 3.4 becomes:

$$\varphi^{an}(r,z) = \frac{\sigma_r+\sigma_z}{2\sigma_r}\frac{a^2}{4}\frac{\sigma_i}{\sigma_e}\int_{-\infty}^{+\infty}\frac{d^2V_m}{ds^2}\frac{1}{\sqrt{\frac{\sigma_z}{\sigma_r}r^2+(z-s)^2}}ds \qquad (3-5-1)$$

where:

$$\frac{dV_m}{ds} = 3\times 96\times s^2e^{-s} - 96s^3e^{-s} \qquad s>0 \qquad \Rightarrow$$

$$\frac{d^2V_m}{ds^2} = 6\times 96\times se^{-s} - 6\times 96s^2e^{-s} + 96s^3e^{-s} = 96s^{-s}s(6-6s+s^2)\ s>0 \quad (3-5-2)$$

with (3-5-2) in (3-5-1):

$$\varphi^{an}(r,z) = \frac{\sigma_r + \sigma_z}{2\sigma_r} \frac{a^2}{4} \frac{\sigma_i}{\sigma_e} 96 \int_{-\infty}^{+\infty} \frac{s(6 - 6s + s^2)e^{-s}}{\sqrt{\frac{\sigma_z}{\sigma_r}r^2 + (z - s)^2}} ds \qquad (3 - 5 - 3)$$

In that equation, Miller Larsson [39] used: $\frac{\sigma_z}{\sigma_r} = 5$ and $\frac{\sigma_i}{\sigma_e} = \frac{1}{3}$ where σ_i and σ_e are the fiber intra-

and extracellular purely resistive conductivity. Within the fiber, the medium is isotropic with a

longitudinal conductivity σ_z while σ_r, the conductivity of the medium outside the fiber which is

perpendicular to the fiber axis, is higher than σ_z. The above equation than becomes:

$$\varphi^{an}(r,z) = 24a^2 \int_0^\infty \frac{s(6-6s+s^2)}{\sqrt{5r^2+(z-S)^2}} \exp(-s)\, ds \qquad (3-6) \text{ [1]}$$

Where φ^{an} represents the spatial potential distribution around a fiber, measured at P(r, z) where

z=vt (Fig 3.5.A). Very close to the surface of a fiber, such a potential with v=5 m/s is illustrated

in Fig 3.5.B.
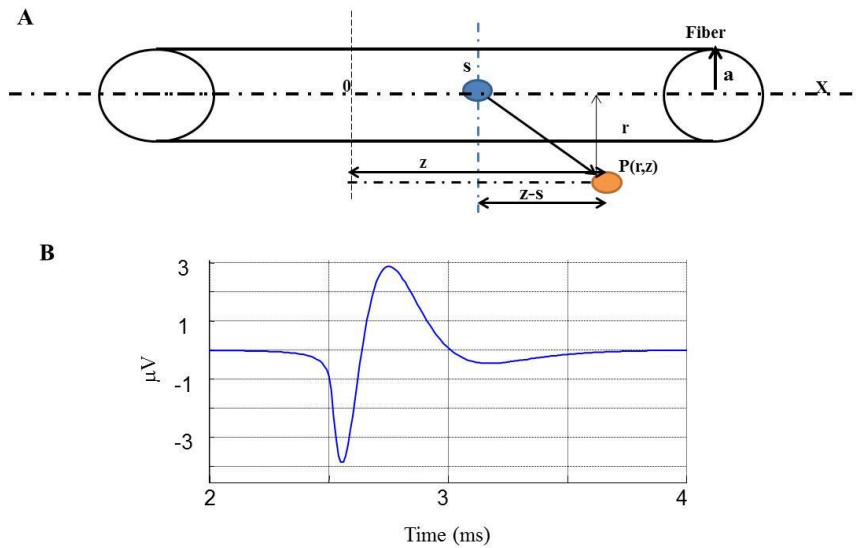
Fig 3.5 A: illustration where s represents a charge distribution on the axis of the fiber and where the fiber radius a is 0.02 mm. The horizontal distance between the charge distribution s and the recording point P is (z-s) and *r* is perpendicular distance. B: extracellular SFAP obtained with r slightly larger than *a*.

---

[1] The second time derivative of equation 3-14 is used to model the current source.

Since the integral along the fiber of membrane current obtained is zero ($\int i_m = 0$), to each $i_m(x)$, we can associated an inverse current $-I_m(x+d)$ at a distance d, which each point can be associated to a dipole that we positioned at the center of the bundle. Assuming that dipoles exist at the center of the bundle the following Okada's equation was used to obtain the potential distribution inside a finite-length cylinder:

$$V_z(\rho\phi z) = \frac{-p_z}{L^2\sigma}\sum_{m=0}^{\infty}(2-\delta_{m0}) \times cos[m(\phi-\phi')]\sum_{n=1}^{\infty}nI_m\left(\frac{n\pi\rho'}{L}\right)[K_m\left(\frac{n\pi R}{L}\right) - \frac{K'_m\left(\frac{n\pi R}{L}\right)}{I'_m\left(\frac{n\pi R}{L}\right)}I_m\left(\frac{n\pi R}{L}\right)]cos\left(\frac{n\pi z}{L}\right)sin\left(\frac{n\pi z'}{L}\right) \quad (3-7)$$

where pz is dipole moment and L represents the height of the tank. Since the integral of the transmembrane current is zero, each point at the fiber surface could be assumed as a dipole obtained by multiplying the current at the fiber surface with a distance (d) between two poles (dipole momentum pz=I.d).

In our simulations, both amplitude and timing of each generated SFAP were randomly chosen from a normal distribution where the amplitude ranged between 0.25 and 10 μV and the timing of their presence varied between 0 and 5 s within a 5 s long simulated signal. A punctual electrode is considered in the previous equations while in practice circular electrodes having 10 mm diameter are often used. To consider that aspect, the following equation [36] was used:

$$H_f = \frac{J_1(\pi df/v)}{\pi df/v}$$

the transfert function of such an electrode is shown in Fig 3.6.
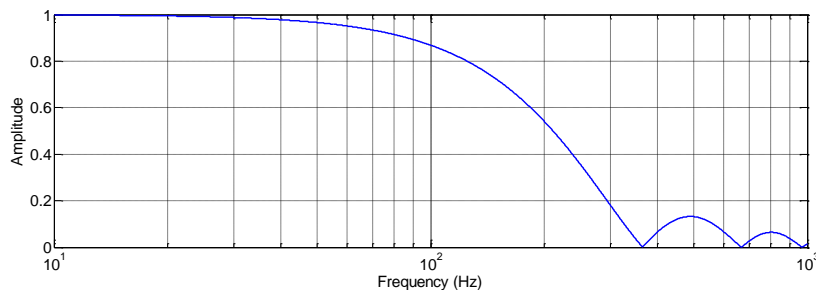
Fig 3.6. Frequency response of a circular electrode (Ø = 10 mm).

3.2 INVERSE MODEL

The strategy considered to solve the inverse problem was simply to use the direct model to generate, for each dipole within a cylinder, a potential at each equidistant electrodes which encircled entirely or partially the cylinder. Amplitude of the signal at each electrode would depend on the intensity of a dipole source and its location within the cylinder relative to each electrode. Since many dipole configurations could reproduce an experimental potential distribution, the most physiologically relevant solution has to be singled out. To make such a sorting, tools such as a genetic algorithm can be used to generate a useful solution.

3.2.1 Genetic Algorithm (GA)

Inverse problem being ill-posed, to find the best solution for the identification of dipoles characteristics, a cost function is mimimized with a search software such as a genetic algorithm (GA), which search through a given space to find through mutations of a given population of data, a global minimum, To GA, a nonlinear optimization solutions such as the Steepest Descent Method, Nonlinear Conjugate Gradient Method (NCG) was added to speed up the convergence toward the global solution.

With the tank data were the dipoles were fed by sinusoidal current of different frequencies, the power spectra of the 16 recorded signals were obtained by the Welch method ([24], p. 418) with the following 2 equations:

$$P^\wedge{}_W\left(e^{j\omega}\right) = \frac{1}{KLU} \sum_{i=0}^{K-1} \left| \sum_{n=0}^{L-1} \omega(n) x(n + iD) e^{-jn\omega} \right|^2 \tag{3-16}$$

where in each segment, L is the length of each segment, D is the number of segment (L and D is a series of values which obtained from the digitalization the signals in time tomain). Moreover, K is the value of overlap in each sequence and U is normalization constant present in the definition of the modified periodogram. Therefore, the expected value of Welch's estimate is given by:

$$E\{P^\wedge{}_W\left(e^{j\omega}\right)\} = \frac{1}{2\pi LU} P_x\left(e^{j\omega}\right) * \left| W\left(e^{j\omega}\right) \right|^2 \tag{3-17}$$

from which only the peak value was used as an a priori information in the inverse model. The least square method between the simulated and the experimental data was used to get a global minimum among the many possible local minima. A generic flow chart of the GA algorithm is presented in Fig 3.7 and our cost function to be minimized is:

$$min\|J\| = \sum_{i=1}^{16}(Welch\left(V_z(\rho',\varphi',z')\right) - Welch(V_{i,observation}))^2 \qquad (3\text{-}18)$$

where V_z is the inverse model potential obtained from a given position of the dipole(s) for each of the 16 recording electrodes and V_i is each experimental signal
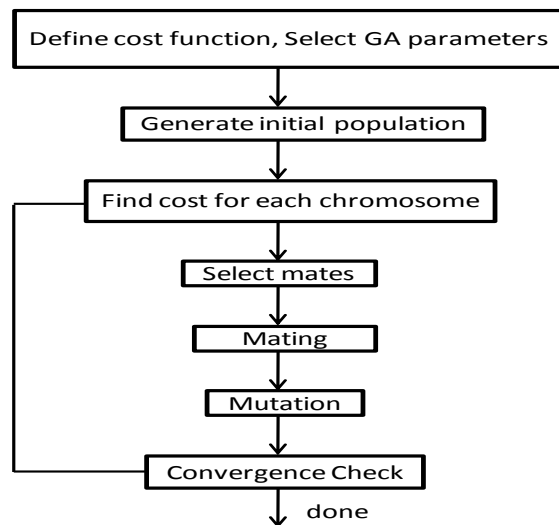
Fig. 3.7 Flowchart of a GA and nonlinear optimization.

With the cost function determined the GA is started by defining the population size. If it is too small, not all the solutions within the search space will be explored leading to inconsistent results but when it is too large, the convergence of the algorithm will be time consuming. With the tank data, 20 chromosomes were used each representing a plausible dipole location within the tank (ρ its radial position, φ its angular position and I a relative intensity). To code those 3 parameters, a 20 bits string was used: the first 7 bits represent the radial distance (ρ) at a step of 0.66 mm to cover the tank radius from 0 to 85 mm, the next 9 bits encoded its angle (φ) with a resolution of 0.70° and the final 4 bits indicate its relative intensity in 16 steps covering 0 to 10. In Table 3.1, a

sample of the initial 20 chromosomes as obtained with the Matlab rand function is presented. When two or three dipoles are simulatenously present in the tank, the search domain is greatly enlarged since many more combinations have to be evaluated to get a best fit. The size of a chromosome was then doubled or tripled.

Table 3.1 Initial 20 chromosomes: associated to a dipole characteristics

no	Binary coding	Radial	Angle	Intensity
1	0100011 010010001 0111	3.5	145	7
2	0110011 000101100 0110	5.1	44	6
3	1000000 001100001 0101	6.4	97	5
4	0110010 001011101 0010	5	93	2
5	0101111 001110111 1000	4.7	119	8
6	0110010 000110111 0010	5	55	2
7	0101100 001111101 0011	4.4	125	3
8	0000111 000101100 1001	7	44	9
9	0111101 100111110 1000	6.1	318	8
10	1010101 000100010 0100	8	34	4
11	0011110 101001111 0011	3	335	3
12	1010011 010010000 0110	7.8	144	6
13	0011101 000010001 1001	2.9	17	9
14	1001011 001111011 1001	7.5	123	9
15	0100111 100001001 0110	3.9	265	6
16	0100011 100011110 0011	3.5	286	3
17	0010011 011000100 1000	1.9	196	8
18	0001011 011110111 0100	1.1	247	4
19	0011010 101000010 1001	2.6	322	9
20	0111110 000010100 0001	6.2	20	1

As each chromosome encode the position and intensity of a dipole, equation 10 of section 3 is used to calculate the potential that a dipole can generates at each of the 16 electrodes placed around the tank Having done that with the initial 20 chromosomes, a cost function defined as:

$$\cos t_k = \sqrt{\sum_i^n (Dipole(i) - data(i))^2} \qquad (3.19)$$

where k=1 to 20 (chromosomes) and i=1 to 16 (number of electrodes). The 10 chromsomes for which $\cos t_k$ are the smallest are chosen to become parents and have offsprings in order to create a new generation. To produce offsprings, *mating* is done by the cross-over operation where, for each parents, different start and end bits are chosen and exchanged between them. For example, let's take the two following chromosomes where the 5nd up to the 13th bits of each chromosome (shown within rectangles) is inherited to the other chromosome in order to produce 2 offsprings:

0101 111 001110 111 1000 → 0101010 000110 111 1000

0110 010 000110 111 0010 → 0110111 001110 111 0010
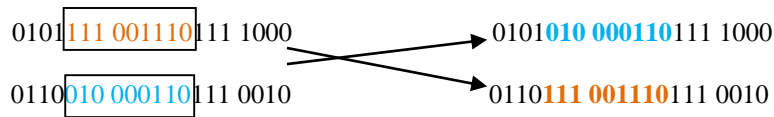
As shown at the right of Table 3.2, the start and end bits for the crossover are randomly chosen as illustrated for the first 8 chromosomes of Table 3.1.

Table.3.2 Sample of 10 parents and their offsprings

No	Parents	Mate	Bit Start	Bit End	Offsprings (new generation)
1	0110011 000101100 0110	6	5	11	0110110 000001100 0110
2	0110010 000110111 0010	7	13	19	0110010 000111101 0010
3	0000111 000101100 1001	8	10	18	0000111 001100001 0101
4	1010101 000100010 0100	9	4	12	1011110 101000010 0100
5	0011101 000010001 1001	10	13	20	0011101 000010111 1000
6	0111110 000010100 0001	1	5	11	0111011 000110100 0001
7	0110010 001011101 0010	2	13	19	0110010 001011101 1000
8	1000000 001100001 0101	3	10	18	1000000 000101100 1001
9	0011110 101001111 0011	4	4	12	0010101 000101111 0011
10	0101111 001110111 1000	5	15	24	0101111 001110001 1001

When a minimum distance between real data and those obtained with the GA, is found and some bits coding either the radius, angle or the relative intensities do not change during successive generations (in Table 3.2, 9th bit which shows the angle has this property), this point may only be

a local minimum. To find a global one, a Mutation operation consisting in some logical operations such as "and" between the chromosomes or "inverse" of one or two bits of some chromosomes is done. If the new minimum point converged to the previous one, than a global minimum is considered to have been detected; otherwise a new minimum point is obtained and the mutation process is repeated. Such cycles are repeated up to the time that the difference between the results obtained with the GA and the real data are within a choosen value. The algorithm is then stopped and the last results obtained are expected to be the best ones.

As long the initial conditions are properly determined, GA is a robust and reliable method to minimize the difference between the inverse model data and the experimental ones otherwise the convergence toward a solution can be very slow naking the process non-effective. This can be prevented by putting restrictions on the initial population. So, for restricting the search of the dipoles angular positions around the tank, the root mean absolute value (MAV) or root mean square (RMS) values of each of the 16 EMG signal was calculated. As a dipole produces a larger potential when near an electrode than away from it, the position of the highest MAV or RMS values indicated the best angles to initiate the search.

3.2.2 Nonlinear Conjugated Gradient (NCG)

When numerous parameters have to be optimized, the speed of convergence to a global minimum point could be very slow. To prevent this, after the first GA global minimum, the Nonlinear Conjugated Gradient (NCG) [59] was used to complete the search of a better minimum for the position (ρ, φ) and relative intensity of each considered dipole. The initial parameters of the NCG algorithm where those obtained at the end of the GA iterations:

1) x is a vector encoding the radial distance, angle and relative intensity of each dipole in the tank. So for 2 dipoles, x_j will encode 6 values: the first two for the radial distance of each dipole, the next two for their angles and the last two for their relative intensities.

2) $I(x)$ the last GA cost function value

so the initial values used in NCG are: $x_0 = x$ and $I(x_0) = \nabla I(x)$ since the NCG and GA cost functions are the same because the goal is minimization of the different berween the simulation and experimental data and just the methods are different. The initial direction of the steepest descent (gradient) around x_0 is then given by:

$$g_0 = \quad I(x_0) \tag{3.20}$$

and: $$x_1 = x_0 + ap_0 \tag{3.21}$$

where a is the learning rate (or step length) used to upgrade to a new point and p_0 the initial search direction which is equal to $-g_0$ giving:

$$x_1 = x_0 - ag_0, \tag{3.22}$$

After this iteration, other gradient directions p_j for finding the new points are obtained with:

$$p_j = -g_j + b_j p_{j-1} \tag{3.23}$$

where b_j is a learning rate or step associated to the direction vector p_{j-1} and obtained with:

$$b_j = \frac{g'_j g_j}{g'_{j-1} g_{j-1}} \tag{3.24}$$

which gives: $$p_j = -g_j + b_j p_{j-1} \tag{3.25}$$

Having the gradient direction, the search point is upgrated from this direction:

$$x_{j+1} = x_j + ap_j \tag{3.26}$$

A generic flowchat of the NCG is presented in Fig. 3.8.
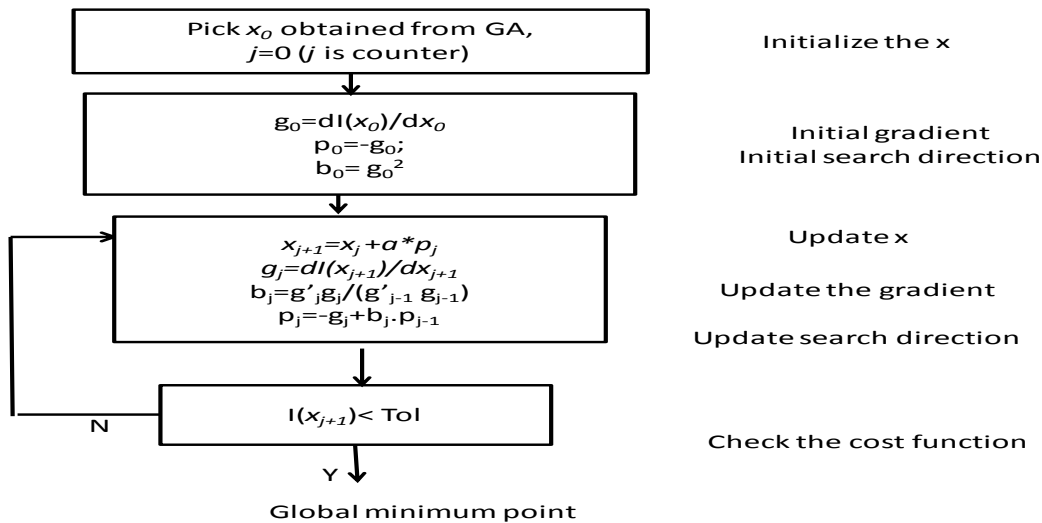
Fig 3.8 Flowchart of the nonlinear conjugate gradient (NCG) optimization process where a and b are two learning rate constants updated at each iteration (Tol=10^{-12}).

CHAPTER 4: Results

4.1 Tank data

To initially test our inverse program, we started analyzing the very simple situation where a dipole was moved from close to the tank border up to its center (Fig 4.1).

A   **B**
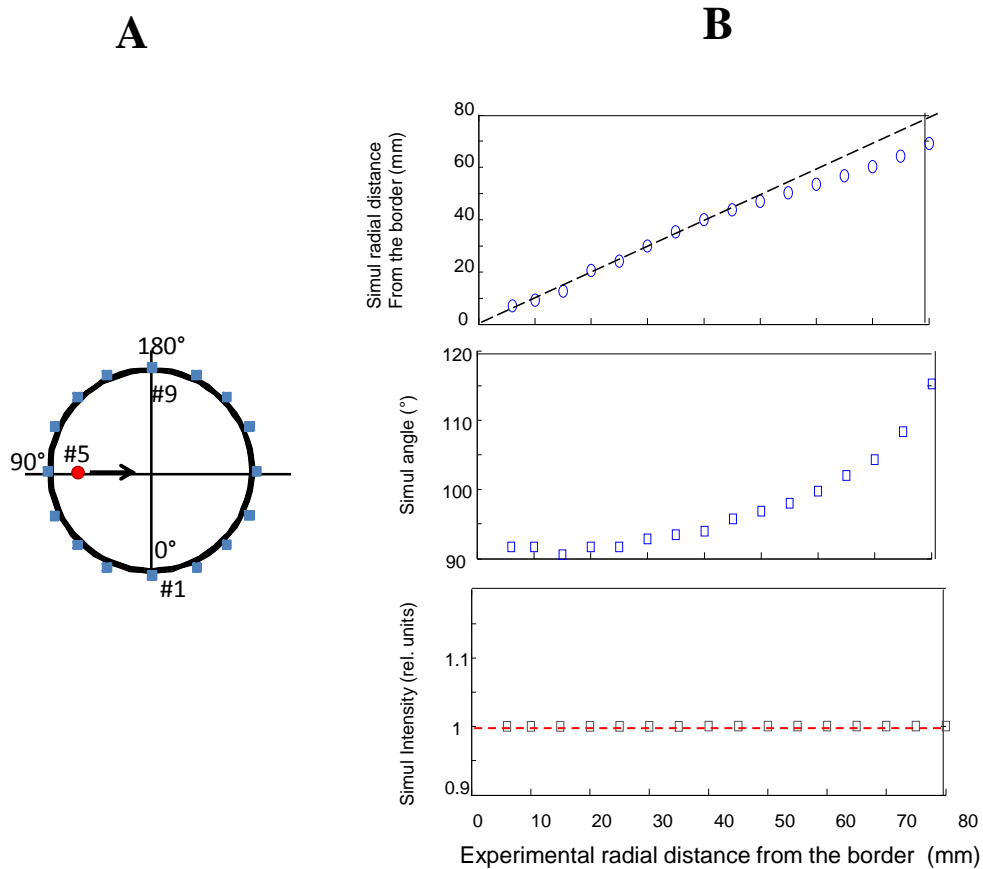
Fig 4.1 A. Top view of the tank with one dipole placed in front and at 5 mm from electrode #5 before being moved radially toward the tank center. B. Inverse model results as the dipole was moved toward the center.

As the dipole is getting closer to the tank's center, the detected position is smaller than the one expected. Part of that error arises for the angular position of the dipole which as seen in the Simul. Angle panel is varied from 90° to more than 110°. Such a deviation from the planned trajectory is also detected in Fig. 4.2A where signal at electrode #6 is higher than at #5 when the dipole was at 80 mm for the border of the tank. As illustrated in Fig.4.2B, the detected position of

the dipole by the inverse model is larger than expected from the tank center which leads to underestimated positions in Fig 4.1B for the values between 50 and 80 mm from the tank border.

A

B
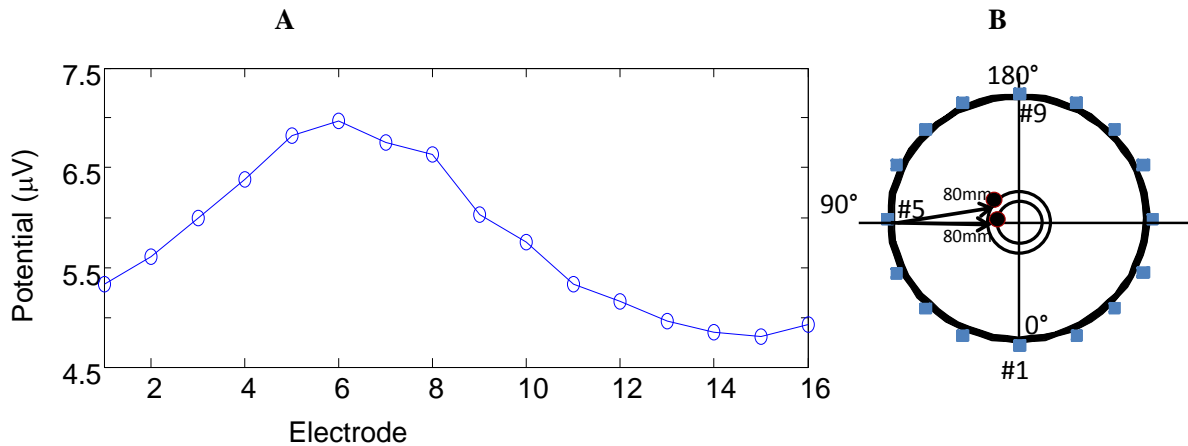
Fig 4.2. A. RMS values collected under each electrode when the dipole was at 80 mm from the tank's border. Maximum value is under electrode #6 while is should have been under electrode #5. B. due to the angular misalignment, the dipole distance from the center is greater than expected.

So to verify those results, we solved the direct model by simulating the same situation i.e. a dipole at a given location and with an intensity of 1 in a tank. In absence of any measurement and experimental errors, the inverse model results produce good results (Fig 4.3).

Forward			Inverse			Error (%)		
R(cm)	Phi(°)	I	R(cm)	Phi(°)	I	R%	Phi%	I(%)
7.5	90	1	7.5	90	1	N.S	N.S	N.S
7	90	1	7	90	1	N.S	N.S	N.S
5.5	90	1	5.5	90	1	N.S	N.S	N.S
4	90	1	4	90	1	N.S	N.S	N.S
2	90	1	2	90	1	N.S	N.S	N.S
0.5	90	1	0.5	90	1	N.S	N.S	N.S
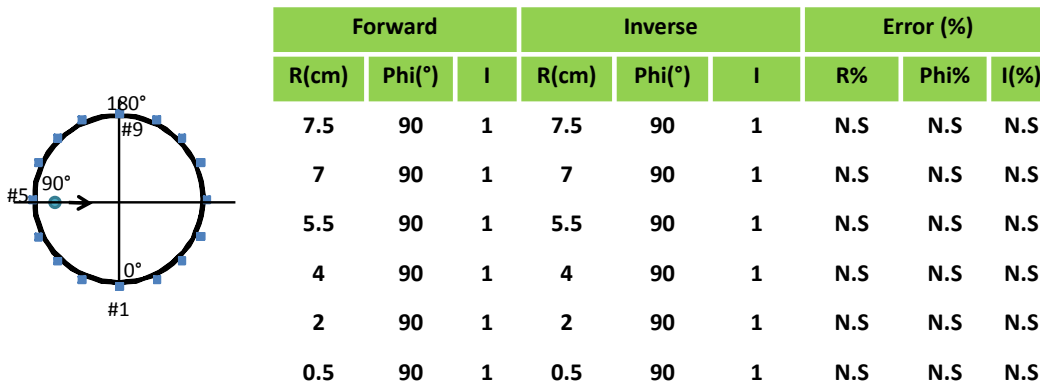
Fig 4.3. Simulation results obtained with the direct and inverse models when a single dipole is moved toward the tank's center (N.S= non significant).

Initially, in experiments with 2 dipoles, one was kept at a fixed position while the other dipole was moved toward the tank's centre. As with one dipole, as the dipole is approaching the centre of the tank, its angular position moved away from the intended path which reduced the detected radial distance from the border (Fig.4.4). While a constant intensity value was found for the fixed dipole, a different situation was observed for the moving one. This can be due to deviation of angle and its effect on radial distance therefore to obtain the minimum cost function, the lower intensity was obtained.
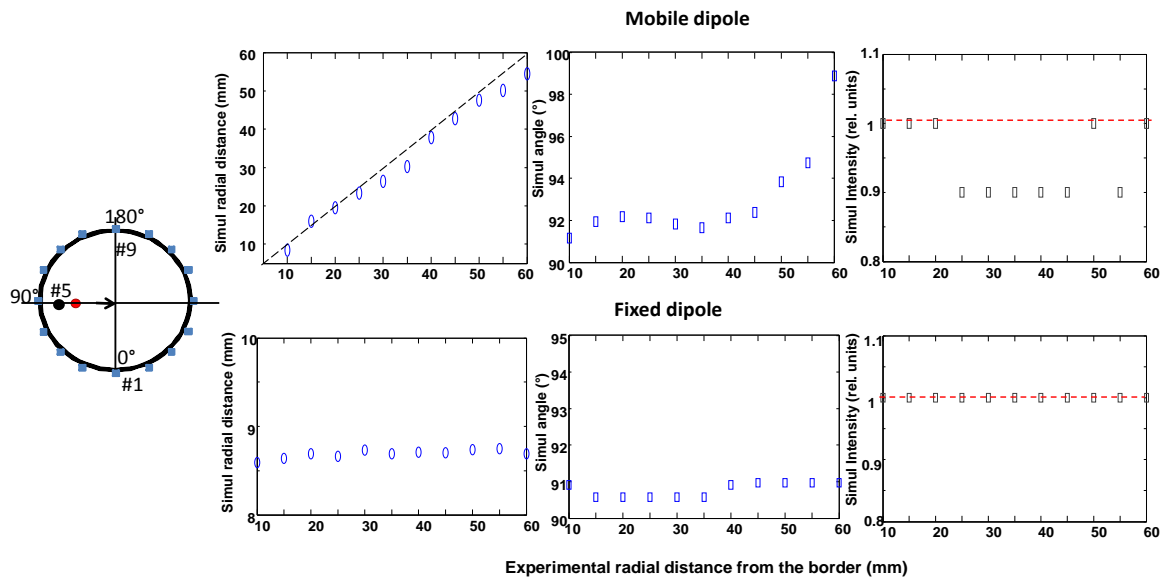
Fig 4.4. Inverse model results when a dipole is moved toward the center while another one is fixed at 10 mm from the border from Filion directory multiple_sensibilite_radiale).

In a second test, the fixed dipole remain at 10 mm in front of electrode #5 while the other one at 10 mm for the border is angularly moved from close to electrode #5 to electrode #10 in 11.25° steps. With the inverse model it can be seen (Fig.4.5) that the detected angular position of the mobile dipole correlates very well with the expected angular position. Again, detected intensity value of the fixed dipole is more stable than foe the mobile one. Changes in the dipoles distance from the tank border can be linked to manipulations errors.   The first condition considered with 3 dipoles consists in moving radially toward the center a dipole initially placed in front of electrode #9 at 10 mm from the border. As for the other 2 dipoles, they where kept fixed position in front of elecrodes #4 and #14 at 10 mm from the border. As can be seen in Fig 4.6, radial distance error for the mobile dipole also increased as it got closer to the center due, here to a decrease in its
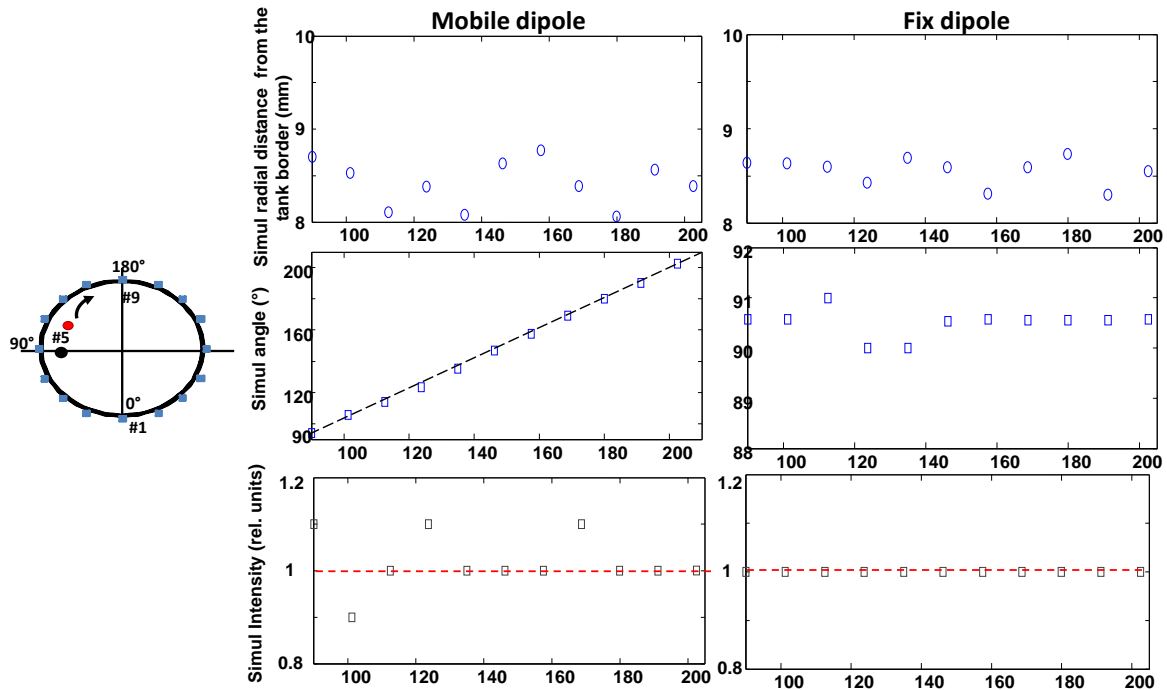
Fig 4.5. Result of the inverse problem when a dipole is moved angularly with the second one is kept in front of electrode #5 (from Filion directory multiple_sensibilite_angulaire).
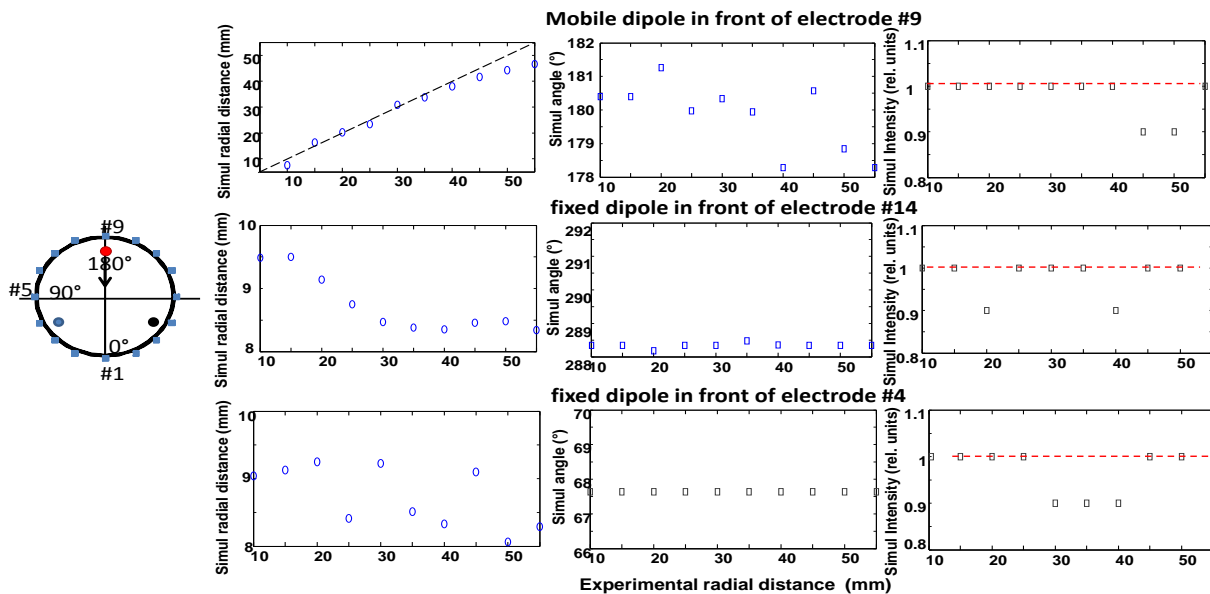
Fig 4.6. Results of the inverse problem when 2 dipoles are at a fixed position and the third one moved radially in steps of 5 mm toward the center of the tank. Same current intensity feeding each dipole (from Filion 3_dipoles_exp_E directory).

angular position, which produced the same effect as an increase as found with one moving dipole. Here errors in the intensity values were found even for the 2 fixed dipoles. A good similitude was

observed between the experimental potential distribution around the tank and the inverse model results as shown in Fig.4.7 for 2 positions of the mobile dipole.

A								
ρ_1	φ_1	I_1	ρ_2	φ_2	I_2	ρ_3	φ_3	I_3
8.34	67.6	1	8.55	180.4	0.9	8.49	288.2	1

B								
ρ_1	φ_1	I_1	ρ_2	φ_2	I_2	ρ_3	φ_3	I_3
8.41	67.6	0.9	23.44	179.9	1	8.75	288.3	1
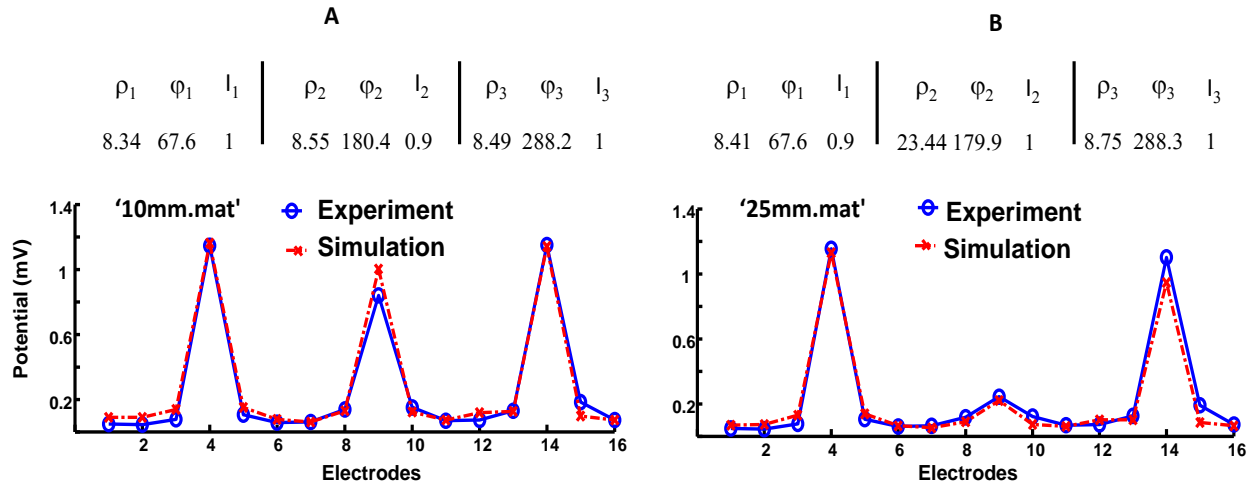
Fig 4.7 From the same dataset of the previous figure, comparison between experimental RMS values and inverse model results for the 10 and 25 mm position of the mobile dipole.

In the second tested situation, 2 dipoles where kept fixed in front of electrodes #9 and 10 while the mobile dipole were moved from electrode #13 to between electrode #10 and #11. The intensity of the mobile dipole was 2 while it was 1 for the two fixed dipoles. In Fig 4.8, it can be seen that result is illustrated and it can be seen that the movement of angle is detected very good by our inverse model.

In the last condition, the 3 dipoles are all in a fixed positions in front of electrodes #4, #9 and #14 while the intensity of the current feeding one dipole is varied between 0.5 to 2. As can be seen in Fig 4.9, results are satisfying for the estimated radial distance and angular position but less good for the intensity evaluation of the mobile dipole.
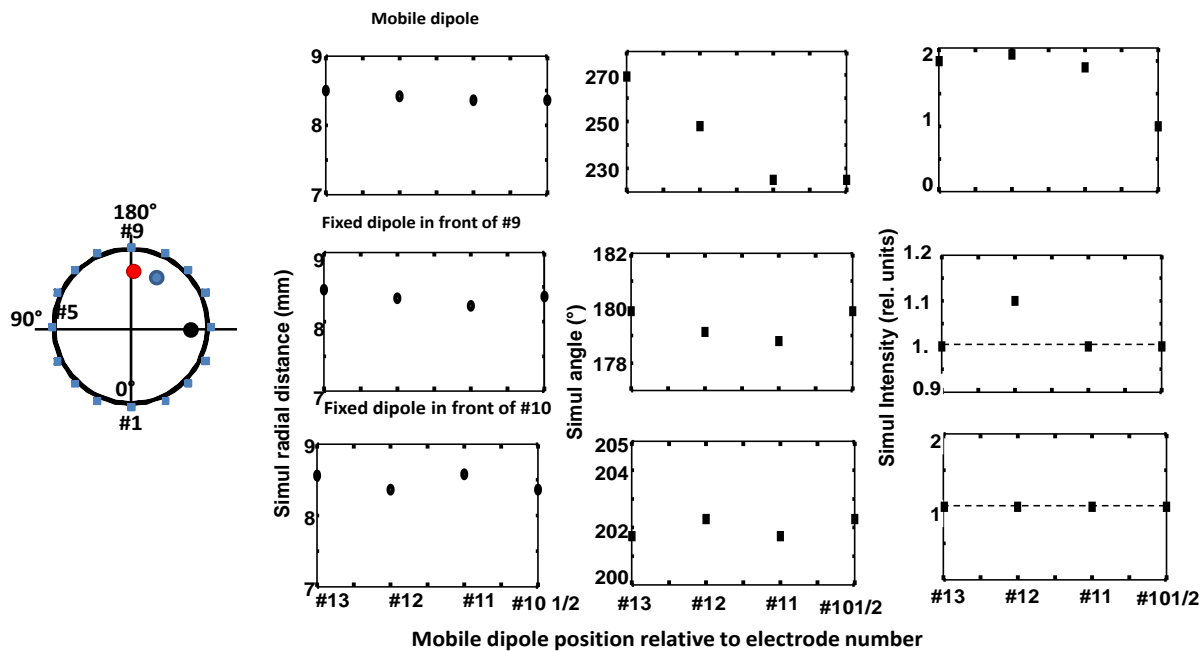
Fig 4.8 Results of the inverse problem when a dipole has angular movement and two others remained fixed close to electrode #9 and #10 (from Filion 3_dipoles_exp_B directory).
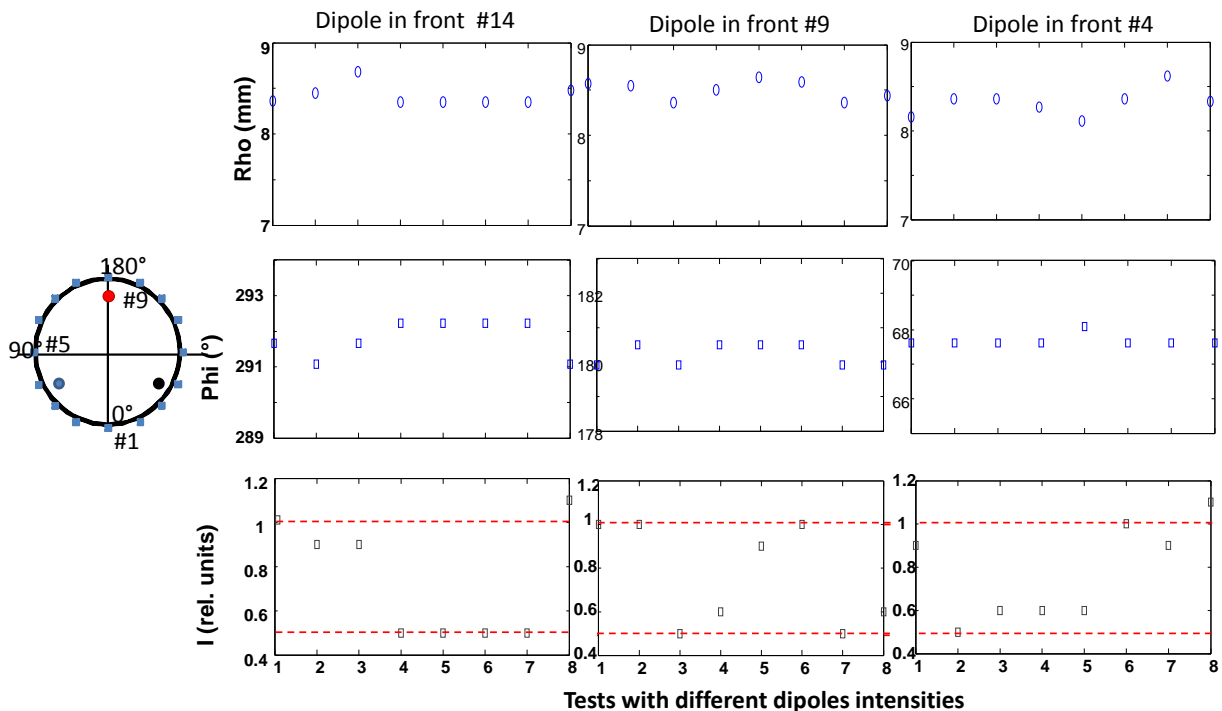
Fig 4.9. Results of the inverse model when 3 dipoles are in fixed position but their relative intensity is for position 1: **1:1:1**. for 2: **½:1:1**. for 3: **½:½:1**, for 4: **½:½:½**, for 5: **¼:1:½,** for 6: **1:1:½,** for 7: **1:½:½** and for 8:**1:½:1** (from Filion 3_dipoles_exp_D directory).

To evaluate the robustness of the inverse model, to each sinusoidal signals for which results are displayed in Fig. 4.6, white Gaussian noise was added, with a S/N ratio of 30, 20 and 10 dB (Fig. 4.10).
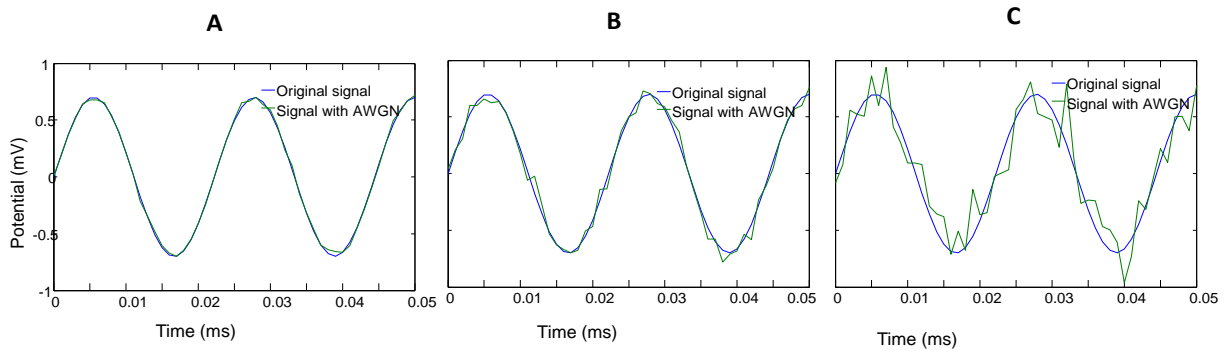
Fig 4.10 Sinusoidal signal (45 Hz) to which different S/N white noise ratio was added. A: 30 dB; B: 20 dB; C: 10 dB.

Table 4.1: Effect of the addition of 3 different white gaussioan noise levels on the characteristics when the mobile dipole was moved from 10 to 70 mm toward the center of the tank. Values in red indicate negative differences i.e. smaller than expected results.

position: 10 mm	rho (mm)	phi (°)	I (rel.)
inverse results	8,55	180,4	0,9
no noise diff (%)	14,50	0,22	10,00
30 dB diff (%)	14,80	0,28	10,00
20 dB diff (%)	15,10	0,28	10,00
10 dB diff (%)	15,20	0,28	10,00

position: 30 mm	rho	phi	i
inverse results	30,83	180,4	1
no noise diff (%)	2,77	0,22	0,00
30 dB diff (%)	5,07	0,06	0,00
20 dB diff (%)	5,40	0,22	0,00
10 dB diff (%)	5,60	0,06	0,00

position: 50 mm	rho	phi	i
inverse results	48,02	178,8	0,9
no noise diff (%)	3,96	0,67	10,00
30 dB diff (%)	4,22	0,72	10,00
20 dB diff (%)	5,56	0,67	10,00
10 dB diff (%)	13,46	0,67	10,00

position: 70 mm	rho	phi	i
inverse results	63,06	172,70	1,00
no noise diff (%)	9,91	4,06	0,00
30 dB diff (%)	10,29	4,50	0,00
20 dB diff (%)	10,79	4,50	0,00
10 dB diff (%)	19,44	4,83	0,00

The effect of noise addition is only illustrated here for the mobile dipole[2]. As can be seen in Table 4.1, the presence of added noise did not perturb the prevailing situation when the mobile dipole was at 10 mm from the tank border. As the mobile dipole got closer to the tank center, the error in the dipole position as well as in its angular position is more related to the increasing distance from the recording electrodes than to the presence of the noise, the effect of which is only clearly visible with a 10 dB S/N ratio.

To verify the angle position of the moving dipole, a power spectrum analysis was performed on the signals to which noise has been added. With the power spectrum, it was detected that the 3 dipoles were feed with sinusoidal current at 22.5, 32 and 45 Hz. Information on the amplitude and phase of those signals at each electrode were inserted in the inverse model. To demonstrate the deviation angle of the moving dipole from its planed trajectory in the experimental data, amplitude of the 32 Hz sinusoid (the mobile dipole signal frequency) was measured at each recording electrode when the dipole was at different positions. Fig.4.11A show the results when the dipole was at 70 mm from the border and in Fig.4.11B when at 10 mm from the border.In this latter case, the maximum amplitude of the spectrum component at 32 Hz is in front of electrode #9 as expected. As the dipole reached 70 mm (near the center of the tank), amplitude is higher under electrode #8 indicating a progressive shift in the dipole angular position from its planned trajectory.
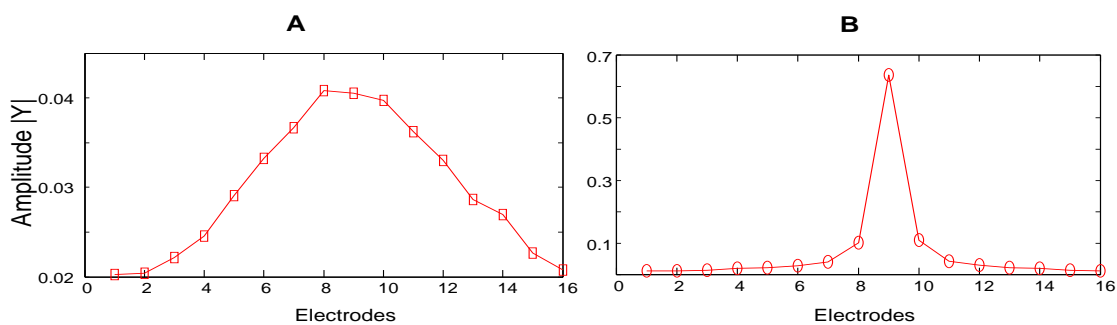
Fig 4.11. Amplitude of the spectra. In A, the dipole is at 70 mm and in B at 10 mm from the tank border

---

[2] Additional results are presented in Annex 2.

4.2 Simulated EMG signals.

To further test the appropriatness of our direct and inverse model, instead of analyzing dipoles feeded with sinusoidal current, extracellular action potentials (SFAPs) associated to the activity of a pool of motoneurons where simulated to generate dipole current. The SFAP model of Miller-Larsson [39], which is an enhanced version of the Rosenfalck [47] model for an isotropic volume conductor, was used. The Rosenfalk model is given by:

$$\varphi^{is}(r,z) = \frac{a^2}{4}\frac{\sigma_i}{\sigma_e}\int_{-\infty}^{+\infty}\frac{d^2V_m}{ds^2}\frac{1}{\sqrt{r^2+(z-s)^2}}ds \qquad (4-1)$$

where σ_i and σ_e are the intra and extra cellular conductivities, respectively. Moreover V_m is the intracellular action potential propagating inside and along a muscle fiber is described by:

$$V_m(s) = \begin{cases} 96s^3e^{-s} - 90 & for\ s \geq 0 \\ -90 & for\ s < 0 \end{cases} \qquad (4-2)$$

where a is the fiber radius and $r\ (\geq a)$ is the radial distance from the axis of the fiber (Fig 4.12A) to $P\ (r,\ z)$ where the potential $\varphi^{is}(r,z)$ is calculated; s represents the center of the charge distribution associated with the action potential. When an anisotropic volume conductor is modeled, the potential (φ^{an}) can be expressed (Plonsey [45]) by:

$$\varphi^{an}(r,z) = \varphi^{is}\left(r\sqrt{\frac{\sigma_z}{\sigma_r}},z\right) \times [\frac{\sigma_r + \sigma_z}{2\sigma_r}] \qquad (4-3)$$

and eqn. 4 becomes:

$$\varphi^{an}(r,z) = \frac{\sigma_r + \sigma_z}{2\sigma_r}\frac{a^2}{4}\frac{\sigma_i}{\sigma_e}\int_{-\infty}^{+\infty}\frac{d^2V_m}{ds^2}\frac{1}{\sqrt{\frac{\sigma_z}{\sigma_r}r^2+(z-s)^2}}ds \qquad (4-4)$$

where:

$$\frac{dV_m}{ds} = 3 \times 96 \times s^2e^{-s} - 96s^3e^{-s} \qquad s > 0 \qquad \Rightarrow$$

$$\frac{d^2V_m}{ds^2} = 6 \times 96 \times se^{-s} - 6 \times 96s^2e^{-s} + 96s^3e^{-s} = 96s^{-s}s(6 - 6s + s^2) \qquad s > 0 \quad (4-5)$$

With eqn.4-5 in eqn.4-4:

$$\varphi^{an}(r,z) = \frac{\sigma_r + \sigma_z}{2\sigma_r} \frac{a^2}{4} \frac{\sigma_i}{\sigma_e} 96 \int_{-\infty}^{+\infty} \frac{s(6 - 6s + s^2)e^{-s}}{\sqrt{\frac{\sigma_z}{\sigma_r}r^2 + (z - s)^2}} ds \qquad (4-6)$$

with: $\frac{\sigma_z}{\sigma_r} = 5$ and $\frac{\sigma_i}{\sigma_e} = \frac{1}{3}$, the above equation becomes:

$$\varphi^{an}(r,z) = 24a^2 \int_0^\infty \frac{s(6 - 6s + s^2)}{\sqrt{5r^2 + (z-S)^2}} \exp(-s) \, ds \qquad (4-7)$$

which represents the spatial potential distribution around a fiber, measured at point *P(r, z)* where *z=vt* (Fig 4.12.A). Very close to the outside surface of a fiber, a SFAP waveform is illustrated in Fig 4.12.B when a conduction velocity of v=5 m/s is assumed. In this figure, the amplitude of each SFAP was chosen from a normal distribution varying between 0.25 and 10 µV with an activation time spanning from to 5000 ms. For the 3 simulated signals, it was assumed that the fibers (~20 µm in diameter) where parallel to each other and tightly and uniformly packed within a circle lar radius of 2 mm as with the real dipoles Three current sources were considerd to be put in the tank with a mean fibers distance of 10 mm from the border and in front of electrodes #3,#7 and #11 (Fig 4.4).

The SFAP results from the ionic current associated to the intracellular action potential (IAP) propagating along a muscle fiber. This current is proportional to the first derivative of the IAP and is given by: $\frac{\partial \Phi_i}{\partial z} = -r_i I_i$ where Φ_i is the IAP, I_i the intracellular current and r_i is resistance per unit length (Ω/cm). Moreover conservation of current requires that the axial rate of decrease in the intracellular longitudinal current be equal to the transmembrane current per unit length: $\frac{\partial I_i}{\partial z} = -i_m$ where i_m is the current of transmembrane (Fig4.14) [36].

Therefore transmembrane voltage is: $\frac{\partial V_m}{\partial z} = \frac{\partial \Phi_i}{\partial z} - \frac{\partial \Phi_e}{\partial z} = -r_i I_i + r_e I_e$,where I_e is extracellular

current. The extracellular longitudinal current may decrease with increasing z either because of a decrement of the transmembrane current or a loss that is carried outside when intracellular electrodes are present:

$$\frac{\partial I_e}{\partial z} = i_m + i_p$$

where i_p is the current of electrodes. Therefore deriving a second time is:

$$\frac{\partial^2 V_m}{\partial z^2} = -r_i \frac{\partial I_i}{\partial z} + r_e \frac{\partial I_e}{\partial z} \Rightarrow \frac{\partial^2 V_m}{\partial z^2} = r_i i_m + r_e(i_m + i_p) = (r_e + r_i)i_m + r_e i_p$$
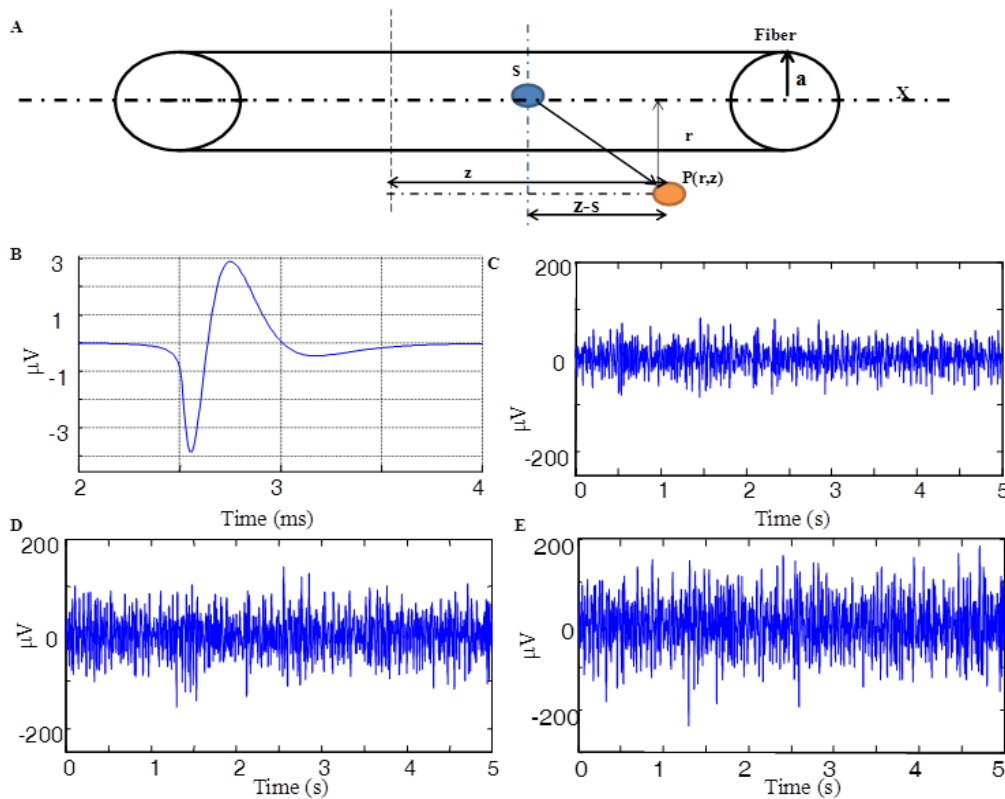
Fig 4.12. A: Diagram where s represents a charge distribution on the axis of a fiber (r=0). The perpendicular distance from the fiber axis, a represents the fiber radiue. The horizontal distance between the charge distribution (s) and the recording point P is (z-s). B: extracellular SFAP obtained with r slightly larger than a which is 20 μm. C. Simulation of SEMG obtained with the summation of 1000 SFAPs of random amplitudes as observed at a z-s and r value of respectively aa and bb mm. D: a sum of 2500 SFAPs and of 5000 SFAPs in E under the same measuring point.
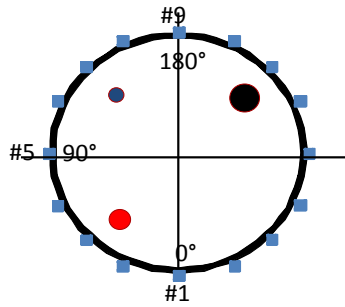
Fig 4.13. Dipole positions considered in the simulation. Size of the circles is proportional to the intensity associated to each dipole.

In our simulations, in each active zone, 5000 SFAPs where packed within a 3 mm radius and the potential recorded at each recording electrode was obtained by rhe Okada's equation.
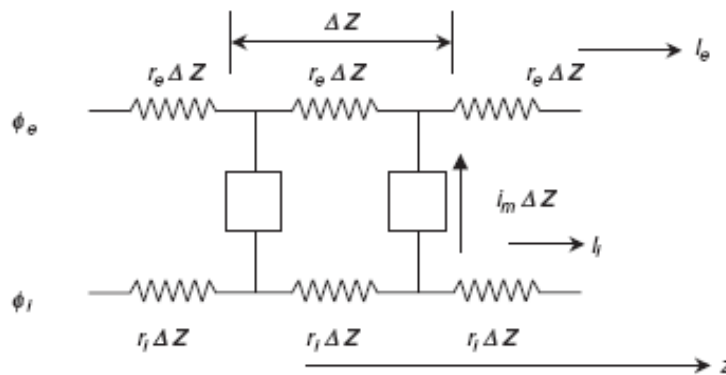
Fig. 4.14: Linear core-conductor model representing a portion of the fiber membrane. For graphical representation the structure is shown as a repetitive network of finite length Δz, but in fact $\Delta z \longrightarrow 0$; the analysis is based on the continuum. The open box is a symbol representing the equivalent circuit of the membrane, which depends on the membrane state, namely a passive structure during the resting period and a circuit with time-dependent components during the active phase.

To model the amplitude decay of the SFAP signal at distance from its source, this Okada formula is used:

$$V_z(\rho\ \phi\ z) = \frac{-p_z}{L^2\sigma} \sum_{m=0}^{\infty} (2-\delta_{m0}) \cos\left[m(\phi-\phi')\right] \sum_{n=1}^{\infty} n I_m\left(\frac{n\pi\rho'}{L}\right) \left[K_m\left(\frac{n\pi R}{L}\right) - \frac{K_m'\left(\frac{n\pi R}{L}\right)}{I_m'\left(\frac{n\pi R}{L}\right)} I_m\left(\frac{n\pi R}{L}\right) \right] \cos\left(\frac{n\pi z}{L}\right) \sin\left(\frac{n\pi z'}{L}\right)$$

(4-8)

where I_m, K_m is the first and second kind of modified Bessel and δ is delta function and where ϕ' represents the angle between the X axis and the dipole position in the XY plane and the height of the liquid level in the tank is represented by L. Moreover, R is the radius of the tank and ρ' is the radius distance of dipole. Using the mean absolute value (MAV) of the signals amplitude,

comparison was made between the experimental tank signals and those with the 3 dipoles each made of 5000 SFAPs As shown in Fig.14.5A, the dipoles were placed in front of electrodes #3, #7 and #11. They were placed at 10 mm from the border of the tank with a relative intensity of 2, 1 and 4 obtained by each SFAP amplitude which was picked up from a normal distribution spanning between 0,25 to 10 µV for the dipole near electrode #3, 0,25 to 20 µV for the dipole near electrode #7 and 0,25 to 40 µV for the 3rd one.
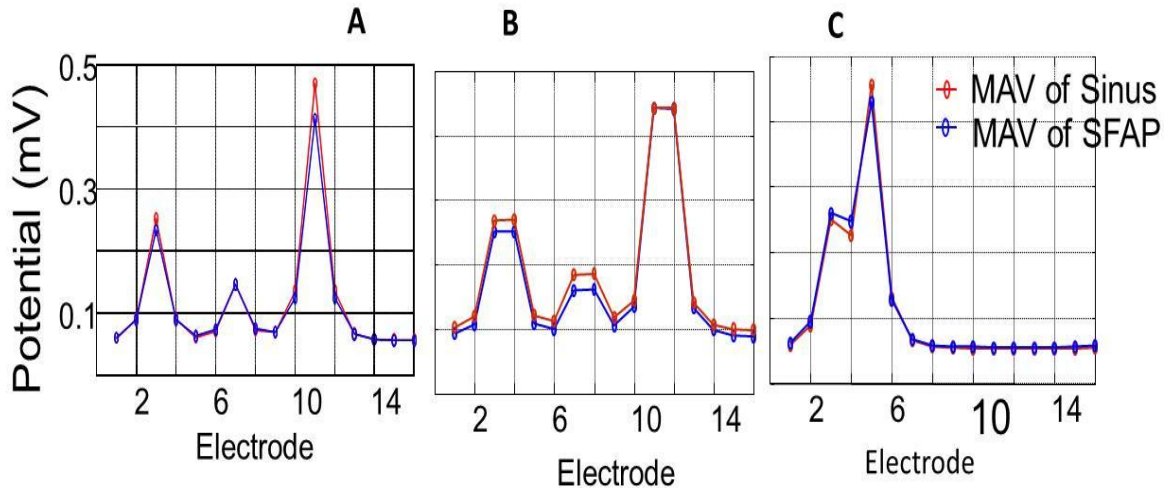
Fig. 4.15. Blue lines: results obtained with sinusoidal current applied to 3 dipoles in the tank as in Fig.4.13 and red lines results are associated to 3 dipoles each made up of 5000 SFAPs. Mean absolute value (MAV) potential is used in both situations and the 3 dipoles are at 10 mm from the tank border Relative intensity of the dipole in front of eletrode #3 was 2, it was 1 for the dipole in front of electrode #7 , an 4 for the dipole in front of #11 as easily seen in panel A..Results in panel B were obtained when each dipole position was angularly moved anticlockwise by 11.25° (half angular position between 2 adjacent electrodes). Between electrodes #10 and #12 the results were identical and the blue line is hidden below the red one. Results in panel C were obtained when the dipoles are in front of electrode #3, #4 and #5.

In Fig. 4.15, results with the sinusoidal currents (red lines and markers) are superposed to those obtained with the SFAPs modelling. Three bundles, each made of 5000 fibers but considered to produce a relative intensity of 2, 1 and 4 were used. In panel A, with such a setup, results are particularly similar when each dipole is in front of a recording electrode. In panel B, the fitting is less good for the first 2 dipoles but better for the third one with intensity of 4. When the dipoles were closely positioned i.e. in front of electrodes #3, #4 and #5, only dipoles in front of electrodes #3 and #5 can be clearly recognized while the weakest dipole in front of electrode #4 can only be suspected. The limit on how close the dipoles could be positionned and still be

individually identified is thus partly dependent on their respective strength; Increas in the number of electrodes or of the distance between the dipoles would facilitat individual detection.

To solve the inverse problem with signals simulated as in Fig. 4.12C, D and E, we considered the Fourier transform of the signals obtained with 3 dipoles of different intensities positioned in the tank at 7 cm distance from the tank center and placed in the same horizontal plane in front of electrodes # 3, 7 and 11 (Fig 4.13). Amplitude of the signals detected at the electrodes is illustrated in Fig 4.15 and FFT of electrodes 2 to 9 shown at Fig 4.16. A moving average was used to smooth those spectra (Fig. 4.17).
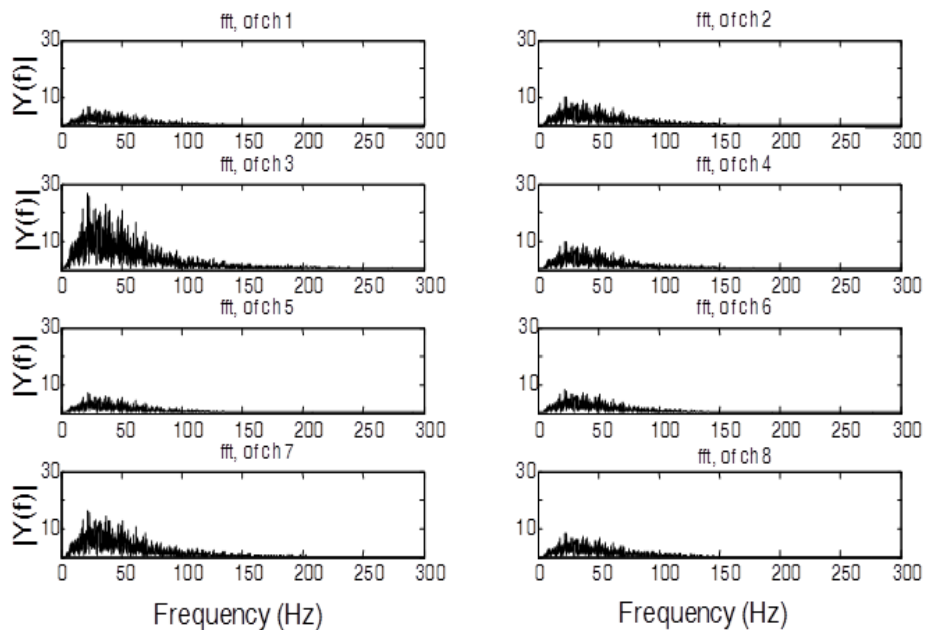
Fig 4.16. The FFT of signals at electrodes 2 to 9 around the tank when three dipoles are in the tank which has one isotropic environment.

To solve our inverse problem we considered that when all channels share similar frequency behaviour the location and intensity of our zones of activity could be found using the frequency where the amplitude is maximum. In the search of that frequency, the spectra were shown in Fig 4.16 where filtered with a moving average. We used the MATLAB command *smooth (Y,SPAN,METHOD)* where Y is the signal, SPAN represents the number of signal samples which

was 7 and METHOD was Moving average. As shown in Fig. 4.17, similar frequency behavior is observed for each displayed signal.
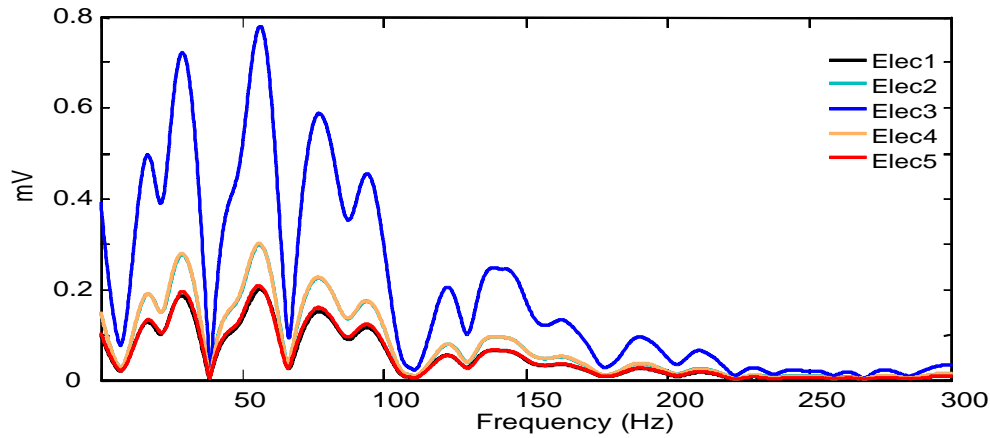
Fig 4.17. Smoothed FFT of 5 of the signals shown in the previous figure.

In the inverse problem, the difference between observation data and calculation values has to be minimized. Solving this in 2D, we assumed that each dipole was placed at the same level (z) in the tank and we just have to define the ρ' and φ' for location of current sources:

$$min\|J\| = \sum_{i=1}^{N} (V_z(\rho', \varphi', z') - V_{i,observed})^2$$

From the peaks displayed in Fig. 4.15, we know that there are three dipoles. To minimize the FFT of electrodes signal and FFT of $A_1 \sin(\omega t + \varphi_1) + A_2 \sin(\omega t + \varphi_2) + A_3 \sin(\omega t + \varphi_3)$ (that A_1, A_2, A_3 are related to the intensity and the place of dipoles and ω is one frequency that has the highest value and φ_1, φ_2 and φ_3 are the phase of signals). After 100 GA iterations we switched to NCG method (Fig. 4.18) and the results are presented in Fig. 4.19.
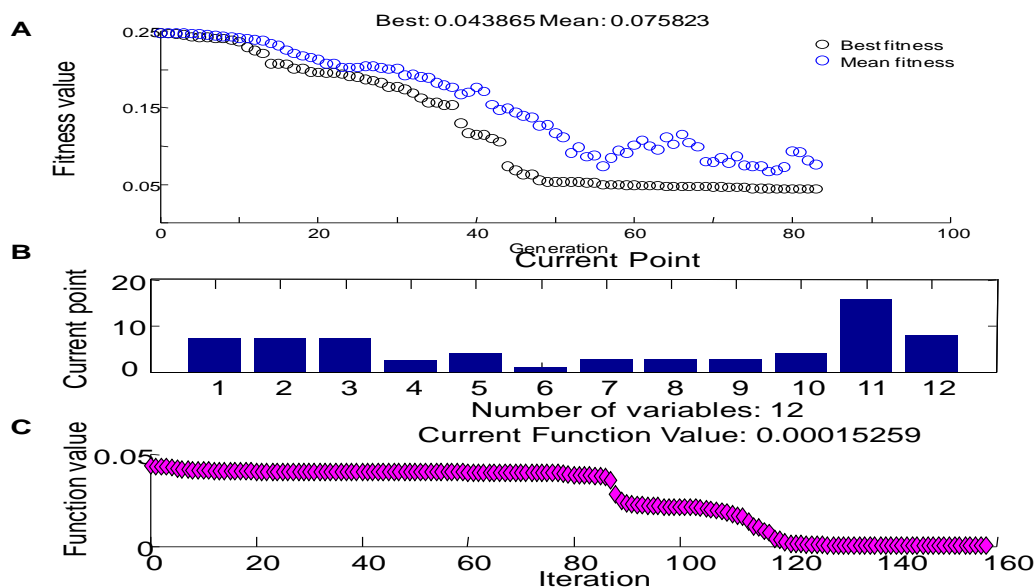
Fig. 4.18. **A)** The fitness value in GA **B)** The values of radius, angles and intensities **C)** Error in NO method. The first third values are radial distance from the center, the second third values are the angle values and third third values are the relative intensities and the last one is the phase of signal.

	Forward			Inverse			Error (%)		
R(cm)	Phi(°)	I	R(cm)	Phi(°)	I	R%	Phi%	I(%)
7.	45	2	7.001	45.07	2.008	0.014	0.15	0.4
7.	135	1	7.002	135.05	1	0.028	0.037	0
7.	225	4	6.998	225.11	4.004	-0.028	0.048	0.1
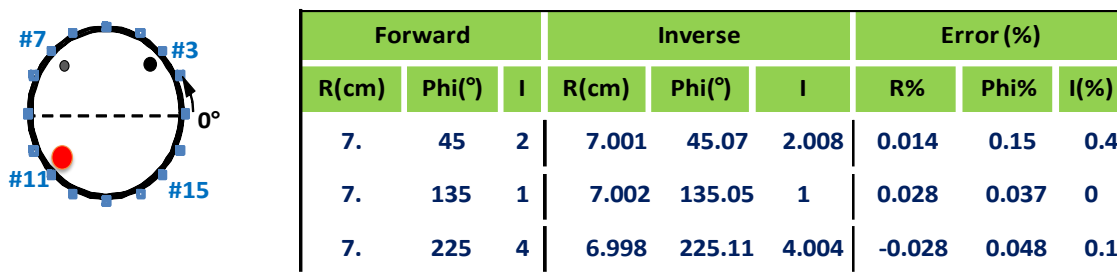
Fig. 4.19. Comparison between the forward and inverse model results with 3dipoles.

4.3 EMG signals collected over the bicep brachii (BB) muscle

We will now be dealing with EMG data already collected from normal subjects by a master student [40]. She explored many positions of the upper limb and of the hand to find how to activate, in group or individually, the 6 compartments of the biceps brachii muscle. Out of the explored positions, she identified 3 body positions coupled with the 3 hand postures (Fig.4.20A

and B) which appeared most promising to reach that goal. As for the tank data, the signals were amplified (gain of 2000), filtered (10-1000 Hz) and digitized (2 kHz).
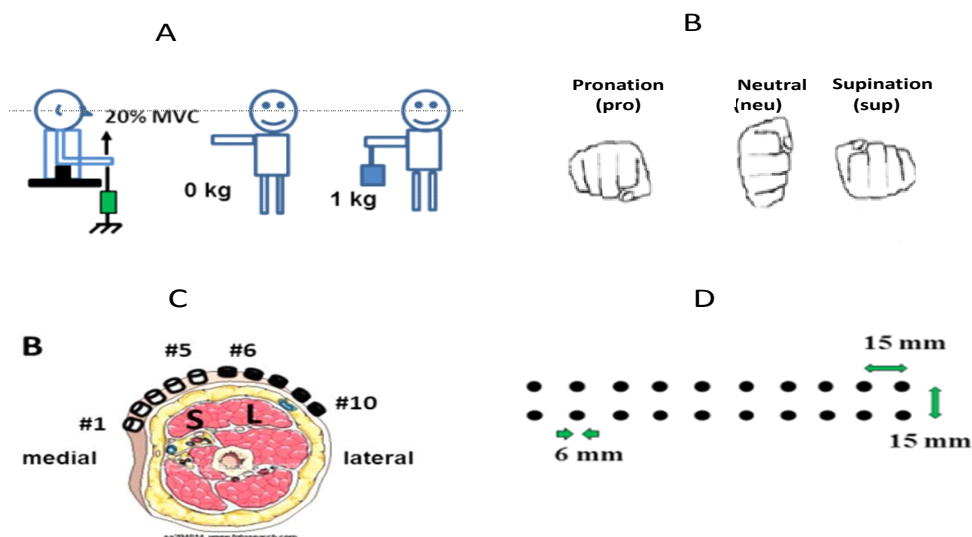
Fig 4.20. A. Three body positions used to collect the data. B. Three hand positions experimented during each body position. C. Five pairs of surface gold–plated electrodes where placed over the short (S) and long (L) heads of the BB muscle. D.Information on the electrode matrix used.

A sample of the recorded EMG signals is shown in Fig. 4.21. The subject was in the seated position, the elbow flexed at ~90°. He contracted the biceps to produce an elbow contraction at 20% of his maximum volountary contraction level (MVC) while his hand was in pronation.
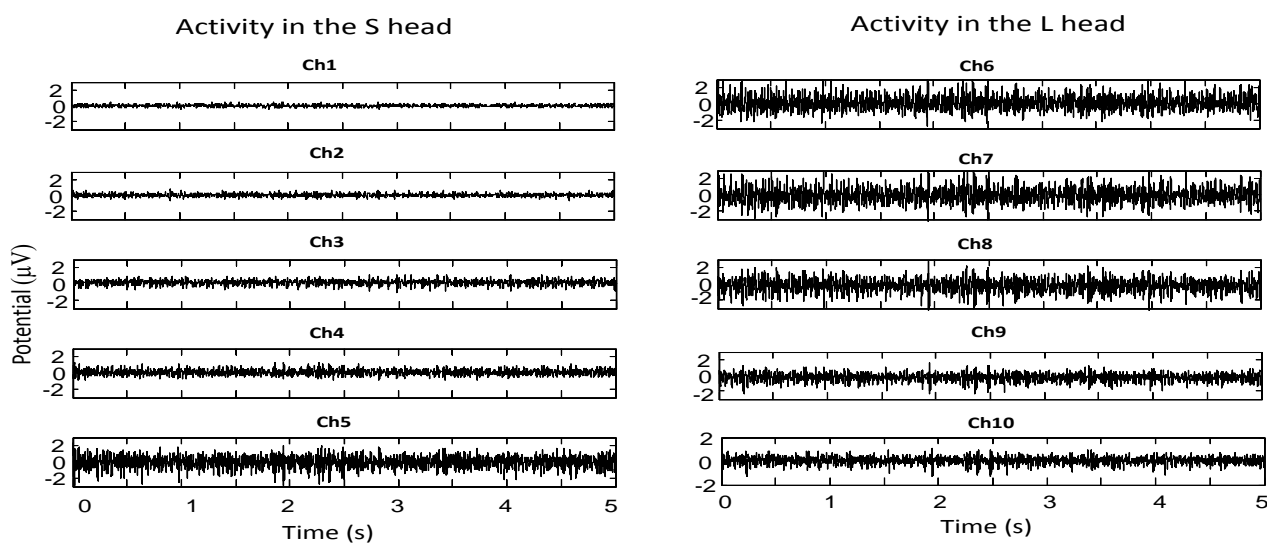
Fig 4.21 Ten EMG signals collected over the BB during a 20% MVC contraction while the subject was seated and the hand in right elbow flexed ~100°. Same amplitude scale for each signal.
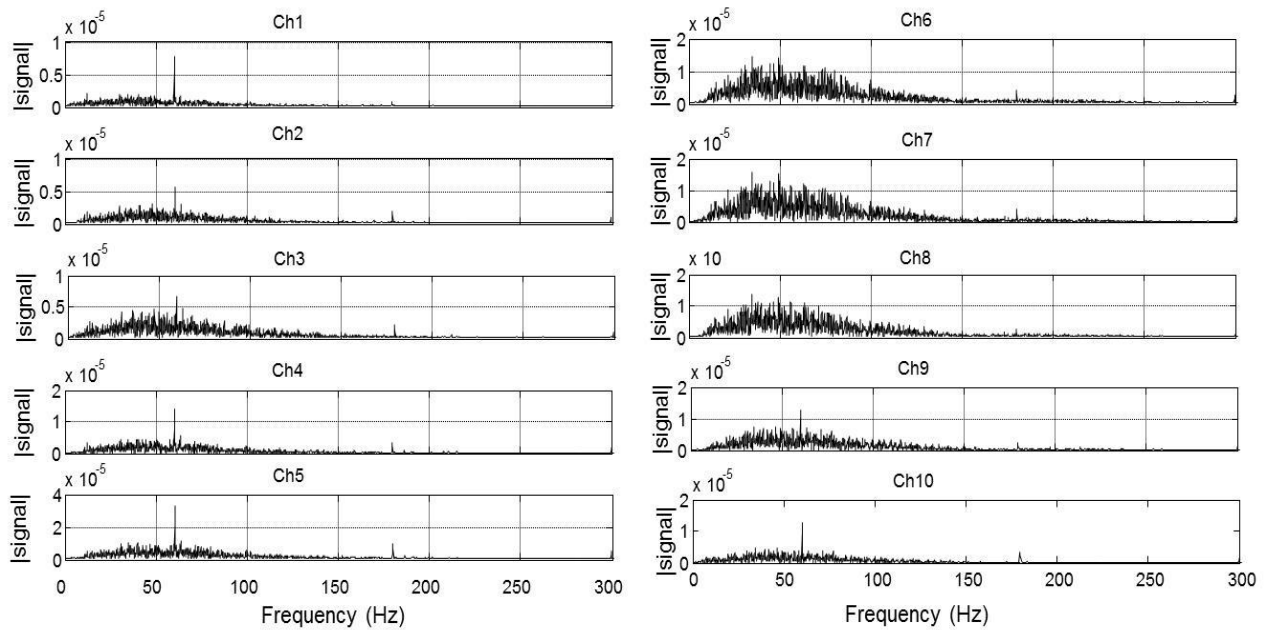
Fig 4.22. FFT of the 10 signals displayed in the previous figure.

To establish a cost function, as done with the tank data, the FFT of each EMG signals was obtained (Fig.4.22), To facilitate the extraction of valuable information from those spectra, a smoothing was initially done with a moving average (10 samples with a 5 samples overlap) and the results are shown in Fig 4.23A. From the various peaks, the one at 65 Hz was the largest but being close to the power line frequency, the peak at 49 Hz was initially considered. Even smoother spectra, the Welch method was used (8 windows with a 50% overlap) and the results are shown in Fig 4.23B. Using the peak amplitude (the black dotted line), 49 Hz was picked up. from the given data set and varied between 45 and 65 Hz for the other analyzed situations as shown in Table 4.2. At each of those frequencies, the amplitude of each of the 10 spectra was used in the cost function associated with a given data set.

A circle, with a radius deduced from the measure circumference measured at the electrodes level position, is used as a model of the arm cross-section. The lengh of each spoke radiating from the circle is proportional to the RMS or MAV value of the signal recorded over each electrode.

Table 4.2. Peak frequency identified for individual (T1,T2,T3) and average (Av) trials. Each Av trial correpond to the average of signals in T1,T2 and T3.

Condition/Subject	PM								MM							
	Pronation (Hz)				Supination (Hz)				Pronation (Hz)				Supination (Hz)			
	Av	T1	T2	T3	Av	T1	T2	T3	Av	T1	T2	T3	Av	T1	T2	T3
Standing- 1Kg	62	69	60	62	53	48	45	53	64	63	62	64	60	59	59	60
Standing 0kg	53	49	51	55	47	46	51	46	61	59	61	61	58	59	56	58
Sitting-20% MVC	48	49	45	48	58	59	64	58	54	57	50	54	53	54	59	53
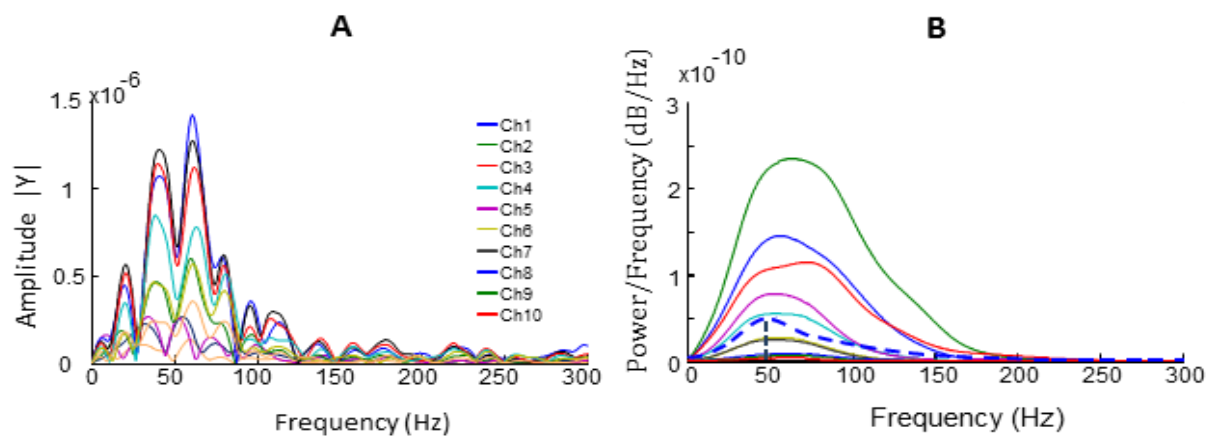
Fig 4.23. A. Smoothed version of the FFT shown in the previous figure. B. Ten Welch spectra of Fig.4.17 signals with their mean value (dashed line) with a peak at 49 Hz.

When the RMS values of the recorded signals where displayed, 3 active areas where found to be similarly positioned in each of the 3 trials when the subject was in the seated position with the hand either supinated or pronated (left of Fig.4.24). In the standing position, 3 active areas are also seen in the supinated hand position but not in the pronated position. Considerint the prevalence of one situuation, we assumed that 3 zones of activities were always present.
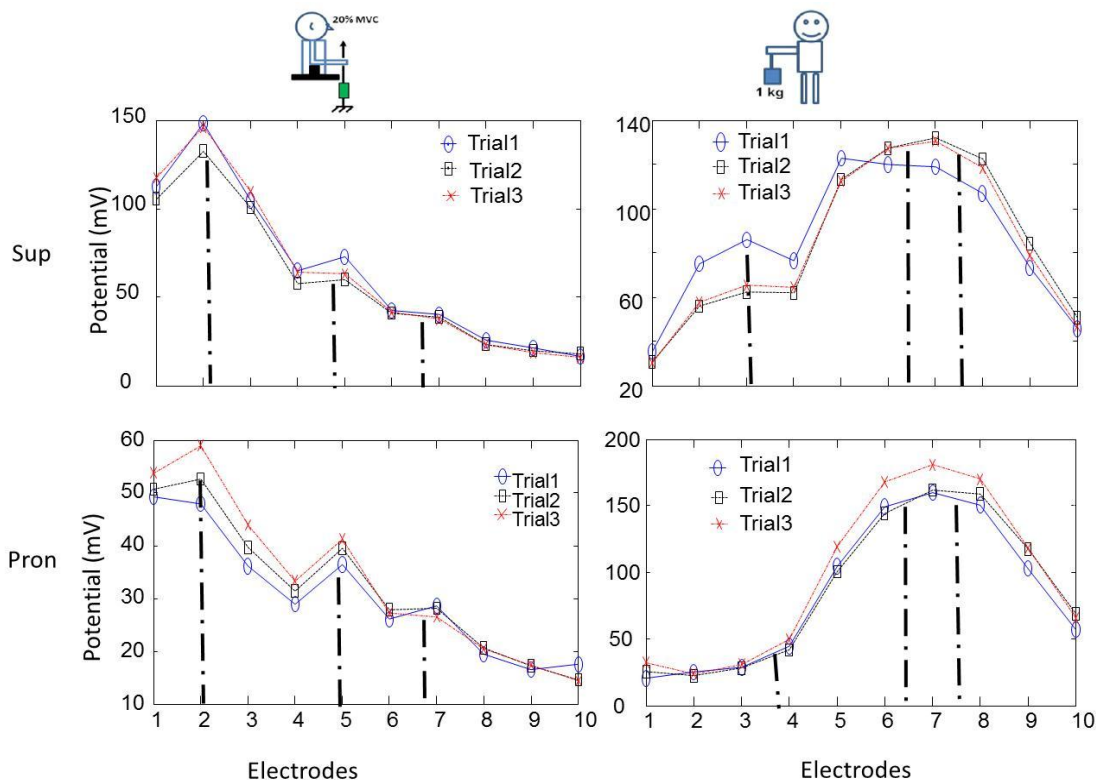
Fig 4.24 Electrode RMS values obtained for 3 individual contractions with hand supinated and pronated in 2 body conditions for subject PM. In the sitting condition a peak is detected at electrode #2, another around electrode #5 and a third one around #8. In the standing condition, peaks around electrode #3, #6 and #8 can be seen.

4.3.1 Results with subject PM

In the seated position with the hand supinated, (left of Fig.4.25), the 3 active areas where found to be similarly positioned in each of the 3 trials. The most important dipole (red one) could have been in the middle of the anatomical contour of the S head of the BB while the second more important (blue one) was located near the division between the S and L head. As for the less important dipole (black one) it was located within the L head. As for their distance from the periphery of the circle which has a radius of 43 mm (estimated from the measured circumference of the subject's arm) they ranged between 7 to 19.83 mm which suggest that the 3 zones of activity where, as expected, within the BB. With the hand in pronation, similar positions where obtained while the intensity of each dipole was less than in the supination position for the red and blue dipole.
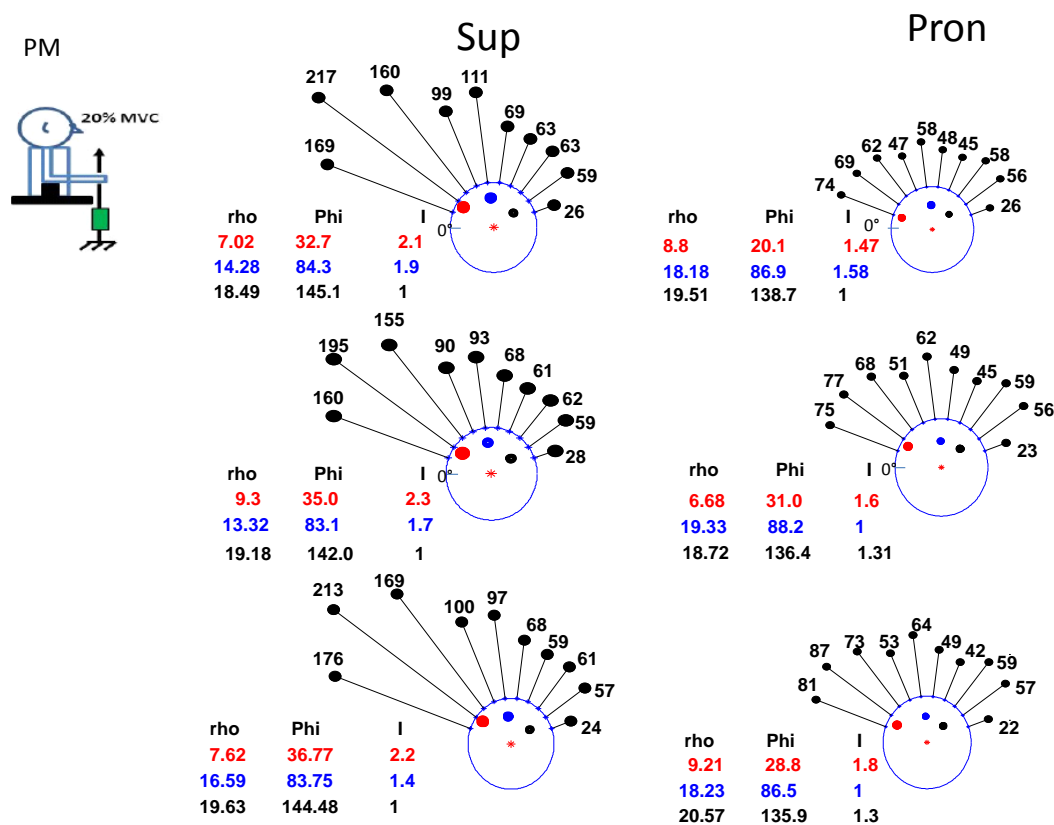
Fig 4.25. Three experimental trials of seated subject PM when his hand was supinated (Sup) and pronated (Pron). The figures around the tip of each spoke is the MAV value (µV) of the signal collected by each electrode Both in supination (Sup) and pronation (Pron), 2 dipoles are associated to the activity within the short head and one in the long head of the BB. In the figure, 0° is considered to be at the left of the circle and angular values (phi) are measure clockwise. The position of an active area (rho) is from the border of the circle used to represent the arm and I is a relative intensity of each dipole. For this subject, the radius of the circle was 43 mm.

In another body position, the subject was standing up with the right arm extended horizontally in the coronal plane (90°shoulder abduction) without load and the hand either supinated or pronated. As illustrated in Fig 4.26, for the 3 trials, the two most important activities (blue and black dipoles) are mostly located in the L head near the medial part of the BB while the less powerful red dipole was located in the S head. It can also be noticed that while the blue dipole intensity was larger than the black intensity in 5 situations out of 6 and that its angular location was greater than the black one when the hand was supinated, the inverse was observed in the pronation position.

PM

Sup

Pron

0 kg

Sup - Trial 1

124   159   162   144
53   98
35
19   55
22

rho	Phi	I
21.72	52.8	1
9.65	104.3	2.1
12.23	122.01	1.9

Pron - Trial 1

127   105   133   119
49   82
47
24   44
20

rho	Phi	I
19.57	28.8	1
13.99	118.2	2.5
10.57	92.4	2.1

Sup - Trial 2

105   128   135   122
50   84
51
26   45
20

rho	Phi	I
20.25	32.7	1
15.8	121.5	2.2
11.65	99.8	1.5

Pron - Trial 2

153   117   160   144
50   100
35   56
18
20

rho	Phi	I
20.43	55.1	1
13.12	94.6	2.2
16.86	118.7	2

Sup - Trial 3

119   154   162   146
50   102
36
18   59
20

rho	Phi	I
21.32	50	1
12.58	91.2	1.75
18.72	117.6	2.2

Pron - Trial 3

103   121   128   117
48   .83
48
24   47
21

rho	Phi	I
19.01	26.4	1
14.64	119.2	2.2
12.08	91.1	1.8

Fig. 4.26. Same situation as in the previous figure except that subject PM was standing up with his arm extended laterally without load. Positions of the dipoles are somewhat similar to the previous figure except that the intensity of the red dipole is now smaller than for the 2 others and that the blue and black dipole relative angular position is different depending on the hand position.

In the third considered situation, a weight of 1 kg was added at the wrist level. The zones of activity in the BB in this condition are illustrated in Fig 4.27. In comparison with the no load situation, intensity of the blue and black dipoles are greater and their relative angular position is not modified with a change in the hand position while teir position relative the the S head is similar to the no load situation. In the 2 first trials, the black dipole is more powerful that the blue one in 2 of the 3 trials while in pronation, it is the blue dipole which has more strenght than the black one in 2 of the 3 trials.
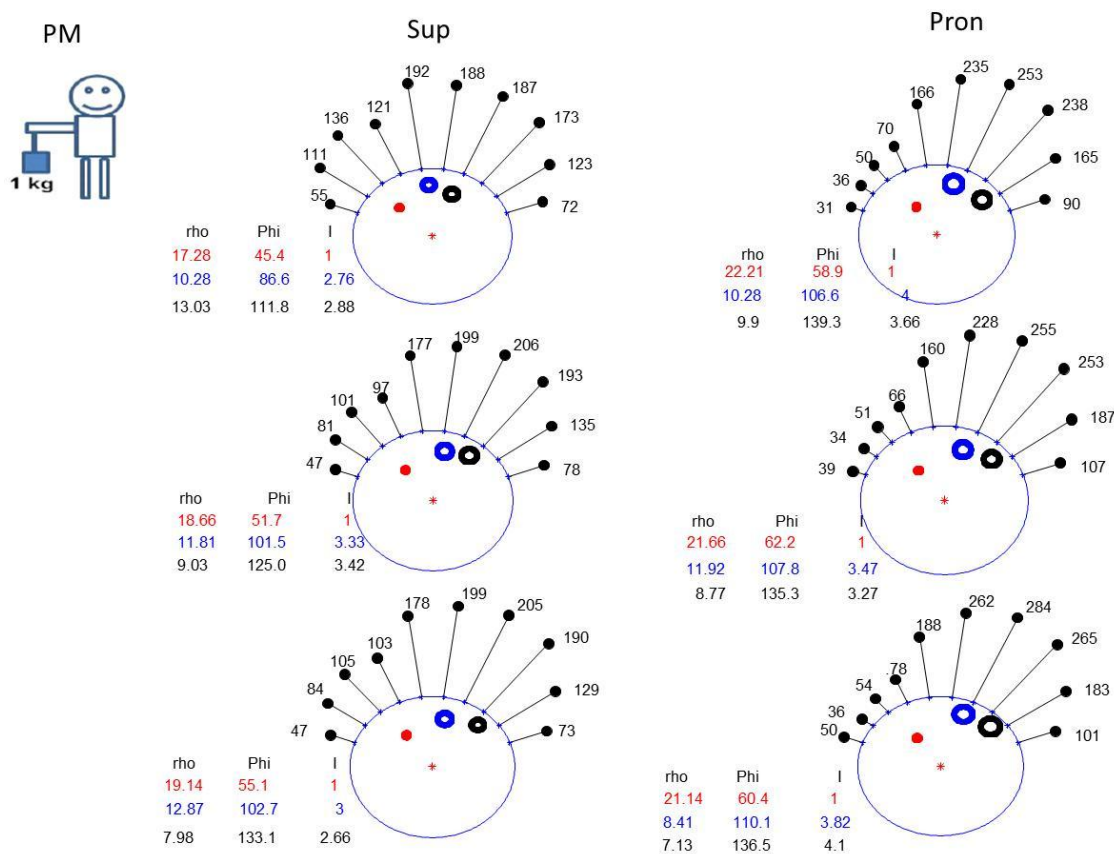
Fig 4.27. Three experimental trials of the standing up subject PM with a 1 kg load at the wrist. While the detected activity is similar to the standing position without load, the intensity of the blue dipole is now the largest.while the red dipole position appear to be shifted clockwise particularly when the hand was pronated.

4.3.2 Results with subject MM

Since the results obtained with subject PM in each individual trial were quite similar, the 10 MAV values obtained in each of the 3 trials of subject MM were added and a mean value was obtained for each of the 10 signals. The activity zones obtained from the mean MAV values are presented in Fig. 4.28 for the 2 hand positions and the 3 body postures. As can be seen from the numerical values and length of the spoles the muscular activity was quite less than for the previous subject. However as with subject PM, only one zone of activity was detected within the S head. In supination, the position of the dipole within the S head was near electrode #4 both in the sitting position and in the position with a 1 kg load but their intensities were not the same. In the standing position without loas the dipole wiyhin the S head moved toward electrode #2. In pronation, activity within the S head eas also either in front of electrode pair #2 or #4. As for the

activity within the L head, both in supination and pronation, activity was in front of #6 and #8 electrode pairs in all 3 body positions while the distance from the circle border varied.
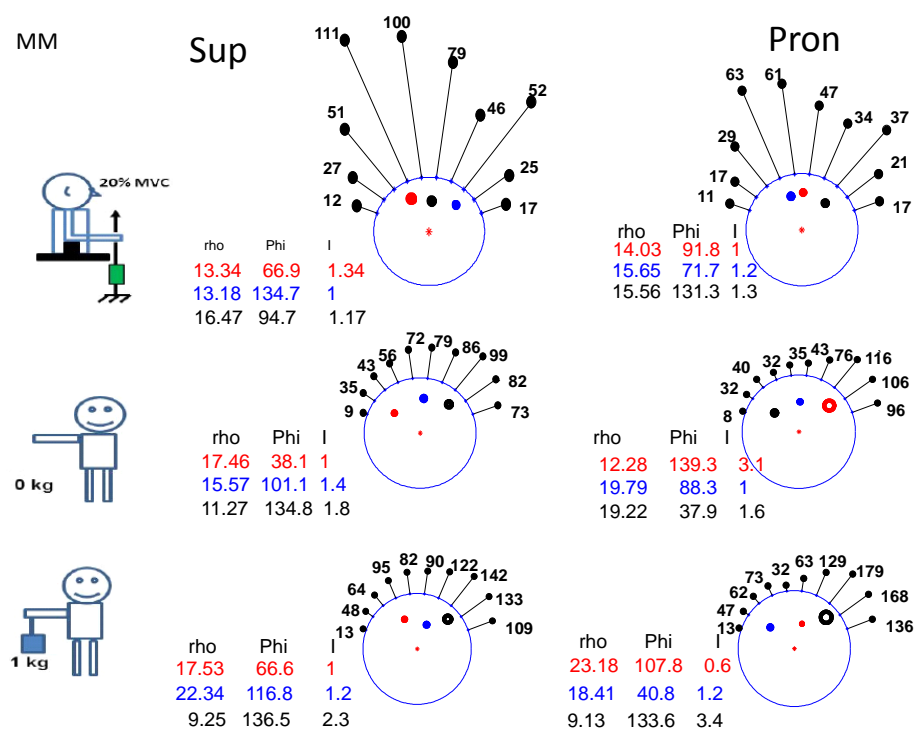
Fig. 4.28. Averaged results obtained for the 3 trials of the MM subject as collected in 3 body positions. Each lenght of a spoke is proportionnal to the average MAV values obtained from the 3 individual trials.

CHAPTER 5

5.1 Discussion

In relation to the activation of the biceps brachii compartments, a direct and inverse model was developed to help locate zones of activity within those muscles as 2 normal subjects produced different contractions. To elaborate those models, we initially analyzed experimental signals collected around a circular tank filled with saline and where up to 3 dipoles were inserted.

For the direct model, an analytical model based on Okada and Lambin-Troquet (42, 30) was chosen considering the simple shape of the circular tank. For the inverse model, an over-determined method was selected because of the limited number of compartments within the BB. For this purpose, the same model used in the direct model was used to generate simulated signals. From the smoothed spectra of each signal, a mean spectrum was obtained from which the frequency at which amplitude was maximum was picked up. At that frequency, the amplitude of each individual smoothed spectrum was used in the cost function. To find an initial minimum point in the cost function, a genetic algorithm was used and from this point, the search of an optimum point was done with a nonlinear optimization method since convergence toward a global minimum is faster than with GA.

Initial models of the upper arm consisted in a single cylinder for which analytical models can be used to evaluate the propagation of signals within the enclosed volume and on its border. More realistically, a 3 concentric cylinders model was proposed (34) and magnetic resonance imaging was even used to get very realistic personalized situations (56, 57). To elaborate our direct and inverse model, a simple cylinder was used considering that the first available experimental data were those obtained from a circular tank in which dipoles where placed at known positions. With the inverse model, the dipoles coordinates and intensity were correctly detected in all the studied conditions. To obtain those results, the peak frequency of a mean spectrum obtained from the individual smoothed spectra available in a data set was used as representative of the trial. At that frequency, the amplitude of each individual spectrum was used in the cost function to localize the position of the current sources.

Simulated signals derived from the activity of many single fiber action potentials were produced and analyzed with the inverse model. Good results were also obtained. When white Gaussian noise was added to the original signals, the differences between the simulated and inverse results increases as the signal to noise ratio was reduced as expected but a good detection was still present.

A for the analysis of experimental EMG signals, it was planned to use a 3 concentric cylinders with 5 principal internal divisions as illustrated in Fig. 3.6D. However, due to time constraints this was not possible and the single cylinder model was also used with EMG signals. However in spite of the simplicity of the model used, all the located zones of activity obtained from the data of 2 subjects, were, from their distance from the border, always within the biceps. More specifically, in the seated position it was found for subject PM that 2 zones of activities were found in the S head of the biceps while the other one was found in the other head. Intensity of the dipoles in the S head was larger than the dipole positioned in the L head. For subject MM, the results obtained from the mean MAV values of 3 trials, similar good results were obtained but, in difference with the PM subject, 2 zones of activity were located in the medial portion of the L head and only one in the S head.

In both hand positions in the standing position without load, 2 zones of activity were always found for PM in the medial part of L head with an intensity nearly doubled as compared to the dipole in the S head. For subject MM, with the mean results from 3 trials, the 2 zones of activity in the L head were less closely positioned than found. As for the standing position with 1 kg load, the dipoles position are similar to the no load situation and as expected the intensity of some dipoles is higher for both PM and MM subject. For subject PM, intensity of the 2 dipoles in the L head was 2 to 4 times larger than for the other dipole in the S head. A similar situation for the dipole intensities was found for subject MM. However difference in the position of his dipoles within each head was different from those for PM.

Such dipole locations and variation in their intensity, confirms the indications obtained from surface EMG RMS values that it is possible, through different body and hand positions, to voluntary activate either the long or the short head of the biceps. In addition to that results, the position of our dipoles within the biceps is giving some insights on which compartment within those heads could have been activated. This can be observed in the following figure.

In the left column, the activity zone within the short head could be lying either in the compartment 1 or 2 depending in the body position while in the long head, the 2 activity zones remain mainly fixed in compartments 4 and 6. In the standing position, intensity of the dipole in the short head is reduced while it is increased for those in the long head. In the middle column where the hand is in pronation, the location of the activity zones is similar to the supinated hand position but intensity of the dipoles increased in the long head while the subject was standing up.

In the right column, it would seem that in the seated position, the localization of the 3 dipoles are within the biceps muscles outline while in the standing position without load one dipole is between the biceps and the muscle under it while a second one is located partly outside the biceps and within nerves and arteries, It can be observed with the 1 kg load, that an important dipole would have been located within the fat and skin layers which is impossible in real world. Such results indicate that the models used are capable to produce plausible results but may need improvement if erratic solutions are also found for the other 8 subjects. This could also be an indication that a more personalized cross-section image of the upper arm should be used instead of a generic one.

In our work various source of errors where present. For the tank data, the 2 mm diameter of the dipole when close to a 10 mm diameter recording electrode could have induce some distortion in the recorded potential from that electrode. The metallic grid placed at the bottom of the tank does not exactly be considered as a far distant reference point considered in the Okada model.

Attention was used with the positioning of the dipoles within the tank but it cannot be said that the positioning was precise. Signals were contaminated at various levels with 60 Hz.
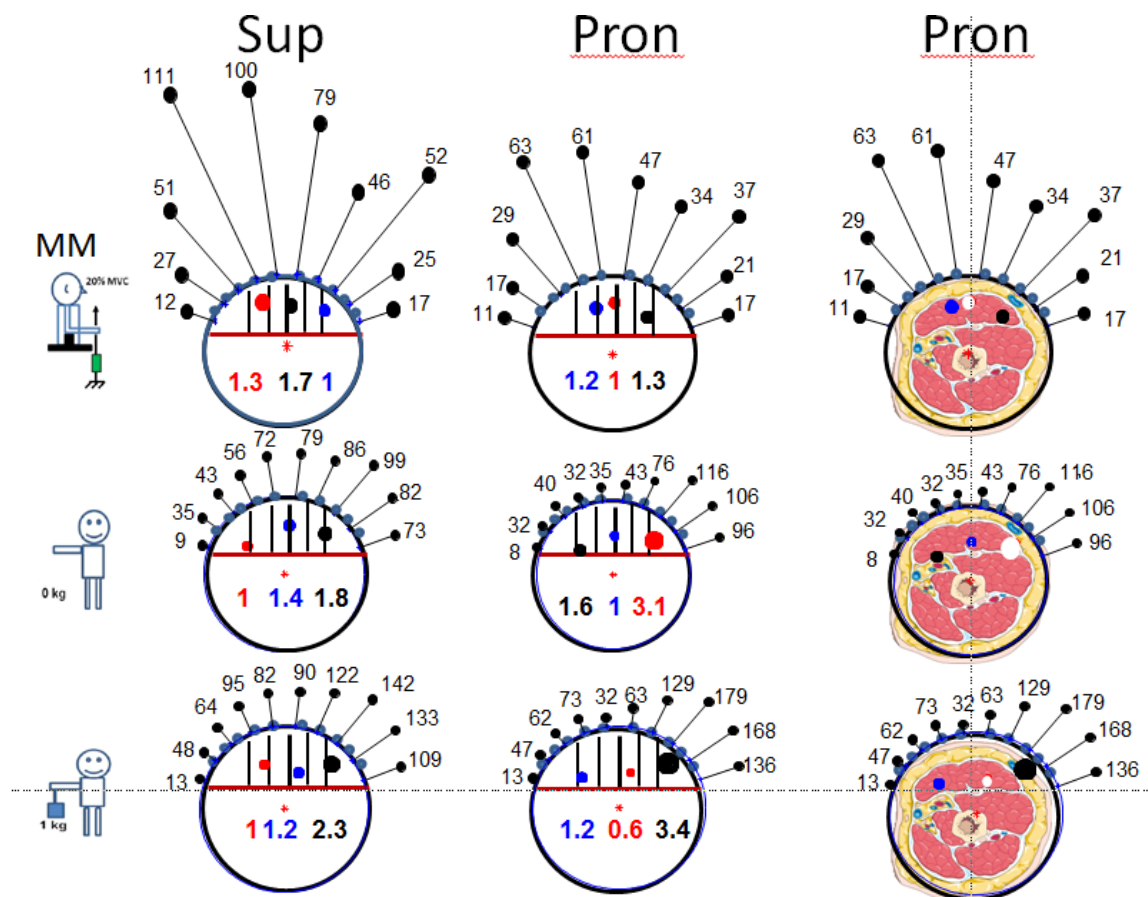
Fig 5.1 Mean results of subject MM. In the left and middle column, superposition of the inverse model results with a schematic representation of the hypothetical repartition of the 6 compartments within the biceps whose lower border is represented by the horizontal red line. Each figure within the circles is related to the intensity of a zone of activity. In the right column, results obtained in pronation are superposed to a generic cross-section illustration of the anatomical upper arm structures at the level of the recording electrodes. White color has replaced the red one used in the center column for one of the zone of activity. Color is only used for visualization purposes; it does not track a particular zone of activity.

As for the experiments with normal subjects, the position of the electrodes could have been slightly modified as the body and hand positions were modified. In the standing position since no measurements were done on the spatial arm position, it was impossible for each subject to be exactly the same position. The use of a cylinder to model the upper arm is only a very simple

approximation of the physical shape of the arm. In addition only an homogeneous and isotropic volume conductor was considered while that volume is made of skin and fat layers which be considered as isotropic but with different conductivities. As for the muscle tissue it is anisotropic.

As for our inverse model the over-determined method gave acceptable results but the under-determined method could have been used. With this approach, any point within the area occupied by the biceps is a possible dipole location where intensity has to be determined. In the over-determined method both location and intensity of the active zones have to be determined. As an additional limitation, we only presented the results obtained from 2 subjects. The results have thus to be considered only as preliminary and need confirmation with the analysis of the data of additional normal subjects.

5.2. Conclusion

Using a simple cylindrical model to represents the upper arm, an analytical model of a direct model was established and used in the inverse one. To explain the 10 EMG signals collected over the biceps of few normal subjects during isometric and isotonic contractions, 3 zones of activity were assumed. Location of those sources within the short and long head appears to be compatible with the anatomical compartmental division of this muscle most of the time. It thus appears possible that the biceps compartments activation could provide a new avenue for improving the control of modern upper limb myoelectric prostheses. Work in improving the inverse model appears to be promising.

5.3 Future work

The first thing to do is to complete the analysis of the other 8 normal subjects from which data are presently available. Our volume conductor was considered to be homogenous and isotropic but the real situation is quite different. So new experiments with the tank could be realized where various materials of different forms could be inserted between the dipoles and the recording electrodes. Also with 4, 5 or 6 dipoles, more complex situations could produce results to check

the robustness of our inverse model. As for the arm model, an initial improvement would be to use three concentric cylindrical layers simulating the skin, fat and muscle. In such a model the muscular compartment could itself be divided in three parts to represent the biceps, the triceps and the brachialis which are present at the level where the electrodes are usually placed. To produce even more accurate anatomical model of the arm, the use of magnetic resonance images of the arm can be considered. With a software program, as COMSOL, to produce a mesh model of those images, a finite element method can then be used to solve the forward problem. Very interesting results could be obtained but important work; equipment and time need to be available. Finally, since the users of myoelectric prostheses are amputee persons, it will be important make recording with them to verify if they also could voluntarily activate their biceps compartments.

BIBLIOGRAPHIE

1. Blok J. H., Stegeman D. F., Van Oosterom A., "Three-layer volume conductor model and software package for applications in surface electromyography," Annals Biomed Eng, Vol 30, p. 566–577, 2002.

2. Blok J., Stegeman D., "*Simulated bipolar SEMG characteristics*," in H. J. Hermens, and B. Freriks, eds., SENIAM 5: The state of the art on sensors and sensor placement procedures for surface electromyography: A proposal for sensor placement procedures, Roessingh Research and Development, Enschede, Netherlands, 1997, p. 60–70.

3. Broman H., Bilotto G, De Luca C., "*A note on the non-invasive estimation of muscle fiber conduction velocity*". IEEE Trans BME, 1985, Vol 32, p. 341–343.

4. Burger HC, Tolhoek HA, Backbier FG, "The potential distribution on the body surface caused by a heart vector; calculations on some simple models", Am Heart J., Vol 48, p. 249-63, 1954.

5. Chanaud C.M., Pratt C.A., Loeb G.E., "*Functionally complex muscles of the cat hindlimb. V. The roles of histochemical fiber-type regionalization and mechanical heterogeneity in differential muscle activation*". Exp. Brain Res., 1991, Vol 85, p.300-313.

6. Chauvet E, Fokapu O, Gamet D, "Inverse problem in the surface EMG: a feasibility study", Proc. 23rd Annu. EMBS Int. Conf. (Istanbul, Turkey), p. 1048–1050, 2001.

7. Clark R.K, "*Anatomy and physiology: understanding the human body*". Jones & Bartlett Learning, 2005, Edition 1.

8. Côté J, Mathieu PA, "*Mapping of the human upper arm muscle activity with an electrode matrix*". Electromyogr Clin Neurophysiol, 2000, Vol 40, p. 215-223.

9. English A.W., "*An electromyographic analysis of compartments in cat lateral gastrocnemius muscle during unrestrained Locomotion*". J. Neurophysiol, 1984, Vol 52, p. 114-125.

10. English A.W, Letbetter W.D., "*Anatomy and innervation patterns of cat lateral gastrocnemius and plantaris muscles*". Am. J.Anat, 1982, Vol 164, p. 67-77.

11. English A.W, Wolf S.L, Segal L. "*Compartmentalization of muscles and their motor nuclei: the partitioning hypothesis*". Phys Ther., 1993, Vol 73, p. 857-867.

12. Farina D, Merletti R, Enoka R,M., "The extraction of neural strategies from the surface EMG", J Appl Physiol, Vol 96, p. 1486–1495, 2004.

13. Farina D, Mesin L, Martina S, Merletti R, "Comparison of spatial filter selectivity in surface myoelectric signal detection: Influence of the volume conductor model", Med. Biol. Eng. Comput, Vol 42, p. 114-120, 2004.

14. Farina D., Rainoldi A., "Compensation of the effect of sub-cutaneous tissue layers on surface EMG: A simulation study," Med Eng Phys, Vol 21, p. 487–496, 1999.

15. Fillion D., "Activité EMG au niveau du membre supérieur: étude à l′aide d′un fantôme," Master thesis, University of Montreal, 84 pages, 2006.

16. Frank E, "The zero-potential contour on a homogeneous conducting cylinder", Trans. IRE PGME, Vol 1, p. 27-37, 1953.

17. Fuchs M, Wischmann HA, Wagner M, "Generalized minimum norm least squares reconstruction algorithms", In: Skrandies W, editor. ISBET newsletter, no. 5. p. 8–11, 1994.

18. Gootzen T. H., Stegeman D. F., Van Oosterom A., "Finite limb dimensions and finite muscle length in a model for the generation of electromyographic signals", ELECTROEN CLIN NEUR, Vol 81, p. 152-162, 1991.

19. Grave de Peralta R, Gonzalez S, Lantz G, Michel CM, Landis T. "Noninvasive localization of electromagnetic epileptic activity. I. Method descriptions and simulations". Brain Topogr, Vol 14, p. 131–137, 2001.

20. Grave de Peralta Menendez R, Gonzalez Andino SL, "A critical analysis of linear inverse solutions". IEEE Trans Biomed Eng, Vol 45, p. 440–448, 1998.

21. Gross J, Kujala J, Hämäläinen M, Timmermann L, Schnitzler A, Salmelin R. "Dynamic imaging of coherent sources: studying neural interactions in the human brain". Proc Nat Acad Sci USA, Vol 98, p. 694–699, 2001.

22. Guyton A.C , Hall J.E, "*Text Book of medical physiology*". Elsevier Saunders, 2006, Edition11.

23. Hämäläinen MS, Ilmoniemi RJ, "Interpreting magnetic fields of the brain—minimum norm estimates". Med Biol Eng Comput, Vol 32, p. 35–42, 1994.

24. Hayes M.H, "*Statistical digital signal processing and modeling*". John Wiley & Sons, 1996.

25. Haykin S, "Neural networks and learning machines", Pearson, 2008.

26. Heringa A, Stegeman D.F, Uijen, Gerard J. H., De Weerd, J.P.C.," Solution Methods of Electrical Field Problems in Physiology", IEEE Trans, Vol 29, p. 34-42, 1982.

27. Jackson J.K, "Classical Electrodynamics", Wiley, New York, 1962.

28. Jesinger R.A, Stonick V.L, "Processing signals from surface electrode arrays for noninvasive 3Dmapping of muscle Activity", IEEE DSP Workshop Proc, p. 57–60, 1994.

29. Kuiken TA, Stoykov N.S, Popovic´ M, Lowery M, Taflove A, "Finite Element Modeling of Electromagnetic Signal Propagation in a Phantom Arm", IEEE Trans. Neural Systems and Rehabilitation Engineering, Vol 9, p. 346-354, 2001.

30. Lambin P, Troquet J, "Complete Calculation of the Electric Potential Produced b a Pair of Current Source and Sink Energizing a Circular Finite-Length Cylinder", J. Appl. Phys, Vol 54, p. 4174-4184, 1983.

31. Letbetter W.D., "*Influence of intramuscular nerve branching on motor unit organization in medial gastrocnemius muscle*". Anat.Rec., 1974, Vol 178, p. 402.

32. Liu AK, Dale AM, Belliveau JW. "Monte Carlo simulation studies of EEG and MEG localization accuracy". Hum Brain Mapp, Vol 16, p. 47–62, 2002.

33. Lowery M.M, Stoykov N.S, Dewald J.P.A, Kuiken T.A., "Volume Conduction in an Anatomically Based Surface EMG Model", IEEE Trans Biomed Eng., Vol. 51, p. 2138 – 2147, 2004.

34. Lowery M.M, Stoykov N.S, Taflove A, Kuiken T.A, " A multiple-layer finite-element model of the surface EMG signal ", IEEE Trans. Biomed. Eng., Vol 49, p. 446–454, 2002.

35. Marieb E.N, Wilhelm P.B, Mallatt J.B, "*Human anatomy*". Benjamin Cummings, 2010, Edition 6.

36. Merletti R., Parker P.A, "*Electromyography*". John Wiley & Sons, 2004, Edition 1.

37. Mesin L, Farina D, "A Model for Surface EMG Generation in Volume Conductors With Spherical Inhomogeneities", IEEE Trans Biomed Eng., Vol. 52, p. 1984-1993, 2005.

38. Michel C. M., Murray M. M., Lantz G., Gonzalez S., Spinelli L., Grave de Peralta R, "EEG source imaging", Clinical Neurophysiology, Vol 115, p. 2195–2222, 2004.

39. Miller-Larsson, A., "An analysis of extracellular single muscle fiber action potential field Modelling results", Biol Cybern, Vol 51, p. 271-284, 1985.

40. Nejat N, " Study on the actovation of the biceps brachii compartments in normal subjects", Master thesis, University of Montreal, 114 pages, 2012.

41. Nolty J, "*The Human Brain: An Introduction to its Functional Anatomy*". Mosby Inc, 2002.

42. Okada *R.H, "Potentials Produced by an Eccentric Current Dipole i*n a Finite-Length Circular Conducting Cylinder", IRE. Trans. Med. Electron, Vol 7, p. 14-19, 1956.

43. Pasqual-Marqui RD, Michel CM, Lehmann D. "Low resolution electromagnetic tomography: a new method to localize electrical activity in the brain". Int J Psychophysiol, Vol 18, p. 49–65, 1994.

44. Piotrkiewcz M., Miller-Larsson A., "A method of description of single muscle fibre action potential by an analytical function V(t,r)". Biological cybernetics, Vol 56, p. 237-245, 1987.

45. Plonsey R, "Action potential sources and their volume conductor fields", IEEE Trans BME, Vol 65, p. 601-611, 1977.

46. Randy L, "*Practical algorithm genetic*", John Wiley & Sons, 2004.

47. Rosenfalck, P., "Intra and extracellular fields of active nerve and muscle fibers: A physicomathematical analysis of different models," Acta Physiol Scand, Vol 321, p. 1–49, 1969.

48. Saitu K., Masuda T., Okada M. "Depth and intensity of equivalent current dipoles estimated through an inverse analysis of surface electromyograms using the image method", BMES, vol. 37, pp. 720-726, 1999.

49. Schmidt DM, George JS, Wood CC. "Bayesian inference applied to the electromagnetic inverse problem". Hum Brain Mapp, Vol 7, p. 195–212, 1999.

50. Schneider J, Silny S, Rau G, "Influence of tissue inhomogeneties on noninvasive muscle fiber conduction velocity measurements—Investigated by physical and numerical modeling", IEEE Trans. Biomed. Eng., Vol 38, p. 851–860, 1991.

51. Segal L., "*Neuromuscular compartments in the human biceps brachii muscle*". Neuroscience Letters, 1992, Vol 140, p. 98-102.

52. Segal L., Catlin, P. Krauss, E, Merick, K, Robilotto, J, "*Anatomical Partitioning of Three Human Forearm Muscles*". Cells Tissues Organs, 2002, Vol 170, p. 183-197.

53. Ter Haar Romeny B.M., Denier van der Gon J.J., Gielen C.C.A.M., "*Changes in recruitment order of motor units in the human biceps muscle*". Exp. Neurol., 1982, Vol 78, p. 360-368.

54. Ter Haar Romeny B.M., Denier van der Gon J.J., Gielen C.C.A.M., "*Relation between location of a motor unit in the human biceps brachii and its critical firing levels for different tasks*". Exp. Neurol., 1984, Vol 85, p. 631-650.

55. Uutela K, Hamalainen M, Salmelin R, "Global optimization in the localization of neuromagnetic sources". IEEE Trans Biomed Eng, Vol 45, p. 716–723, 1998.

56. Van den Doel K, Ascher U, Leitao A, "Multiple level sets for piecewise constant surface reconstruction in highly ill-posed problems", Journal of Scientific Computation, Vol 42, p. 44-66, 2010.

57. Van den Doel K, Ascher U, Pai D, "Computed myography: three dimensional reconstruction of motor functions from surface EMG data. Inverse Problems, Vol 24, 2008.

58. Vander A, Sherman J, Luciano D, "*Human Physiology, The Mechanisms of Body Function*". McGraw Hill, 2008, Edition 8.

59. Vogel C, "*Computational Methods for Inverse Problem*". Philadelphia: SIAM, 2002.

60. Weeks OI, English AW.," *Compartmentalization of the cat lateral gastrocnemius motor nucleus*". J Comp Neurol., 1985, Vol 235, p. 255-267.

61. Weeks OI, English AW., "*Cat triceps surae motor nuclei are topologically organized*". Erp Neurol., 1987, Vol 96, p. 163-167.

62. Wood S. M, Jarratt J. A, Barker A.T, Brown B. H, "Surface electromyography using electrode arrays: A study of motor neuron disease", Muscle Nerve, Vol. 24, pp. 223–230, 2001.

APPENDIX 1 – Using Matlab optimization toolbox with the GAI programs

1- Open MATLAB
2- At Current Directory, choose the path where the David's data are located and choose one of the available directories as Radiale_long for example.
3- In that directory, open **rad.m** to edit it
4- At line 42 delete 1:size (fichiers,1) and replace it, from the violet list appearing above by the number corresponding to the radial position of the dipole such as: 27:27 which correspond to the dipole positioned at 40 mm from the border of the tank and **s*ave the file.***
5- In the Command Windows, type **rad** to execute the program (wait for the return of >>) then

    type moy1'

6- In the Command Windows, choose the path where the GA file is stored
7- In the Command Windows, select the 16 values and copy them in the clipboard
8- Open *GAI1_new* file and for **RMS (line 10), deleted the values that are shown and make a copy command (to replace them by those last put in the clipboard). Save the file.**
9- In the Command Windows, type: *gatool*
10- The following window will appear:
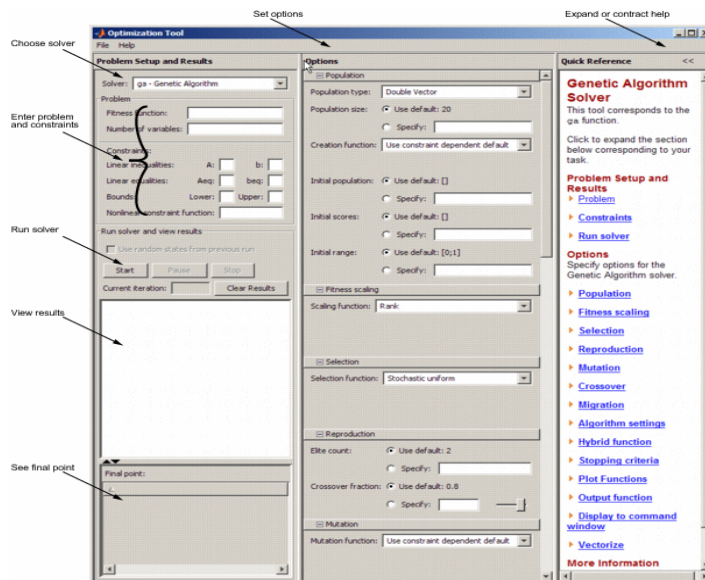
and near the top of the left panel side at the 3rd entry for the Fitness function enter:

@GAI1_new

11- At Number of valuables, put: 3 (for radius, angle and intensity)
12- At Bounds: go to Lower: and enter *[0 0 0]* and for Upper: enter *[8.5 6.28 10]* (limits of radius, angle and intensity)
13- Go on the right panel, near the bottom, go to the section **Stopping criteria:** and put *1e-9*

Stopping criteria	
Generations:	100
Time limit:	Inf
Fitness limit:	-Inf
Stall generations:	50
Stall time limit:	20
Function tolerance:	1e-006
Nonlinear constraint tolerance:	1e-006
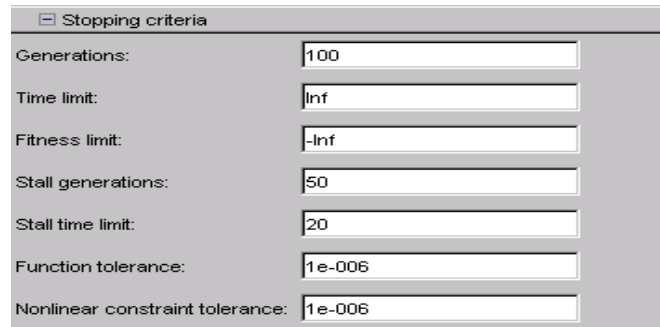
14- In the Plot functions section, tick *Best individual*
15- Then on *Start* button at the left side.

16- When the 100 GA iterations are finished, go on the top left panel and at **Solver:** use the top down menu and choose: *fmincon and push on the YES button in the pop-up window.*

Optimization Tool
File   Help

Problem Setup and Results

Solver: fmincon - Constrained nonlinear minimization
Algorithm: Trust region reflective
Problem
  Objective function:
  Derivatives: Approximated by solver
  Start point:
Constraints:
  Linear inequalities: A: b:
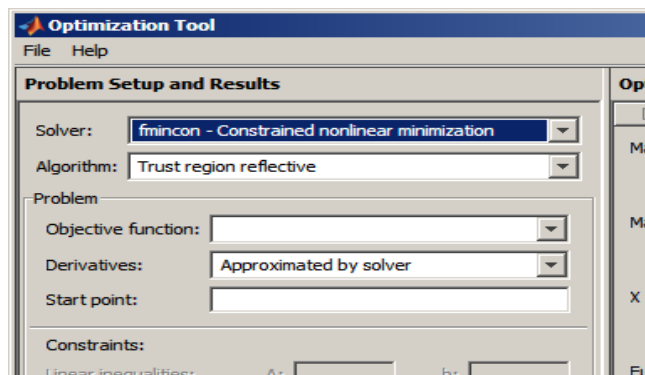
At the bottom of the left panel, click on **the Final point:** values obtained with GA and make a Control+C to copy those values. Then go upward to **Start point:** to copy them.

17- For Objective function: as for GA, type: @GAI1_new

18- For Plot functions: (bottom on the right panel), click ***Current point.***
19- Push the **Start** button on the left panel.

In the **Solver**, *fmincon* was used because it uses the conjugated gradient approach and it is also possible to put restrictions in the search domain and an initial search point can be in it to guide the search. For the global minimum, values of the dipole characteristics appear at the bottom of the left panel with the angular position expressed in radians.

APPENDIX 2 – Results for simulated signals (3 dipoles)

Inverse model results when applied to experimentally obtained results (displayed in Fig. 4.6) to which Gaussian white noise was added at 3 S/N ratios.

	#1 Fixed dipole			Moving dipole			#2 Fixed dipole		
	10			10			10		
	rho (mm)	phi (°)	I (rel.)	rho (mm)	phi (°)	I (rel.)	rho (mm)	phi (°)	I (rel.)
inverse	8.34	67.6	1	8.55	180.4	0.9	8.49	288.2	1
diff (%)	-16.6	0.15	0	-14.5	0.22	-10	-15.1	0.07	0
S/N=30db	8.31	67.6	1	8.52	180.5	0.9	8.49	288.3	1
diff (%)	-16.9	0.15	0	-14.8	0.28	-10	-15.1	0.1	0
S/N=20db	8.21	67.6	1	8.49	180.5	0.9	8.5	288.3	1
diff (%)	-17.9	0.15	0	-15.1	0.28	-10	-15	0.1	0
S/N=10db	8.14	67.6	0.8	8.48	180.5	0.9	8.5	288.3	1
diff (%)	-18.6	0.15	-20	-15.2	0.28	-10	-15	0.1	0
	10			30			10		
	rho	phi	i	rho	phi	i	rho	phi	i
inverse	8.23	67.6	0.9	30.83	180.4	1	8.47	288.3	1
diff (%)	-17.7	0.15	-10	2.77	0.22	0	-15.3	0.10	0
S/N=30db	8.2	67.6	0.9	31.52	179.9	1	8.47	288.2	1
diff (%)	-18	0.15	-10	5.07	-0.06	0	-15.3	0.07	0
S/N=20db	8.2	67.6	0.9	31.62	179.6	1	8.47	288.2	0.9
diff (%)	-18	0.15	-10	5.4	-0.22	0	-15.3	0.07	-10
S/N=10db	8.21	67.6	1	31.68	179.9	1	8.47	288.2	0.8
diff (%)	-17.9	0.15	0	5.6	-0.06	0	-15.3	0.07	-20
	10			50			10		
	rho	phi	i	rho	phi	i	rho	phi	i
inverse	8.25	67.6	1	48.02	178.8	0.9	8.5	288.3	1
diff (%)	-17.5	0.15	0	-3.96	-0.67	-10	-15	0.1	0
S/N=30db	8.25	67.6	1	47.89	178.7	0.9	8.48	287.6	1
diff (%)	-17.5	0.15	0	-4.22	-0.72	-10	-15.2	-0.14	0
S/N=20db	8.24	67.6	1	47.22	178.8	0.9	8.5	287.6	1
diff (%)	-17.6	0.15	0	-5.56	-0.67	-10	-15	-0.14	0
S/N=10db	8.25	67.6	1	43.27	178.8	1.1	8.49	287.1	1
diff (%)	-17.5	0.15	0	-13.46	-0.67	10	-15.1	-0.31	0
	10			70			10		
	rho	phi	i	rho	phi	i	rho	phi	i
inverse	8.19	67.6	1	63.06	172.7	1	8.48	288.2	1
diff (%)	-18.1	0.15	0	-9.91	-4.06	0	-15.2	0.07	0
S/N=30db	8.19	67.6	1	62.8	171.9	1	8.5	288.2	1
diff (%)	-18.1	0.15	0	-10.29	-4.5	0	-15	0.07	0
S/N=20db	8.12	67.6	1	62.45	171.9	1	8.5	288.2	1
diff (%)	-18.8	0.15	0	-10.79	-4.5	0	-15	0.07	0
S/N=10db	8.12	67.6	1	59.39	171.3	1	8.5	288.2	1
diff (%)	-18.8	0.15	0	-15.16	-4.83	0	-15	0.07	0

APPENDIX 3 − ELABORATED MATLAB PROGRAMS

Program (main.m) used for the simulation of 5000 SFAPs

```matlab
% Created the Extracellular Single Mucle Fibre Action Potential
% and define the position of zone of acivity

% Pooya Maghoul 2011-08-24
%-------------------------
clear;
clc;
%--------------Created one SFAP----------------------------------------
a=0.02;
r=0.02;
%z=10;
Amp=rand(1,20001);
Delay1=10005*rand(1,20001);
Delay2=10005*rand(1,20001);
Delay3=10005*rand(1,20001);
Delay1(1,1)=500;
Delay2(1,1)=500;
Delay3(1,1)=500;

    i=0;
  for z=0:0.1:1000
    i=i+1;
    z1=z-Delay1(1,1);
    z2=z-Delay2(1,1);
    z3=z-Delay3(1,1);
    F1 = @(s)(s.*(6-6*s+s.^2)./sqrt((5*r^2+(z1-s).^2))).*exp(-s);
    F2 = @(s)(s.*(6-6*s+s.^2)./sqrt((5*r^2+(z2-s).^2))).*exp(-s);
    F3 = @(s)(s.*(6-6*s+s.^2)./sqrt((5*r^2+(z3-s).^2))).*exp(-s);
    QQ1 = -24*a^2*Amp(1,1)*quad(F1,0,250);
    QQ2 = -24*a^2*Amp(1,1)*quad(F2,0,250);
    QQ3 = -24*a^2*Amp(1,1)*quad(F3,0,250);
    t(i)=i/1;
    Q1(i)=QQ1;
    Q2(i)=QQ2;
    Q3(i)=QQ3;
  end
  figure(1)
    hold on
    plot(t,10^(-1)*Q1)
    grid on

%------------Add the various SFAP1----------------------------------------
N=5000;
 Cu11=10^(3)*Q1;
 Cu1 = repmat(Cu11,N,1);
 %Cu= Cu1;
 for d=2:N
     dd=round(Delay1(1,d));
```

```matlab
      Cu1(d,:)=Amp(1,d)*circshift(Cu1(d,:),[0,dd]);
 end
%
     SS1=sum(Cu1,1);
     N1=size(SS1,2);
     SS1=SS1(1:N1);
     %-----------Add the various SFAP2----------------------------------------
N=5000;
 Cu22=10^(3)*Q2;
 Cu2 = repmat(Cu22,N,1);
 %Cu= Cu1;
 for d=2:N
     dd=round(Delay2(1,d));
      Cu2(d,:)=Amp(1,d)*circshift(Cu2(d,:),[0,dd]);
 end
%
     SS2=sum(Cu2,1);
     N1=size(SS2,2);
     SS2=SS2(1:N1);
     %------------Add the various SFAP3---------------------------------------
N=5000;
 Cu33=10^(3)*Q3;
 Cu3 = repmat(Cu33,N,1);
 %Cu= Cu1;
 for d=2:N
     dd=round(Delay3(1,d));
      Cu3(d,:)=Amp(1,d)*circshift(Cu3(d,:),[0,dd]);
 end
%
     SS3=sum(Cu3,1);
     N1=size(SS3,2);
     SS3=SS3(1:N1);
          %-----------Add the various SFAP4--------------------------------
------
N=5000;
 Cu33=10^(3)*Q3;
 Cu4 = repmat(Cu33,N,1);
 %Cu= Cu1;
 for d=2:N
     dd=round(Delay3(1,d));
      Cu4(d,:)=Amp(1,d)*circshift(Cu4(d,:),[0,dd]);
 end
%
     SS4=sum(Cu4,1);
     N1=size(SS4,2);
     SS4=SS4(1:N1);
%-----Plot the EMG signal and RMS value------------------------------
   figure(2)

y = detrend(SS1);
yrms1=sqrt(sum((y).^2)/size(SS1,2));

yrmst(i)=yrms1;
```

```matlab
plot(y,'color',[ 0 0 1]),title([' ch ' num2str(i),', nn-30-s-20,
yrms=',num2str(yrms1),' (µV)']);
hold on
%------Dipole1------------------
rho1=5;
phi1 = pi/4%+pi/16;%*pi/6;%+2*pi/18;
teta1=0;
ints1=2;
%------Dipole2-----------------
rho2=5.5;
phi2 =3*pi/4%+pi/16;%+pi/8;
teta2=2*pi/2;
ints2=1;
%-----Dipole3------------------
rho3=4.5;
phi3 = 5*pi/4%+pi/16;%+pi/8;
teta3=pi/4;
ints3=4;
%------Dipole4------------------
rho4=7;
phi4 = 7*pi/4;%+pi/8;
teta4=pi/3;
ints4=0;
%-----MAV and signals on the electrodes------------------
[moy1,electrodes]=forward_ff_SFAP1(rho1,rho2,rho3,rho4,phi1,phi2,phi3,phi4,int
s1,ints2,ints3,ints4,Cu1,Cu2,Cu3,Cu4);

hold on
figure(3)
plot(abs(moy1),'r')
grid on
hold on
stem(abs(moy1),'r')
%----------Frequency analysis---------------------------

 figure(4)
  Fs=2000;
  L=10000;
  bb=0;
for w=1:1:16
    bb=bb+1;
    NFFT = 2^nextpow2(L); % Next power of 2 from length of y
      Y = fft(electrodes(w,:),NFFT)/L;
      z=smooth(Y,7);
      %z=Y;
     for j=1:200
      z=smooth(z,7);
     end
%plot(f,2*abs(z(1:NFFT/2+1))),title([' fft, of ch ' num2str(i),',nn-30-s-20,
yrms=',num2str(yrms1),' (µV)']);
   f = Fs/2*linspace(0,1,NFFT/2+1);
   plot(f,2*abs(z(1:NFFT/2+1)),'k'),title([' fft, of ch ' num2str(i),',nn-30-
s-20,    yrms=',num2str(yrms1),' (µV)']);
   %subplot(3,1,bb),plot(f,2*abs(Y(1:NFFT/2+1)),'k');
```

```matlab
hold on
end

figure(5)
for w=1:16
    y=  electrodes(w,:);
    %[y1,omega]=pmusic(y,6);
    [y1,omega]=pwelch(y,128,120,[],Fs,'onesided')
    %pmusic(y,4)
    y2(:,w)=y1;
    y3(w)=y2(5,w);
    hold on
end
plot(y3)
hold on
plot(y2)
hold all
```

Program (`forward_ff_SFAP1.m`) used for the simulation of Forward problem with main.m program.

```matlab
function [moy,out]
=forward_ff_SFAP1(rrhoa,rrhob,rrhoc,rrhod,pphia,pphib,pphic,pphid,intsa,intsb,
intsc,intsd,input1,input2,input3,input4)

mLim = 20;
nLim = 100;
z0 = 3.3;          % z'
z=4.85;
L = 9;             % longueur
R = 85*10^(-1);    % rayon
x = (1 : nLim) * pi / L;
xx = x(ones(mLim + 1, 1), :);
m = repmat((0 : mLim)', 1, nLim);
n = repmat(1 : nLim, mLim + 1, 1);
%B1=(besseli(m, xx * rrho));
B2=(besseli(m - 1, xx * R) + besseli(m + 1, xx * R));

for j=1:16
   phi=(j-1)*pi/8;
       Va = -sum(sin(x * z0) .* cos(x * z) .* sum(cos(m * (phi -
pphia)).*(besseli(m, xx * rrhoa))./B2));
       Vb = -sum(sin(x * z0) .* cos(x * z) .* sum(cos(m * (phi -
pphib)).*(besseli(m, xx * rrhob))./B2));
       Vc = -sum(sin(x * z0) .* cos(x * z) .* sum(cos(m * (phi -
pphic)).*(besseli(m, xx * rrhoc))./B2));
       Vd = -sum(sin(x * z0) .* cos(x * z) .* sum(cos(m * (phi -
pphid)).*(besseli(m, xx * rrhod))./B2));
%hold on
   V1(j)=Va;
   V2(j)=Vb;
   V3(j)=Vc;
   V4(j)=Vd;

end

Vf1=3.8*intsa/2*V1./3.9507;
Vf2=3.8*intsb/2*V2./3.9507;
Vf3=3.8*intsc/2*V3./3.9507;
Vf4=3.8*intsd/2*V4./3.9507;

%t=0:0.001:2*pi;

for d=1:16
  y1=sum(Vf1(d)*input1,1);
  y2=sum(Vf2(d)*input2,1);
  y3=sum(Vf3(d)*input3,1);
  y4=sum(Vf4(d)*input4,1);
  yf(d,:)=(y1+y2+y3+y4);
  %yf(d,:) = awgn(yf1(d,:),1000,'measured');     % Sinusoids plus noise
  out(d,:)=yf(d,:);
```

```matlab
%  moy(d) = mean(abs(yf(d,:)));
%   yf(d,:) = detrend(yf1(d,:));
%    yrms1=sqrt(sum((yf(d,:)).^2)/size(yf(d,:),2));
%    moy(d)=yrms1;
end




Fs = 2000;                         % Sampling frequency
T = 1/Fs;                          % Sample time
L = 10000; % Length of signal
for d=1:16
y(d,:) = yf(d,:);
% plot(Fs*t(1:50),y(d,1:50))
% title('Signal Corrupted with Zero-Mean Random Noise')
% xlabel('time (milliseconds)')
NFFT = 2^nextpow2(L); % Next power of 2 from length of y
Y = fft(y(d,:),NFFT)/L;
z=smooth(Y,7);
  for j=1:200
    z=smooth(z,7);
  end
  z1(d,:)=z;
f = Fs/2*linspace(0,1,NFFT/2+1);
% Plot single-sided amplitude spectrum.
% plot(f,2*abs(z(1:NFFT/2+1)))
%  title('Single-Sided Amplitude Spectrum of y(t)')
%  xlabel('Frequency (Hz)')
%  ylabel('|Y(f)|')
end
moy=z1(:,330);
```

PROGRAM (`GAI3_surface_elec_new1`.m) USED WITH THE TANK DATA

```
%Aurthur:Pooya Maghoul 2012/09/27
%Solve the Inverse problem for David's experminetal data
% when electrode supposed 10mm diameter

function GAI=GAI3_surface_elec_new1(I)
%----Input definition
rho1=I(1);
rho2=I(2);
rho3=I(3);
phi1=I(4);
phi2=I(5);
phi3=I(6);
ints1=I(7);
ints2=I(8);
ints3=I(9);

D=1;  % diameter of electrode
%---The Value of RMS
RMS =  [  -0.0037 + 0.0199i
   -0.0035 + 0.0201i
   -0.0035 + 0.0218i
   -0.0049 + 0.0243i
   -0.0037 + 0.0287i
   -0.0036 + 0.0331i
   -0.0035 + 0.0366i
   -0.0036 + 0.0407i
   -0.0036 + 0.0403i
   -0.0035 + 0.0396i
   -0.0036 + 0.0359i
   -0.0039 + 0.0327i
   -0.0037 + 0.0282i
   -0.0081 + 0.0256i
    0.0036 - 0.0222i
    0.0031 - 0.0204i
   -0.0181 - 0.0279i
   -0.0123 - 0.0202i
   -0.0098 - 0.0167i
   -0.0080 - 0.0162i
   -0.0086 - 0.0148i
   -0.0087 - 0.0149i
   -0.0093 - 0.0156i
   -0.0107 - 0.0175i
   -0.0124 - 0.0195i
   -0.0155 - 0.0230i
   -0.0203 - 0.0284i
   -0.0306 - 0.0401i
   -0.0599 - 0.0732i
   -0.5193 - 0.6646i
    0.0935 + 0.1166i
    0.0335 + 0.0430i
```

```
       0.0021 - 0.0164i
       0.0022 - 0.0246i
       0.0034 - 0.0532i
       0.0716 - 0.8028i
       0.0047 - 0.0758i
       0.0020 - 0.0326i
       0.0018 - 0.0217i
       0.0016 - 0.0168i
       0.0016 - 0.0131i
       0.0014 - 0.0115i
       0.0014 - 0.0100i
       0.0014 - 0.0093i
       0.0011 - 0.0088i
       0.0016 - 0.0089i
      -0.0013 + 0.0100i
      -0.0012 + 0.0123i]';
%--------------------
 % Solve he inverse problem
mLim = 20;
nLim = 100;
z0 = 4.4;          % z' location of dipole in z axis in cm
z=5.2;             % location of electrode in z axis in cm
L = 10.4;              % height of water tank in cm
R = 85*10^(-1);    % radius of tank in cm
x = (1 : nLim) * pi / L;
xx = x(ones(mLim + 1, 1), :);
m = repmat((0 : mLim)', 1, nLim);  % order of bessle function
n = repmat(1 : nLim, mLim + 1, 1); % order ofbessel function
%B1=(besseli(m, xx * rrho));
B2=(besseli(m - 1, xx * R) + besseli(m + 1, xx * R)); %bessel function
for i=1:16
    phi=(i-1)*pi/8;%-pi/8;   % angle of electrodes

    Va = -sum(sin(x * z0) .* cos(x * z) .* sum(cos(m * (phi -
phi1)).*(besseli(m, xx * (rho1+0.5*ceil(rho1/8.5))))./(B2)));  % calculating
the poytential in each elevtrode
    Vb = -sum(sin(x * z0) .* cos(x * z) .* sum(cos(m * (phi -
phi2)).*(besseli(m, xx * (rho2+0.5*ceil(rho2/8.5))))./(B2)));
    Vc = -sum(sin(x * z0) .* cos(x * z) .* sum(cos(m * (phi -
phi3)).*(besseli(m, xx * (rho3+0.5*ceil(rho3/8.5))))./(B2)));
    %hold on
    V3(i)=Va;  % put potentials in vector
    V4(i)=Vb;
    V5(i)=Vc;

end

Vf1=3.5*V3/3.95+0.04; % normalize the signal with the bias value.
Vf2=3.5*V4/3.95+0.04;
Vf3=3.5*V5/3.95+0.04;
Fs = 2000;                        % Sampling frequency
T = 1/Fs;                         % Sample time
L = 10000; % Length of signal
%t=0:0.001:2*pi;
```

```matlab
t = (0:L-1)*T;
for d=1:16
    y1=5*exp(9*(-1+ints1))*(1-
ints1)*(ints1+0.075)^2*Vf1(d)*sin(2*pi*22.1*t)/6; % calculating the potental
after applying the surface of electrode and dimension of dipole
    y2=5*exp(9*(-1+ints2))*(1-ints2)*(ints2+0.075)^2*Vf2(d)*sin(2*pi*32*t)/6;
    y3=5*exp(9*(-1+ints3))*(1-
ints3)*(ints3+0.075)^2*Vf3(d)*sin(2*pi*44.5*t)/6;
    yf1(:,d)=y1+y2+y3;
    y11(:,d)=y1;
    y22(:,d)=y2;
    %moy2(d) = mean(abs(yf1));   % calculating the RMS value
end
%---Power spectrum analysis-------

y=[];
Y1=[];
Y=[];
D=1; % Diamter of electrode in cm
c=300; % Conductivity velocity in cm/s
NFFT = 2^nextpow2(L);
f = Fs/2*linspace(0,1,NFFT/2+1);
f1=pi*f*D/c;
ELE=2*besselj(1,f1)./f1;
%-----------------------------

for d=1:16
% y11(:,d) = y11(:,d);
% y22(:,d) = y2(:,d);
Y11 = fft(yf1(:,d),NFFT)/L;
Y1(:,d)=Y11(1:NFFT/2+1).*ELE';
% Y22 = fft(y22(:,d),NFFT)/L;
% Y2(:,d)=Y22(1:NFFT/2+1).*ELE';
end
moy2=Y1(183,:);
moy3=Y1(263,:);
moy4=Y1(366,:);
%moy2=[moy3 moy4]
%---Minimum the cost function
GAI1=norm(RMS(1:16)-moy2);
GAI2=norm(RMS(17:32)-moy3);
GAI3=norm(RMS(33:48)-moy4);
GAI=norm([GAI1 GAI2 GAI3]);
```

PROGRAM (`GAI3_Real_model`.m) USED WITH THE EMG DATA

```matlab
%Aurthor:Pooya Maghoul 2012/09/27

function GAI=GAI3_Real_model(I)
%----Input definition
rho1=I(1);
rho2=I(2);
rho3=I(3);
phi1=I(4);
phi2=I(5);
phi3=I(6);
ints1=I(7);
ints2=I(8);
ints3=I(9);
teta1=I(10);
teta2=I(11);
teta3=I(12);


D=1;  % diameter of electrode
%---The Value of RMS %25mm
RMS0 = [0.13 0.34 0.52 0.72 0.82 0.87 1.07 1.41 1.31 0.99]'*1.0e-006;
 RMS1=RMS0(10:-1:1,1);
   RMS=RMS1';


%--------------------
 % Solve he inverse problem
mLim = 20;
nLim = 100;
z0 = 10.2;        % z'
z=11;
L = 17;           % longueur
R = 43*10^(-1);   % rayon
x = (1 : nLim) * pi / L;
xx = x(ones(mLim + 1, 1), :);
m = repmat((0 : mLim)', 1, nLim);  % order of bessle function
n = repmat(1 : nLim, mLim + 1, 1); % order ofbessel function
%B1=(bessel(m, xx * rrho));
B2=(besseli(m - 1, xx * R) + besseli(m + 1, xx * R)); %bessel function
for i=1:10
    phi=(i-1)*0.2715+0.3491;%-pi/8;


    Va = -sum(sin(x * z0) .* cos(x * z) .* sum(cos(m * (phi -
phi1)).*(besseli(m, xx * (rho1+0.5*ceil(rho1/4.2))))./(B2))); % calculating
the poytential in each elevtrode
    Vb = -sum(sin(x * z0) .* cos(x * z) .* sum(cos(m * (phi -
phi2)).*(besseli(m, xx * (rho2+0.5*ceil(rho2/4.2))))./(B2)));
    Vc = -sum(sin(x * z0) .* cos(x * z) .* sum(cos(m * (phi -
phi3)).*(besseli(m, xx * (rho3+0.5*ceil(rho3/4.2))))./(B2)));
    %hold on
    V1(i)=Va;  % put potentials in vector
    V2(i)=Vb;
    V3(i)=Vc;
 end
```

```matlab
Vf1=(3.5*V1/3.95+0.04)/3.5/200; % normalize the signal with the bias value.
Vf2=(3.5*V2/3.95+0.04)/3.5/200;
Vf3=(3.5*V3/3.95+0.04)/3.5/200;
Fs = 2000;                      % Sampling frequency
T = 1/Fs;                       % Sample time
L = 10000; % Length of signal
%t=0:0.001:2*pi;
t = (0:L-1)*T;
for d=1:10
    %y1=4*(1-ints1)*(ints1)^2*Vf1(d)*sin(2*pi*32*t+teta1); % calculating the
potental after applying the surface of electrode and dimension of dipole
    y1=5*exp(9*(-1+ints1))*(ints1+0.075)^2*Vf1(d)*sin(2*pi*44.5*t+teta1)/6;
    y2=5*exp(9*(-1+ints2))*(ints2+0.075)^2*Vf2(d)*sin(2*pi*44.5*t+teta2)/6;
    y3=5*exp(9*(-1+ints3))*(ints3+0.075)^2*Vf3(d)*sin(2*pi*44.5*t+teta3)/6;
    yf1(:,d)=y1+y2+y3;
    %moy2(d) = mean(abs(yf1));    % calculating the RMS value
end
%---Power spectrum analysis-------

y=[];
Y1=[];
Y=[];
D=1; % Diamter of electrode in cm
c=300; % Conductivity velocity in cm/s
NFFT = 2^nextpow2(L);
f = Fs/2*linspace(0,1,NFFT/2+1);
f1=pi*f*D/c;
ELE=2*besselj(1,f1)./f1;
%----------------------------

for d=1:10
%Y11 = fft(yf1(:,d),NFFT)/L;
[Y11,omega]=pwelch(y,[],[],length(y),Fs,'onesided');
%Y1(:,d)=Y11(1:NFFT/2+1).*ELE';
Y1(:,d)=Y11;
end
%moy2=Y1(183,:);
%moy3=Y1(263,:);
moy2=Y1(366,:);
%---Minimum the cost function
GAI=norm(RMS-moy2);
```

APPENDIX 4 – Cylinder model with three concentric layers

For a more realistic model than a single cylinder to model the upper limb, the volume conductor can be considered to be made of 3 concentric layers: one for the skin, another for the fat, and the third one for muscle tissue (Block et al [1]. The presence of the humerus bone can also be considered. A transverse section and a longitudinal view are illustrated in Fig A.1A and B. In such a model, the current sources are put within the muscular cylinder and the potential distribution at the skin level is obtained by solving the Poisson equation with boundary conditions imposed by the humerus bone and the fat and skin layers.

The muscle layer was supposed anisotropic and also the fat and skin layers are assumed isotropic. Block et al solved equation A1 in cylindrical coordinate which gave (eqn 3.71, p.111 of Jackson [27]):

$$\frac{d^2V}{d\rho^2} + \frac{1}{\rho}\frac{dV}{d\rho} + \frac{1}{\rho^2}\frac{d^2V}{d\phi^2} + \frac{d^2V}{dz^2} = -\frac{I}{\sigma} \qquad (A1)$$
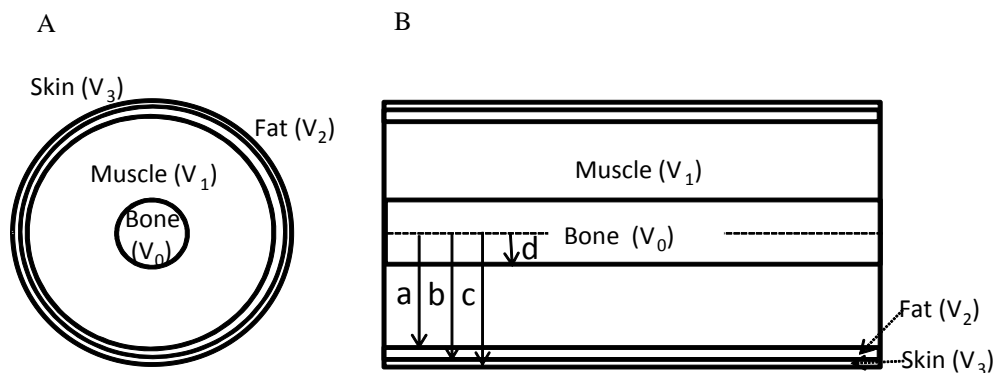
Fig A.1 A. Transverse upper arm cylindrical model with three concentric layers representing the muscle tissue, the fat and skin layers. B. Longitudinal view where *a*= radius of muscle tissue; b=radius of muscle tissue plus fat layer; *c and d:* radius of muscle plus fat and skin layers; d= radius of the humerus bone. The humerus bone (b) is represented by the circle in the middle.

To solve (A1), Block et al [1] used the separation variable method where a goal function (*V*) is included for several independent functions and that each function is created from independent

variables. They considered 3 independent variables which are the variable of cylindrical coordinate:

$$V(\rho,\phi,z)=R(\rho)\,\Phi(\phi)Z(z) \qquad\qquad (A2)$$

is used in (A1) within the boundary conditions of Dirichlet and Neumann when applied between mediums 0, 1, 2 and 3:

$$1)\ V_0|_{\rho=d} = V_1|_{\rho=d} = 0 \qquad 2)\ \sigma_0 \frac{\partial V_0}{\partial \rho}\Big|_{\rho=d} = \sigma_{1_r} \frac{\partial V_1}{\partial \rho}\Big|_{\rho=d} = 0$$

$$3)\ V_1|_{\rho=a} = V_2|_{\rho=a} \qquad 4)\ \sigma_{1_r} \frac{\partial V_1}{\partial \rho}\Big|_{\rho=a} = \sigma_2 \frac{\partial V_2}{\partial \rho}\Big|_{\rho=a}$$

$$5)\ V_2|_{\rho=b} = V_3|_{\rho=b} \qquad 6)\ \sigma_2 \frac{\partial V_2}{\partial \rho}\Big|_{\rho=b} = \sigma_3 \frac{\partial V_3}{\partial \rho}\Big|_{\rho=b}$$

$$7)\ \sigma_3 \frac{\partial V_3}{\partial \rho}\Big|_{\rho=c} = 0 \qquad\qquad (A.3)$$

where σ_0, σ_2, σ_3 represented the conductivities of the isotropic bone, fat and skin and σ_{1_r} and σ_{1_z} are the muscle anisotropic conductivities in the radial and longitudinal directions. When (A.1) is solved with the boundary conditions of (A.3) they obtained:

$$V_0 = 0; \ V_1 = \frac{I.d}{2\,\sigma_{1_r}} K_0\left((r-d)\sqrt{\frac{\sigma_{1_z}}{\sigma_{1_r}}}\right) + \sum_{n=-\infty}^{\infty} e^{-in\phi}[A_n(k)I_n(\rho\sqrt{\frac{\sigma_{1_z}}{\sigma_{1_r}}})]$$

$$V_2 = \frac{I.d}{2\,\sigma_2} K_0(r) + \sum_{n=-\infty}^{\infty} e^{-in\phi}[C_n(k)I_n(\rho) + D_n(k)K_n(\rho)]$$

$$V_3 = \frac{I.d}{2\,\sigma_3} K_0(r) + \sum_{n=-\infty}^{\infty} e^{-in\phi}[E_n(k)I_n(\rho) + F_n(k)K_n(\rho)] \qquad (A.4)$$

Where V_1 is the potential within muscle tissues (excluding the bone), V_2 the potential within the fat layer and V_3 within the skin thickness, in those equations, A_n, B_n, D_n, E_n and F_n are unknown but could be found with:

$$\begin{bmatrix} \dfrac{I_n(a_1)}{I_n(\rho_1)} & \dfrac{-I_n(a_2)}{I_n(\rho_2)} & \dfrac{-K_n(a_2)}{K_n(\rho_2)} & 0 & 0 \\[2mm] \dfrac{I'_n(a_1)}{I_n(\rho_1)} & \dfrac{-I'_n(a_2)}{I_n(\rho_2)} & \dfrac{-K'_n(a_2)}{K_n(\rho_2)} & 0 & 0 \\[2mm] 0 & \dfrac{I_n(b_2)}{I_n(\rho_2)} & \dfrac{K_n(b_2)}{K_n(\rho_2)} & \dfrac{-I_n(b_3)}{I_n(\rho_3)} & \dfrac{-K_n(b_3)}{K_n(\rho_3)} \\[2mm] 0 & \dfrac{I'_n(b_2)}{I_n(\rho_2)} & \dfrac{K'_n(b_2)}{K_n(\rho_2)} & \dfrac{-I'_n(b_3)}{I_n(\rho_3)} & \dfrac{-K'_n(b_3)}{K_n(\rho_3)} \\[2mm] 0 & 0 & 0 & \dfrac{I'_n(c_3)}{I_n(\rho_3)} & \dfrac{K'_n(c_3)}{K_n(\rho_3)} \end{bmatrix} \begin{bmatrix} A_n(k)I_n(\rho_1) \\ C_n(k)I_n(\rho_2) \\ D_n(k)K_n(\rho_2) \\ E_n(k)I_n(\rho_3) \\ F_n(k)K_n(\rho_3) \end{bmatrix} =$$

$$\frac{I.d}{2}\begin{bmatrix} \dfrac{I_n(R_2)K_n(a_2)}{\sigma_2} - \dfrac{I_n(R_1-d)K_n(a_1)}{\sigma_{1r}} \\[3mm] I_n(R_2)K'_n(a_2) - \sqrt{\dfrac{\sigma_{1z}}{\sigma_{1r}}}\,I_n(R_1-d)K'_n(a_1) \\[3mm] \dfrac{I_n(R_3)K_n(b_3)}{\sigma_3} - \dfrac{I_n(R_2)K_n(b_2)}{\sigma_2} \\[3mm] I_n(R_3)K'_n(b_3) - I_n(R_2)K'_n(b_2) \\[2mm] -I_n(R_3)K'_n(c_3) \end{bmatrix} \qquad (A.5)$$

where I and K are the modified Bessel Functions of the first and second kind and n is the order of them. Morover I' and K' are the derivatives of modified Bessel functions.

APPENDIX 5 – Illustration of the processing steps for a simple situation

Using the GA and NCG algorithms of Matlab, here is a simple example of their application to solve the inverse problem. The experimental situation to be analyzed consisted in a dipole fed with a sinusoidal current placed at a known position within a tank filled with a saline solution.
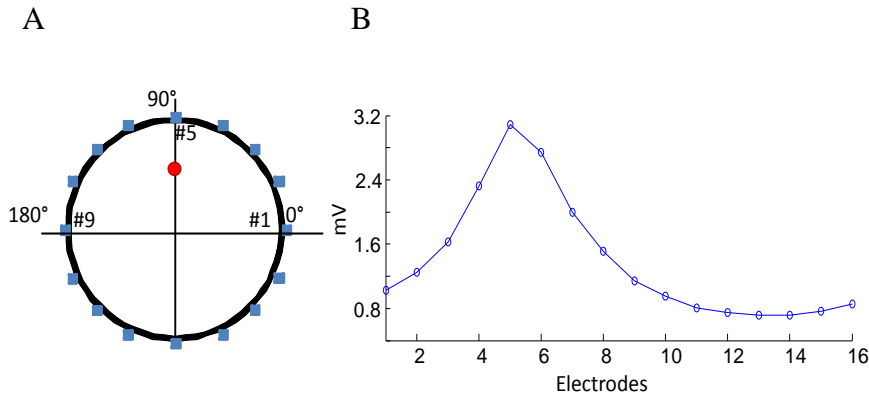
Fig. A2: a dipole (●) is placed at 90° and at 45 mm from electrode #5 B: signals recorded at the 16 electrodes circling the tank.

The Welch's estimate of the simulated signal (Chapter 3, eqn 3.22) at each of the 16 electrodes is compared to the experimentaly recorded signals (eqn 3.23). To identify the number of dipoles to be considered, the number of peaks in the distribution of the RMS values around the tank was used. In Fig A.2B, only one peak is detected and the presence of a single dipole was thus assumed. To minimize that cost function, the GA algorithm is first used. Twenty chromosomes were created to code the radius where the dipole is placed (steps of 0.66 mm), the angle (steps of 0.70°) and 16 steps for the relative intensity. After 100 iterations and a minimum error of $48*10^{-7}$, a dipole location at 44.2 mm, 95.9° and 1.1 as intensity was found. To illustrate the changes in the dipole position at each 10th iterations are shown in Table A.1A.

To find what would be the best results obtained with GA, no limitation was put either on the number of iterations or on the computing time. The algorithm stopped at the 173th iterations (error of $42*10^{-7}$) and gave the following dipole position: at 42.24 mm of radius, 96.6° of angular

position and with an 1.1 intensity. The changes in the dipole position at each 20th iteration is shown in Table A.1B

Table A1 Position and intensity (arbitrary units) of the dipole at different GA iterations. A. For 100 iterations (in each 10th iteration B. For 173 iterations (in each 20th iteration)

A

Iteration	Inverse		
I	ρ(mm)	φ(°)	I
1	6.66	53.91	1.7
10	26.42	96.64	1.5
20	36.37	96.64	1.5
30	41.64	98.02	1.2
40	42.25	96.67	1.2
50	42.93	95.93	1.2
60	43.55	95.98	1.1
70	44.26	95.61	1.1
80	44.26	96.61	1.1
90	44.25	95.98	1.1
100	44.25	95.98	1.1

B

Iteration	Inverse		
I	ρ(mm)	φ(°)	I
1	6.66	53.91	1.7
10	-	-	-
20	36.96	98.02	1.5
30	-	-	-
40	38.94	97.45	1.4
50	-	-	-
60	40.70	95.73	1.3
70	-	-	-
80	41.82	95.73	1.2
90	-	-	-
100	42.35	96.30	1.2
120	43.60	96.30	1.2
140	42.90	96.13	1.1
160	42.32	96.60	1.1
173	42.24	96.60	1.1

To check the robustness of the GA algorithm, the presence of 2 and 3 dipoles were considered to be present in the tank. With 2 dipoles and after 143 iterations (error of $51*10^{-7}$), it can be seen in Table A2 that the second dipole can be ignored due to its very weak intensity while the characteristics of the first are almost the same as those observed at the bottom of Table 4.3A. With 3 dipoles and after 232 iterations (error of $64*10^{-7}$), there is still only one predominant dipole due to its large intensity vs those of the 2 other dipoles (Table A.2B). Its position along the radius ρ is quite similar to the 2-dipoles condition while φ and I values are mose rensible to the addition of the third dipole.

Table A2. Inverse problem results when 2 (A) or 3 (B) dipoles are considered to be present in the tank Intensity I is in arbitrary units. When a dipole intensity is < 0.1, a zero is presented in the table.

A			B		
Inverse (two dipoles)			Inverse (three dipoles)		
ρ(mm)	φ(°)	I	ρ(mm)	φ(°)	I
42.78	96.07	1.1	43.27	103.18	0.9
26.81	117.52°	0	61.41	76.81	0
-	-	-	48.92	146.75	0

Going back to one dipole and the GA algorithm, the position found at the 100th iteration was taken as the initial position of the dipole in the NCG algorithm. After 10 iterations with NCG, the best dipole location was determined to be at 42.24 mm 96.60° and with an intensity of 1.1 which is very close to the GA results after 173 iterations. Evolution of the dipole characteristics and of the gradient g and b constant in NCG iterations can be observed in Table A3.

Table A3 Gradient (g) and b values (a= 0.01) at the 10 iterations of NCG needed to reach the optimal dipole position

Iteration	Inverse				
I	g	b	ρ(mm)	φ(°)	I
1	0.25	0.06	44.02	95.98	1.1
2	0.12	0.83	43.81	95.98	1.1
3	0.10	0.81	43.53	96.12	1.1
4	0.05	0.92	43.47	96.37	1.1
5	0.04	0.95	43.15	96.42	1.1
6	0.04	0.97	42.98	96.42	1.1
7	0.04	0.95	42.67	96.54	1.0
8	0.04	0.90	42.41	96.63	1.0
9	0.04	0.98	42.41	96.62	1.1
10	0.03	0.98	42.24	96.60	1.1

As for the computing time with an Intel® Core ™ i7 CPU 3.2 GHz processor and 12 GB of RAM, 142s were required to complete the 100 GA iterations and 277 s for the 173 iterations results. As for the NCG algorithm, its 10 iterations were finished in 18 s. So by combination GA+NCG, the best solution is obtained in 160s instead of the 277s if GA is only use. For 100 GA iterations when 2 and 3 dipoles are considered, the processing time is respectively 476 s and 1153s as compared to 142s with one dipole. The time benefit is thus expected to be more important as more complex situations as 3 dipoles in the experimental tank will have to be analyzed.

The programs used for the direct and inverse model as well as for initiating the genetic algorithm are presented in Appendix 4.

APPENDIX 6 – CMBEC 34 CONFERENCE PAPER

Proc. CMBEC 34, maghoul- 69363.pdf (FICCDAT CDROM) 4 pages, Toronto June 2011

DIRECT AND INVERSE MODELING IN EMG

Maghoul P[*], Mathieu P.A[**], Corinthios M[*],

[*]Dépt. génie électrique, École Polytechnique de Montréal,
[**]Institut de génie biomédical, Université de Montréal

Abstract—**Muscle activity is accompanied by an electrical signal (electromyogram or EMG) which travels through a complex volume conductor before reaching the surface of the body. Most usually, this signal is recorded with surface electrodes since it is not invasive but due to its alterations induced by the volume conductor, information on the signal origin is difficult to obtain. In such a context, the use of a direct and inverse model could offer useful information to help analyze and take benefits of surface EMG signals. We are developing such a model in the context of improving the control of myoelectric prostheses capable of producing various movements. This could be possible by exploiting the presence of anatomical compartments within large muscles such as the biceps and triceps brachii. If activation of those compartments could be individually activated, they could be used to activate modern myoelectric prostheses. To develop the models, a tank circled with recording electrodes and dipoles positioned at known positions was used. Preliminary results are presented here.**

Index Terms—**Electromyography, direct and inverse model, Poisson equation, myoelectric prosthesis.**

I. INTRODUCTION

In recent years, a lot of research has been done to improve the quality of life of upper arm amputee persons.Most available prostheses are electrically powered and controlled through surface EMG signals. With amputations around and above the elbow, the number of usable muscles to control a prosthesis is restricted. With intramuscular electrodes more recording sites could be obtained but for long term use, this approach is not practical due to possible electrode displacements induced by the repetitive contractions of the muscle and the risks of infection where the skin is pierced. In order to increase the number of surface control sites, the presence of up to 6 anatomic compartments innervated by individual nerve branches within the biceps brachial [1] is being investigated in our group. To help associate the EMG potential distribution collected over the biceps to those compartments, an inverse EMG model would be very useful. In the field of EMG, the one can find the models of analytic method and of numeric method [2,3]. In our case in this step, we choose the analytic approach.

II. METHODOLOGY

A. Experimental Methods

As a simple model of the arm, a tank surrounded by 16 equidistant electrodes and filled with saline solution was used.

Up to three dipoles were placed at various locations in the tank (Fig.1). The dipoles were activated with sinusoidal currents of 22 to 45 Hz. Initially, one dipole was placed at the periphery of the tank and moved radially toward its center. Then, two dipoles were used: one located near one electrode while the other was moved from the border to the center of the tank. Finally, three dipoles were used: two of them had the fixed positions next to the border of the tank (open circles in Fig.1) while the third one was moved from the border up to the center of the tank. The collected signals were analyzed off-line. The root mean square (RMS) values is obtained at each electrode recording from each dipole frequency contribution was used.

For the positioning of the dipoles, the power spectrum of the signal at one electrode was used to determine how many dipoles were present in the tank. Then, for comparison with the simulation results, the RMS value of the signal of each of those dipoles was obtained before their addition. To locate those dipoles the inverse model was used.
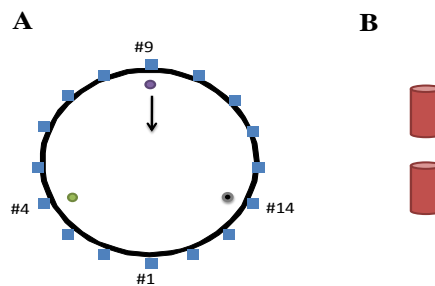

Fig.1. **A:** schematic of the tank (175 mm of diameter) circled by 16 equidistant Ag/AgCl electrodes of 10 mm in diameter and filled with a saline solution In this figure, the position of two dipoles is fixed (near electrodes #4 and #14) while the third one was moved radially step by step toward the center of the tank. **B**. each dipole is made of two cylindrical sintered Ag/AgCl of 1.5 x 3 mm separated by 2 mm and placed perpendicular to the bottom of the tank and few mm above the plane of the recording electrodes.

B. Direct Problem

For the direct and inverse model, we used the Poisson equation (1):

$$\nabla^2 V(r) = -j(r)/\sigma \qquad (1)$$

$$\frac{\partial V}{\partial n} = 0 \qquad (2)$$

where $V(r)$ is the electric potential associated with the current density source $j(r)$ within an homogenous medium of conductivity σ while (2) is associated to the limited dimensions of the tank. To simulate the experimental potential distribution recorded around the tank by our dipoles, we will have image phenomenon because of finite dimension of the tank (Fig. 2).

To obtain the potential through the tank, we extensively used the work of Lambin and Troquet [4] and Okada [5] to produce our models. To simulate the potentials around the tank, we have to solve:

$$V(r) = (p.\nabla)G(r,r') \qquad (3)$$

where p is the dipole moment. Furthermore $G(r,r')$ is green function and Φ_N is normalized solution of the Strum-Liouville problem defined by the eigenvalues of (4):

$$\nabla^2 \Phi_N + \lambda_N \Phi_N = 0 \qquad (4)$$

The Green function was used to solve (1):

$$G(r,r') = \sum_{n \neq 0} \Phi_N \Phi_N^* / \lambda_N \qquad (5)$$

where r is the coordinates of the observation point and r' those of a dipole. Due to the image phenomenon reflections at the bottom of the tank and at the top of the liquid give rise to two sets of dipole images located at r_j' and r_k'' that r_k'' is the location of dipole image relative to the bottom of the tank, z_0''. Furthermore the dipole image relative to the top of the liquid in tank, z_1''. r_j' is the image of z_0'' relative to the top of the tank, z_1'. Finally by solving (3) with conditions (4) and (5), equation (6) is reached.
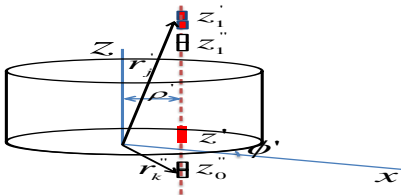

Fig. 2. The image phenomenon from the front section where the dipole is positioned at $z'(\rho'\varphi'z')$. Illustration modified from Lambin and Troquet [4].

$$V_z(\rho\phi z) = \frac{-p_z}{L^2\sigma} \sum_{m=0}^{\infty}(2 - \delta_{m0}) \times cos[m(\phi -$$

$$\phi')] \sum_{n=1}^{\infty} nI_m\left(\frac{n\pi\rho'}{L}\right)[K_m\left(\frac{n\pi R}{L}\right) -$$

$$\frac{K_m'\left(\frac{n\pi R}{L}\right)}{I_m'\left(\frac{n\pi R}{L}\right)}I_m\left(\frac{n\pi R}{L}\right)]cos\left(\frac{n\pi z}{L}\right)sin\left(\frac{n\pi z'}{L}\right) \qquad (6)$$

where I_m, K_m is the first and second kind of modified Bessel and δ is delta function.

C. Electrode size

Our electrodes being not punctual, a convolution equation taking care of the electrodes area was used to simulate their potentials. A simple equation assuming a constant value, equal to the inverse of the electrode area was used:

$$h_{size} = \frac{1}{S} \qquad (7)$$

where S is the electrode area. In case of a circular electrode with radius r, its transfer function will be:

$$H_{size} = \frac{J_1(2\pi r f_z)}{\pi r f_z} \qquad (8)$$

where $J_1(k)$ is the first-order Bessel function of the first kind and f_z is the spatial frequency which is defined by (9).

$$\lambda = \frac{1}{f_s} \qquad (9)$$

D. Inverse Problem

For the inverse model, the gradient method was used to minimize a cost function (10) evaluating the differences between values obtained with the Poisson equation and the experimental results:

$$C = \sum_{i=1}^{N}(V_{i,calculated} - V_{i,observed}) \qquad (10)$$

Due to the small size of our dipole (1.5 x 3 mm cylinder), they only affect the three closest electrodes. With the inverse model, potentials at those electrodes were used to identify where the moving dipole was positionned in the tank. A circle with a radius proportional to the voltage associated with that dipole at each of those electrodes was traced with the electrode positions as centers. The common intersection point of those circles gives the assumed position of the mobile dipole.

III. RESULTS

The results with two dipoles (one in a fixed position near an electrode and one moving radially from the border to the center of the tank) are presented in Fig.3A for the three electrodes where a signal could be recorded As the mobile dipole is getting farther from the recording sites, the signals decrease exponentially but does not reach zero due to the fixed dipole. That value was subtracted and the obtained signal was evaluated by (10) where ρ' parameter of (6) was used to estimate the position the mobile dipole in the tank as illustrated in Fig.3B. In presence of three dipoles (two fixed and one mobile), (Fig.4A), the voltages recorded at the three involved electrodes are varying as with two dipoles. With the inverse model, location of the mobile dipole was more precise up to 40 mm from the border of the tank than further away (Fig. 4.B).
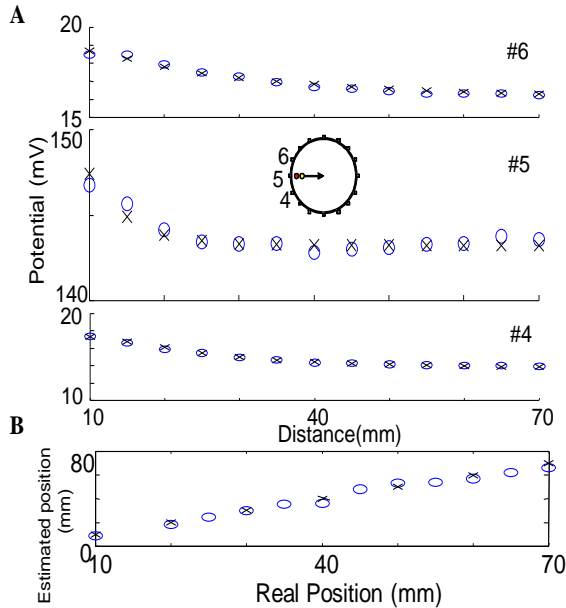
Fig. 3.A) Potentials recorded at three electrodes as a dipole is moved radially from the border to the center of the tank while a second one is kept fixed near the border. Experimental data (circles) and simulation results (crosses). B) Real (circles) vs estimated position (crosses) of the mobile dipole.
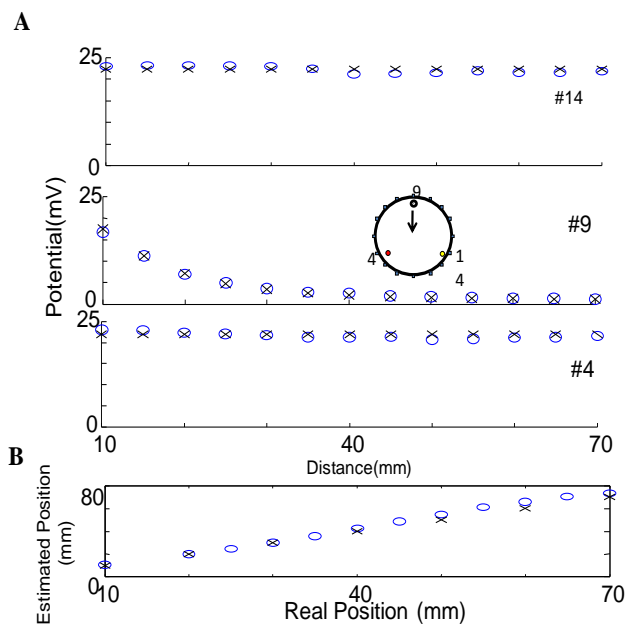
.

Fig. 4.A) Experimental data (circles) and simulation results (crosses)with two fixed fipoles (near electrodes #4 and #14) and a third one moving radially toward the center of the tank. B) Three dipoles in the tank. Estimated (circles) vs real position (continuous line) of the mobile dipolel.

IV.   DISCUSSION

With a dipole placed near the border of the tank and a second one moved toward the center, the direct model was in error close to the border (Fig. 3). This could be due to the lack of perpendicularity of the tube holding the dipoles (eqn. 6 is developed for a dipole perfectly aligned with the Z-axis). As expected, this effect has more effect when the mobile dipole is near the border of the tank than closer to the center. With the inverse model, the larger error is found when the mobile dipole is approaching the center of the tank (Figs. 3B and 4B).This is associated to the exponentially diminishing contribution of the dipole to the potentials recorded around the tank which makes the detection of its position more difficult.

In the future, inhomogeneities will be insert in the tank to simulate some of the conductive medium (bone, fat, blood vessels) The presence of many boundaries conditions will make the analytical solution too difficult to manage with an analytical approach. A numerical solution, like the Finite-Difference Time-Domain Method (FDT) will then have to be considered.

REFERENCES
[1] Segal, L., "Neuromuscular compartments in the human biceps brachii muscle",Neuroscience Letters, Volume 140, Issue 1, 8 June 1992, Pages 98-102
[2] Lowery, M. M., N. S. Stoykov, A. Taflove, and Kuiken, "A multiple-layer finite-element model of the surface EMG signal," IEEE Trans BME 49, 446–454 (2002).
[3] Gootzen, T. H., D. F. Stegeman, and A. Van Oosterom, "Finite limb dimensions and finite muscle length in a model for the generation of electromyographic signals," Electroenc Clin Neurophysiol, 81, 152–162 (1991).
[4] P. Lambin, and J. Troquet, "Complete Calculation of the Electric Potential Produced b a Pair of Current Source and Sink Energizing a Circular Finite-Length Cylinder", J. Appl. Phys, 54:7, 4174-4184, 1983.
[5] R.H Okada, "Potentials Produced by an Eccentric Current Dipole in a Finite-Length Circular Conducting Cylinder", IRE. Trans. Med. Electron, 7, 14-19, 1956.
[6] D.K Cheng, Field and Wave Electromagnetics. Addison-Wesley Publishing Co., 1983.
[7] T.H.J.M Gootzen, and D.F Stegeman, and A, Heringa, "On Numerical Problems in Analytical Calculations of Extracellular Fields in Bounded Cylindrical Volume Conductors", J. Appl. Phys, 66:9, 4504-4508, 1989.
[8] J.K Jackson , Classical Electrodynamics. Wiley, New York, 1962.
[9] J. Malmivuo, and R. Plonsey, Bioelectromagnetism. Oxford U. Press, 1995.
[10] M.O Sadiku, Numerical Techniques in Electromagnetics, CRC Press, 2009.
[11] K. Saitou, and T. Masuda, Okada M. "Depth and intensity of equivalent current dipoles estimated through an inverse analysis of surface electromyograms using the image method", BMES 1999, Vol. 37, pp 720-726.
[12] S.A Schelkunoff, Electromagnetic Waves (Van Nostrand Co., New York, 1943)
[13] Fuglevand, A., D. Winter, A. Patla, and D. Stashuk, "Detection of motor unit action potentials with surface electrodes: influence of electrode size and spacing," Biol cybern 67, 143–153, 1992.